POLITECNICO DI TORINO

Master degree in Biomedical Engineering

A.Y. 2024/2025



Development of magnetically patterned anisotropic hydrogels for Xolography-based volumetric 3D printing to guide myocytes organization

Supervisor:

Candidate:

Dott. Ignazio Roppolo

Silvia Compagno

Prof.ssa Francesca Frascella

S311594

Acknowledgements

I would like to express my heartfelt gratitude to Ignazio Roppolo and Francesca Frascella for their support and incredible availability throughout this past year, both professionally and personally.

I am deeply thankful to Professor Miguel Castilho, Dr. Gerardo Cedillo Servin, and all the members of the Biomaterials and Biofabrication group at Eindhoven University of Technology for welcoming me into their lab and giving me the opportunity to be part of their research.

I would like to thank Francesco Schimmenti for being by my side throughout this journey, both in Turin and in Eindhoven, together with all the other members of the 3D Printing group at Politecnico di Torino. I would also like to thank Gabriele Addario for his kind help and support.

A special thanks to Leonor, Teresa, and Sara, the best lab team I could ever ask for. These months with you have been precious and unforgettable — I can't wait to see you again.

Abstract

Skeletal muscle (SkM) is a highly organized tissue displaying multiple levels of structural organization, whose development and contractile function is intimately related to its anisotropic structure. To engineer SkM in vitro models, scaffolds must mimic the native extracellular matrix (ECM) architecture, providing not only biochemical but also physical cues to promote myoblasts alignment and maturation. Hydrogels provide a water rich, biomimetic 3D environment, and represent the most promising candidate materials to engineer scaffold for tissue engineering applications. However, the intrinsic isotropy inherent to their network is not capable of guiding cell alignment, limiting their applicability to those tissues characterized by high level of structural anisotropy, like skeletal muscle.

One of the latest strategies explored to produce anisotropic hydrogel scaffolds is based on the incorporation and remote manipulation of magnetic nanoparticles (MNPs) inside the hydrogel liquid precursor. Under a uniform magnetic field, they spontaneously arrange into linear, chain-like aggregates aligned along the field lines, which are finally stabilized upon 'sol-to-gel' transition of the host matrix. These anisotropic structures can act as topographical cues to guide cells alignment, as largely demonstrated in the literature. Super paramagnetic iron oxide particles (SPIOPs) are the most used type of MNPs due to their high cytocompatibility.

Beyond structuration at the microscale, hydrogels can be fabricated into the required shape by a wide range of additive manufacturing (AM) technologies, including direct ink writing (bioplotting) and vat photopolymerization. The use of AM strategies has rapidly spread in the field of tissue engineering to address the growing need to improve the control over the structural and mechanical properties of scaffolds at the macroscale, key factors in regulating cells behavior. The integration of AM technologies with the self-assembly approach will pave the way for the fabrication of constructs with structural control at multiple scale lengths.

Within this framework, the aim of the work is to investigate a further step ahead in the development of advanced hydrogels, studying a magnetically patterned, cell-laden, hydrogel-based scaffold which can be processed via the innovative technology of Xolographic volumetric printing. The intended goal is to provide the hydrogel-photo-resin with an inner microstrucure composed of anisotropic fibril arrangements of self-assembled SPIONs, while preserving its printability.

The research activities were conducted both at Politecnico di Torino (MPMNT research group) and at TUE in Eindhoven (the Netherlands), in the Dias Castilho's group.

In this Thesis work, first the principles of skeletal muscle engineering will be introduced (chapter 1), followed by a description of magnetic hydrogels (chapter 2) and additive manufacturing (chapter

3). Then, the experimental part will be shown, first explaining materials and methods (chapter 4) applied in this work and then reporting experimental results (chapter 5). Finally, a conclusion chapter will summarize the results obtained, discussing future developments.

Index

1. Skeletal muscle in-vitro models	7
1.1 Tissue engineering	7
1.2 Hydrogels	8
1.2.1 Hydrogel Classification Based on Crosslinking	9
1.2.2 Hydrogel Classification Based on source	12
1.3 Skeletal muscle anatomy	
1.4 Anisotropic hydrogel scaffolds	16
2. Magnetic hydrogels	
2.1 Superparamagnetic nanoparticles	19
2.2 Magnetic field-driven self-assembly	22
2.3 State-of-the-art of anisotropic magnetic hydrogel	25
3. Additive manufacturing (AM)	31
3.1 3D-Printing overview	32
3.2 Vat polymerization printing	34
3.2.1 Photopolymerization	36
3.2.2 Stereolithography (SLA)	39
3.2.3 Digital light processing	40
3.2.4 Computed axial lithography (CAL)	40
3.2.5 Two-photon photopolymerization	42
3.3 Xolography	43
4. Materials and methods	49
4.1 GelMA synthesis	49
4.2 Optimization of IOPs self-assembly	50
4.3 Adaptation of the self-assembly approach to Xolography	54
4.3.1 XOLO printers	54
4.3.2 Photoresin preparation	55

4.3.3 Stabilization of the anisotropic pattern in XOLO cuvette	57
4.4 Cell culture	58
4.4.1 Cell casting – Cytocompatibility analysis	59
4.4.2 Live/Dead essay	60
4.4.3 Cell casting – Anisotropic Magnetic Hydrogels	60
4.4.4 DAPI/Phallodin staining	61
5. Results and discussion	62
5.1 Kinetics of IOPs self-assembly	62
5.2 Integration of IOPs self-assembly with XOLO technology	65
5.2.1 Printability of magnetic photoresins	65
5.2.2 Stabilization of anisotropic pattern in printed objects	69
5.3 cell culture	70
5.3.1 Live/dead essay	70
5.3.2 Phase-contrast imaging	71
5.3.3 Myotubes orientation	74
6. Conclusions	76
References	80

1. Skeletal muscle in-vitro models

Skeletal muscle (Skm) accounts for 40–45% of an adult human body mass and controls voluntary movement and locomotion [1]. It can be functionally compromised by several causes, such as aging, traumatic injuries, tumor ablation and genetic diseases. The loss of Skm function leads to muscular dystrophies (MD), a class of diseases characterized by progressive weakness that severely affects the quality of patients' lives, by causing disability and, ultimately, death [2], [3]. Traditionally, small animal models and two-dimensional cell cultures have been employed to investigate biological processes and to identify and validate pharmacological compounds for the treatment of SkM disorders, but their translational relevance is limited by their poor ability to predict drug responses in humans. This underscores the need for engineering authentic and reliable in vitro skeletal muscle models for disease modeling and/or drug testing. In the big picture, this lies in the larger framework of tissue engineering [4].

1.1 Tissue engineering

Tissue engineering (TE) is an interdisciplinary field that merges the principles of engineering and life sciences, combining living cells, biocompatible materials, and suitable biochemical and physical factors to develop biological substitutes that restore, maintain or improve tissue or organ function. This innovative approach was first developed in the mid-1980's and emerged as a potential alternative to tissue or organ transplantation [5]. In addition to clinical applications, other uses include drug testing for efficacy and toxicology as well as basic studies on tissue development, morphogenesis and pathogenesis [6], [7].

The concept at the basis of tissue engineering consists in the addition of cells into biomaterials where cells can proliferate under the influence of a favorable microenvironment [8].

Biological tissues consist of a highly organized interplay of cells and extracellular matrix (ECM) components. In tissue engineering, the substitute of native ECM is called "scaffold", and it represents the microenvironment where cells reside and interact. Scaffolds must provide structural support to the cells during the initial stages of tissue formation. With the goal to achieve proper morphological and functional tissue maturation, scaffolds should (i) mimic the complex structural organization of the native tissues from nano- to macroscale; (ii) match the mechanical and electrical properties of the tissues; (iii) provide the required biophysical and biochemical cues to induce the desired growth, proliferation, and differentiation of the cultured cells [9]. The fabrication of a physiologically relevant in-vitro tissue model requires a proper design of the scaffold in a way to mimic as close as possible the properties of the native ECM of the target tissue [10]. Indeed, the

extracellular environment to which cells are exposed strongly affects the intracellular signaling cascade that governs cell phenotype, namely their structural and functional characteristics [11].

Among the different types of materials investigated as matrices for 3D cell culture, hydrogels are excellent candidates as they recapitulate several features of the native ECM. Hydrogels have gained great attention in biomedical applications to develop 3D scaffolds due to their biocompatibility, soft mechanical properties similar to biological tissues, water-rich composition, ability to encapsulate cells and other biological entities, and easy tunability of their chemical and mechanical properties to match those of target tissues [12], [13].

1.2 Hydrogels

Hydrogels are three-dimensional (3D), cross-linked networks of hydrophilic polymers which can absorb and retain significant amounts of water, up to several times their weight, while maintaining their shape (see *Figure 1.1*). They do not dissolve in water thanks to the existence of cross-linking points between the polymeric chains [14], as shown in *Figure 1.1*. Those can be either chemical (i.e. covalent bonds) or physical (e.g. crystalline phases and electrostatic bonds). It is, indeed, this 3D polymeric frame (or mesh) to confer to the gels solid-like mechanical properties, such as absence of fluidity and the capacity to maintain their shape, strength, flexibility and elasticity [15]. Their hydrophilic nature arises from the presence of polar functional groups within the polymer chains, such as hydroxylic (-OH), carboxylic (-COOH), or sulphonic (-SO₃H) groups [16].

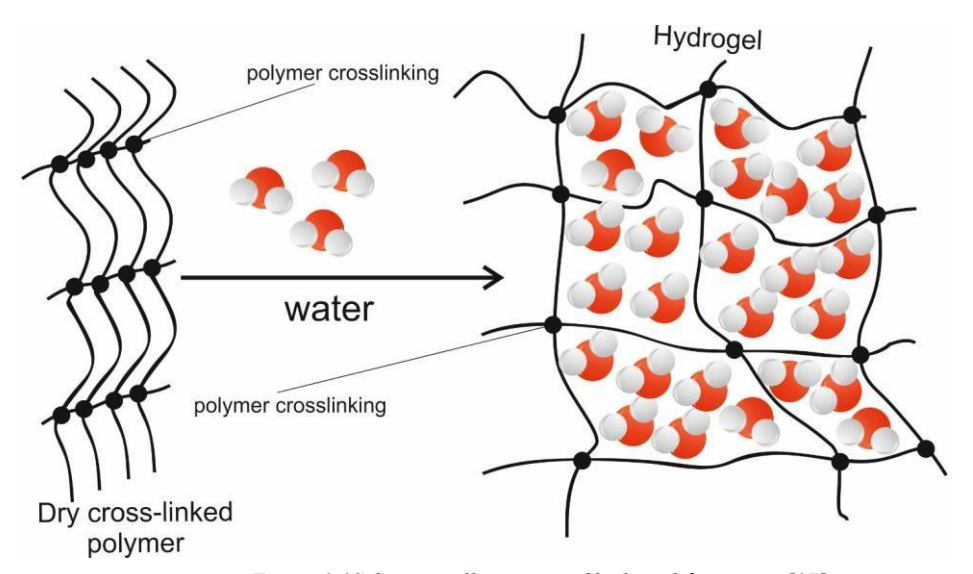


Figure 1.1Schematic illustration of hydrogel formation [17]

Hydrogels possess exceptional physicochemical properties, such as high swelling ability, and high permeability, which favored their application as imaging, diagnosis, and treatment tools. Cytocompatible polymers can be used for hydrogels fabrication, making them suitable for many biomedical applications [18]. Wichterle and Lim, in 1954, established the first application of

hydrogels, developing soft contact lenses using a crosslinked poly-2-hydroxyethylmethacrylate (pHEMA) network [19]. Since then, the use of hydrogels rapidly grew in a wide range of fields, including drug delivery, tissue engineering, skincare products and food products. [18]. To name a few, polysaccharide-based hydrogels (e.g. chitosan, alginate and cellulose.) have been employed for wound dressing, and hyaluronic acid (HA) hydrogels for drug delivery applications. Injectable hydrogels were widely investigated for the targeted drug delivery to tissues, such as cartilage [20].

Also, are well suited to be processed into the required 3D shape and size using a wide range of additive manufacturing processes. The use of 3D printing technologies has rapidly spread in the field of TE in recent years, as they allow the fabrication of scaffold with high complexity, impossible to achieve with conventional methods. [21].

Several criteria exist to classify hydrogels, summarized in *Figure 1.3*, such as by source, type of cross-linking, type of response and preparation method [22].

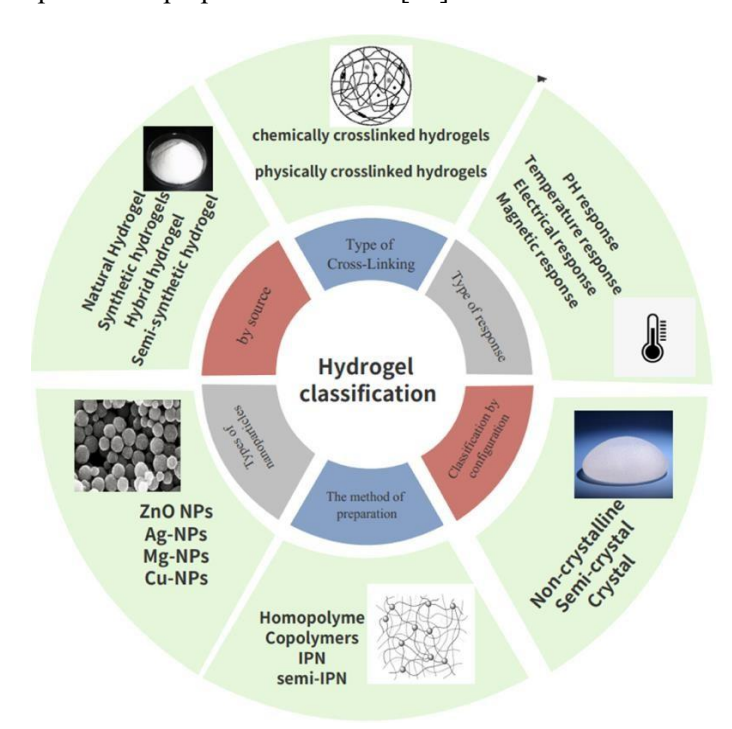


Figure 1.2 Types of hydrogels classification [22]

1.2.1 Hydrogel Classification Based on Crosslinking

The term "gelation" (or "sol-to gel transition") describes the process during which different macromolecular chains (dissolved in water) progressively link together, forming branched polymers of increasing size and reduced hydro-solubility, until a single big insoluble polymeric network is formed. Various types of gelation mechanisms exist (see *Figure 1.3*) that can be grouped into two main categories: physical and chemical gelation, depending on the nature of the cross-links between

the macromolecules. Accordingly, hydrogels can be classified as chemical (permanent) or physical (reversible) [23].

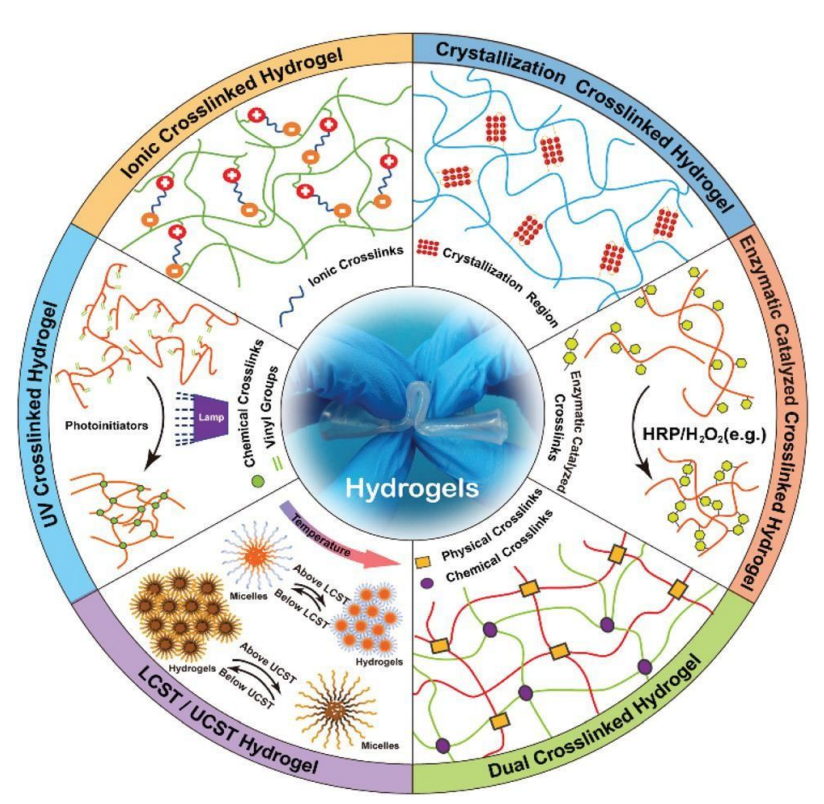


Figure 1.3 Hydrogels classification according to the cross-linking method [24]

1.2.1.1 Physical hydrogels

In physically crosslinked hydrogels (or physical hydrogels) the structure is preserved from dissolution by intermolecular entanglements or secondary interaction forces [23], such as ionic/electrostatic interaction, hydrogen bonds, hydrophobic interactions, crystallization, metal coordination and π – π stacking. [25]. Due to the reversible nature of these interactions, physical hydrogels are themselves "reversible", in the sense that those can be formed and broken in a controlled manner upon changes in the physical conditions [23]. A key advantage of physically crosslinked hydrogels is the biocompatibility of the gelation process, that does not require chemical crosslinking agents, typically cytotoxic [25]. On the other hand, they may need controlled temperature or the presence of salts.

- <u>Ionic interactions</u>: the mesh is kept together by attractive electrostatic forces between molecules of opposite electric charges [25]. As an example, divalent cations, like calcium (Ca2+), can be used to crosslink alginate, a naturally derived polysaccharide, by interacting with its negatively charged glucuronic acid residues.[26].
- <u>Hydrofobic interactions</u>: an aqueous solution of amphiphilic polymers, i.e. polymers containing both hydrophilic and hydrophobic segments, can undergo sol-to-gel transition

induced either by temperature or ultrasonic treatment. These polymers tend self-assemble into organized structure (e.g. micelle), exposing their hydrophilic blocks to water while hiding the hydrophobic portions within a core, to minimize their contact with water. Temperature variations can trigger hydrophobic interactions between nearby micelles, leading to their aggregation and gel formation. There are polymers which are soluble below a LCST (lower critical solution temperature), while other polymers are soluble above an UCST (Upper Critical Solution Temperature) [25]. An example is represented by the amphiphilic copolymers combining hydrophilic poly(ethylene oxide) with hydrophobic poly(propylene oxide), widely used as injectable drug delivery systems, that gelate at physiological temperature [27]

- <u>Crystallization:</u> Polymer chain crystallites can serve as physical crosslinking points within the network, leading to hydrogel formation. For example, hydrogels can be obtained when an aqueous solution of poly(vinyl alcohol) (PVA) is subjected to repeated freeze—thawing cycles. The resulting hydrogel properties are influenced by factors such as polymer molecular weight, solution concentration, freezing temperature and duration, as well as the number of freeze—thaw cycles [28].
- <u>Hydrogen bond</u>: is among the most important noncovalent interaction types. Hydrogen (H) bonds are used in nature to stabilize a peptides' secondary structure. Typical groups involved in H-bonds formation are amide, urea, carboxylic acid, pyrrole, carbazole and hydroxyl groups [25].

1.2.1.2 chemical hydrogels

In chemically crosslinked hydrogels covalent bonds are used to cross-link the polymeric chains of the networks, which are much stronger and more stable over time than physical interactions [18]. The cross-linking can be induced by the introduction of cross-linking molecules, photosensitive agents or enzymes. Compared to physical hydrogels, major control is allowed toward hydrogel properties, which can be tailored by choosing the appropriate cross-link agent and/or chemically modifying the polymers [29]. Different routes are possible to produce chemical hydrogels: copolymerization of multifunctional monomers, reactions with crosslinkers, high energy irradiation, chemical reactions of pendant groups, etc. The most used strategies include the free-radical polymerization, enzyme mediated crosslinking, and the so-called "click chemistry" reactions [18].

- <u>Free-radical polymerization</u> can be initiated by light (photoinitiation), redox reactions, heat (thermal initiation), or ionizing radiation [30]. Photo-initiated polymerization is the most used and relies on the presence of unsaturated moieties, usually (meth)acrylates, containing highly reactive double bonds between carbons (-C=C-). When exposed to photo-irradiation these bonds promote a free radical chain growth polymerization. The mechanism of photopolymerization will be extensively discussed in Section 3.2.1. Hydrophilic polymers

- containing hydroxyl, carboxyl and amino groups can be chemically functionalized to include vinyl groups [25].
- Enzymatic cross-linking enables tunable control of gelation by adjusting the enzyme concentration and reaction parameters. Gel formation depends on the specific enzyme and reaction conditions. This strategy for hydrogel formation is straightforward and proceeds under closely physiological conditions, typically with high efficiency and without requiring toxic reagents, elevated temperatures, or ionizing radiation [18]. Transglutaminase (TG) is a commonly used enzyme, that, in the presence of calcium ions, promotes the bridging of amide linkages among carboxamide and amine groups [31].
- <u>Click-chemistry</u>: is a family of chemical reactions performable in mild conditions, characterized by high yields under mild conditions, low by-products generation, high specificity and selectivity. It includes Diels-Alder, Schiff base, oxime and Michael-type addition [32].

1.2.2 Hydrogel Classification Based on source

Depending on the nature of the polymer from which their network is derived, hydrogels can be categorized as natural, synthetic or hybrid (semi-synthetic). A wide variety of hydrogels belonging to these categories have been successfully used as 3D substrate for cell culture applications [33].

1.2.2.1 Natural hydrogels

Natural polymers used for this purpose include hydrogel-forming proteins (e.g. gelatin, collagen, fibrin, and silk fibroin) or polysaccharides (e.g. hyaluronic acid, chondroitin sulfate, alginate, and chitosan) [33]. Hydrogels derived from natural polymers are endowed with integrin-binding motifs naturally present in native ECM. A widely used natural component for TE applications is gelatin, a soluble polypeptide mixture of denatured and partially hydrolyzed collagen, the must abundant protein of the human body. Pure gelatin is water soluble, and forms thermo-reversible, transparent hydrogels via physical interactions (hydrogen bonds) at low temperatures. However, these hydrogels reverse back to the liquid state at the physiological temperature (37°C), making them unsuitable for cell culture applications when used alone and unmodified. Gelatin, like collagen, contains Arginine–Glycine–Aspartic acid. (Arg-Gly-Asp, or RGD) sequences that bind to integrin receptors on the cell surface, thereby making the hydrogel bio-adhesive [34]. The binding of cells surface receptors to these sites (see *Figure 1.4 A*) can direct cells behavior by promoting the mechano-transduction of intracellular signaling pathways, and that has proved to improve viability and function of cultured cells The drawbacks of natural hydrogels are the significant batch to batch properties' variation and the presence of impurities [11].

1.2.2.2 Synthetic hydrogels

On the other hand, synthetic hydrogels offer the advantage of reproducible, well-defined and tunable physicochemical properties [35]. These are commonly synthetized from polyethylene glycol (PEG), polyvinyl alcohol, polyacrylamide, and pluronics, a polyethylenoxide-polypropylene oxide copolymer [33]. The main limitation of synthetic hydrogels resides in the lack of cell-binding and protease-cleavage motifs naturally found in native ECM, which affects their ability to support cell attachment and matrix remodeling. Hydrogels made of synthetic polymers provide a 3D environment that simply permits cell function, but do not possess any cell-adhesive sites to which cells' surface receptors, e.g. integrins, can bind (see Figure 1.4 B) and lack the endogenous factors that promote cell behavior [11]. As an example, Bryant and Anseth showed that cells encapsulated inside PEG hydrogels can live and deposit their own ECM as they degrade, proving that synthetic hydrogel can be used for 3D cell culture applications [36]. Hydrophilic polymers containing hydroxyl, carboxyl and amino groups can be chemically functionalized to include vinyl groups (-C=CH), that can participate in radical polymerization [25]. Thus, PEG chains can be chemically modified to include terminal acrylate groups, yielding PEG diacrylate (PEGDA). PEGDA hydrogels were first used to produce scaffolds for TE in 1970, proving high biocompatibility and low toxicity. Also, due to its fast polymerization kinetics, it has been widely employed in 3D printing application to develop skeletal muscle and cardiac tissues [37].

Nevertheless, to better recapitulate native ECM, biomimetic signals must be introduced within synthetic permissive hydrogels, to promote desired cell-matrix interactions [11] by incorporating biomimetic signals into synthetic materials

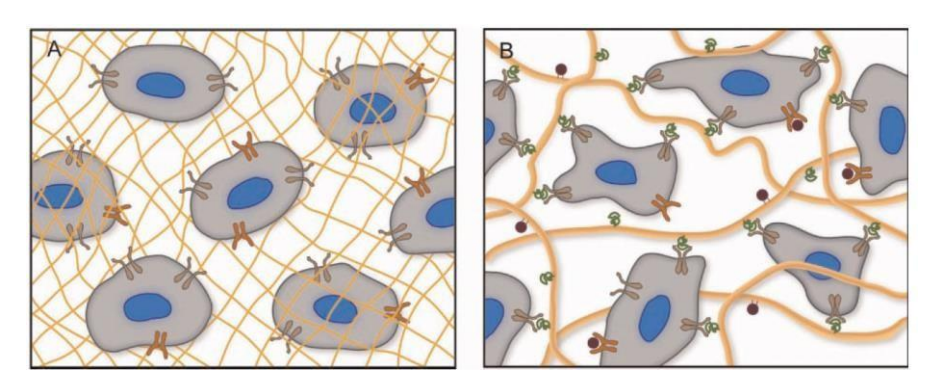


Figure 1.4 Simplified illustration of cell-matrix interaction in synthetic (A) and natural (B) hydrogels [11]

1.2.2.3 Hybrid hydrogels

To overcome the limitations of the two classes of materials, semi-synthetic (or "hybrid") hydrogels have been developed. They integrate the advantages of both natural and synthetic polymers, harboring both integrin cell-binding and protease-cleavage sites together with chemically active motives that ensure the reproducibility and easy tunability of mechanical and biochemical

characteristics [38]. One proposed strategy to realize hybrid hydrogels consists in the functionalization of the synthetic polymeric chain with cell-responsive sites [39]. Otherwise, different hydrogel precursor components, both natural and synthetic, can be mixed to merge the advantages of the two kinds of materials. By entrapping ECM proteins into the synthetic hydrogel network, it is possible to provide binding ligands to the encapsulated cells, to improve cell viability and function, while gaining the advantages of a synthetic bulk material [11].

Another example is given by Gelatin methacryloyl (GelMA), obtained by functionalizing gelatin molecules with photo-sensitive, unsaturated methacryloyl groups (MA). The presence of MA groups along the polymer backbone addresses the issue of thermal reversibility of bare gelatin solutions, providing stable bio-active 3D framework for cell culture applications: an aqueous solution of GelMA can create covalently cross-linked hydrogels by photo-polymerization under mild conditions (see *Figure 1.5*), enabling cell encapsulation with high viability. Additionally, this chemical modification provides remarkable versatility in tuning the final properties of the hydrogel: parameters like gelatin concentration, degree of functionalization (DoF), photoinitiator type, and photo-cross-linking time can be adjusted to control the gel's mechanical stiffness [40]. [41].

Figure 1.5 The chemical reaction between gelatin and methacrylate anhydride to produce GelMA and light-induced crosslinking between two GelMA molecules [41]

1.3 Skeletal muscle anatomy

The basic structure of the skeletal muscle consists of highly organized, densely packed multinucleated cell fibers (called "myofibers"), blood vessels, nerve, and connective tissue, characterized by highly uniaxial alignment degree along the main axis of the tissue [42], as depicted in *Figure 1.6*. Individual myofibers result from the process of myogenesis, which consists in an initial stage of fusion of multiple myocytes into single multi-nucleated cells (called "myotubes") followed by their further maturation into myofibers [43]. Three layers of connective tissue (epimysium, perimysium, and endomysium) support the hierarchical organization of the skeletal muscle: individual myofibers are wrapped in a thin endomysium layer; many myofibers are stacked together, along with neurons and blood vessels, to form cylindrical bundles (fascicle) enclosed by perimysium; and multiple fascicles are bundled together by an outer epimysium layer to form a real muscle [44], [45].

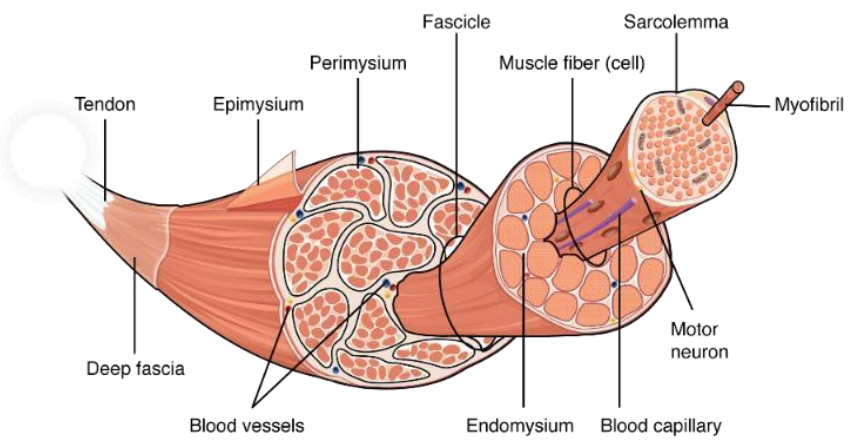


Figure 1.6 Anatomy of the skeletal muscle [46]

Cell organization in skeletal muscle is intimately connected to the tissue contractile function [47]. Anisotropy is an essential feature associated with the development, functions, and regeneration of skeletal muscle tissue. For this reason, skeletal muscle TE strategies are focused on the design of anisotropic scaffolds capable of providing cells with the adequate physical cues to promote myoblasts alignment, elongated growth, and fusion. [48]. Indeed, inducing cell alignment represents the first and foremost step in the myogenic process. As demonstrated, myoblasts grow randomly in the absence of proper physical guidance and that is not conducive to generate contractile tissues [49]. Early studies on 2D cultures demonstrated that groove/ridge micro- and nano- scale surface topographies can induce myoblast alignment and elongation [50], [51] proving the positive effect of physical cues.

The microenvironment of skeletal muscle is composed of a three-dimensional (3D) network of hierarchically organized fibers which are key in force generation and orientation by providing

critical topographical cues and spatial boundary conditions to the cells [52]. Therefore, to engineer reliable SkM in vitro models the effort of researchers has focused on the development of 3D matrices that restore myofiber organization by introducing anisotropic mechanical environments during regeneration [53].

1.4 Anisotropic hydrogel scaffolds

As mentioned before, hydrogels are among the most promising candidate materials to develop 3D TE scaffolds and have been widely employed also for skeletal muscle tissue engineering. However, their isotropic nature prevents them to mimic the architectural features of those human tissues characterized by highly anisotropic structural organization, among which skeletal muscle represents a noteworthy example [54]. Indeed, their disorganized network structure is not conducive to cell alignment [47].

Many tissues in vivo exhibit structural anisotropy, arising from the preferred orientation of extracellular matrix proteins and/or cells along a specific axis, which imparts tissues with orientation-specific properties and functions, for instance the unidirectional force transmission in the skeletal muscle. Thus, biomimetic scaffolds replicating the anisotropic ECM structure are of great importance. To this end, structurally anisotropic hydrogels have emerged as promising scaffolds for TE applications. They are fabricated by inducing a specific orientation of nanofillers, pores, fibrous networks, or surface topographical features. These kinds of hydrogels exhibit enhanced mechanical, conductivity, and mass transport properties along the direction of orientation. Cells cultured in and on anisotropic hydrogels exhibit elongated morphology and directional migration [55].

Several methods have been proposed to adjust hydrogel microstructure to generate structurally anisotropic ECM substitutes capable to direct cell alignment, summarized in *Figure 1.7*.

- (a) <u>Aligned electrospun fibers</u>: By presenting the cells with micro- or nano-scale topological cues, aligned fibers enable the mimicking of native anisotropic structure, being more efficient in promoting myotube alignment and assembly than micropatterned substrates [56]. Among the different possibilities to generate fibrous scaffold, the electrospinning technique has been well established, allowing to produce fibers of both natural and synthetic polymers [57]. Ku et al. have incorporated PANi into PCL polymer to fabricate a conductive nanofibrous scaffold [58], demonstrating that cellular organization has been effectively steered by fiber orientation.
- (b) <u>Unidirectional channels:</u> Jana et al. used thermally-induced phase separation followed by directional free-drying to create uniaxial, tubular, porous microstructures within 3D

- scaffolds. This strategy allows the creation of unidirectional pores within the 3D matrix that proved to be effective in inducing myoblasts alignment, thus in engineering oriented tissues [59].
- (c) <u>Mechanical tension</u>: Another largely explored strategy to facilitate myoblasts alignment within 3D hydrogel matrices is based on the application of an external mechanical tension to the hydrogel scaffold by anchoring the two ends of the hydrogel construct to two more rigid pillars. The tensile stimulus exerted by the pillars drives cells alignment and promotes the fusion of the embedded myoblasts into multinucleated myotubes organized into uniaxially aligned fiber bundle [60]
 - (d) Incorporation of nano-/micromaterials: the incorporation of nano- or micro-sized materials into a hydrogel 3D network has been recently explored to reproduce the architectural features of highly anisotropic biological tissues. In particular, the use of magnetic nanoparticles (MNPs) showed great advantages to build anisotropic ordered patterns within polymeric hydrogel scaffolds [54].

The method investigated in this Thesis work to produce anisotropic hydrogel to guide cells alignment is part of this last approach, and therefore it will be described in detail in the next chapter.

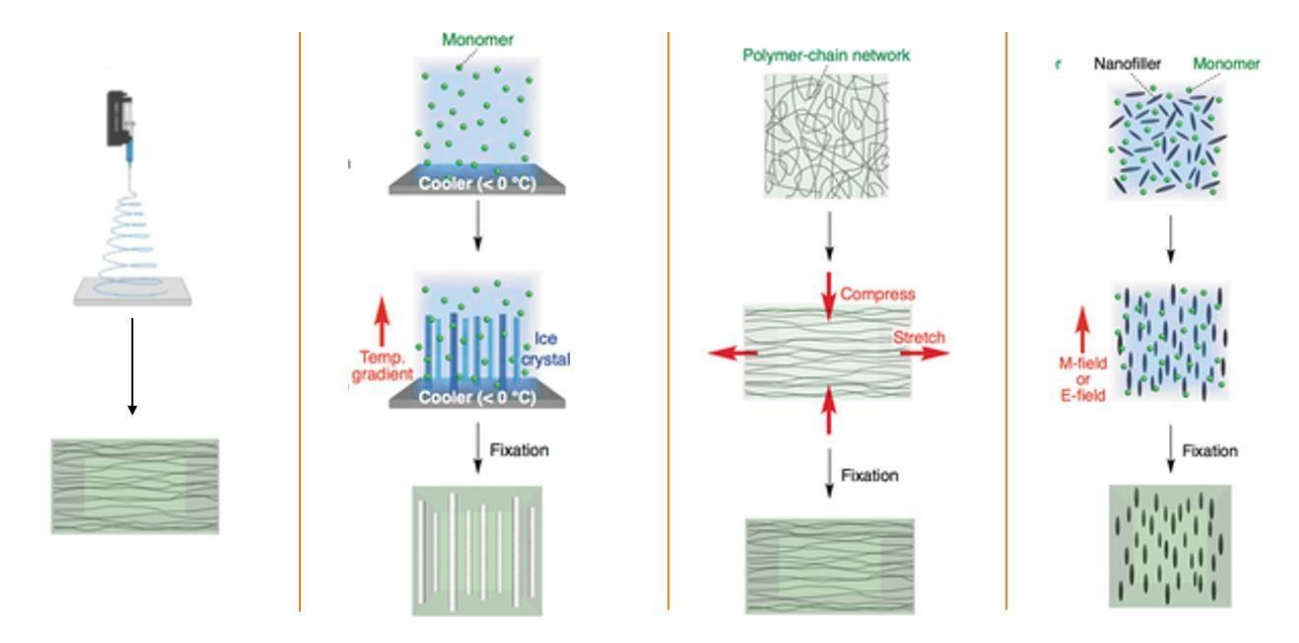


Figure 1.7 Fabrication methods to generate structurally anisotropic hydrogels [55]

2. Magnetic hydrogels

Cells embedded in patterned nanocomposite materials resembling their native ECM could find the specific array of bio physical and biochemical cues for proper growth and maturation. To this end, different architectures can be achieved through the application of electromagnetic fields to promote the self-assembly of nanosized materials [61].

Magnetic nanoparticles are one of the most appealing choices as building blocks due to the possibility to manipulate their distribution within a liquid medium (e.g. hydrogel precursor solution) through the application of external magnetic fields. This innovative approach allows a controlled design of magnetically patterned, anisotropic scaffolding materials, which can be used to engineer different kinds of anisotropic tissues, e.g. cardiac, neural, muscle, cartilage [62].

To produce magnetic anisotropic hydrogel, the general three-steps approach is the following:

- 1. Mix magnetic particles with the liquid hydrogel precursor solution until a homogeneous dispersion is achieved,
- 2. Apply a uniform magnetic field, usually by means of two permanent magnets, to promote the self-assembly of MNPs into bigger linear aggregates
- 3. Stabilize particles anisotropic arrangements by inducing the gelation of the hydrogel solution.

Within a system of magnetic nanoparticles dispersed inside a liquid medium, the application of a uniform magnetic field produces magnetic forces that cause the spontaneous assembly of particles in chain-like structures aligned along the magnetic field lines, as a result of the head-to-tail arrangement of their magnetic moments. This approach can be applied with polymer solutions, molten polymers or photocurable formulations, leveraging the solidification/curing of the polymeric matrix to permanently stabilize the self- assembled particles microstructures. The self-organization of disordered building blocks provides anisotropy to the composite material. The driving force for the self-assembly process in a nanomagnetic system are dipole- dipole magnetostatics interactions [63].

Among the different types of MNPs, iron oxide nanoparticles (IOPs) are the most utilized for biomedical application, because of their low cost, easy production, and reduced toxicity. Also, MNPs must bear high magnetic responsiveness, to achieve their remote manipulation while minimizing the content of magnetic filler and the magnetic field intensity, being these two critical toxicity/safety factors. For these reasons, superparamagnetic iron oxide particles (SPIONs), characterized by very high magnetic responsivity, are usually selected [54].

Before reviewing state-of-the-art examples of magnetic micro-structured hydrogels, the properties of superparamagnetic nanoparticles and the physical principles underlying the magnetic field-driven self-assembly will be introduced.

2.1 Superparamagnetic nanoparticles

Magnetic properties of materials originate from the magnetic moment associated with single electrons of their constituent atoms. Each electron acts like a small magnet whose magnetic moment arises from two different sources: its orbital movement around the nucleus and its rotation around its own axis (spin). The magnetic moment of an atom is given by the sum of the orbital and spin magnetic moments of its electrons. The sign of the magnetic moment depends on the spin orientation (up or down) of the electron. When two electrons occupy the same orbital with opposite spins, their magnetic moments cancel each other, resulting in no net contribution. In atoms with fully filled electronic shells or subshells (e.g. He, Ne, Ar), the magnetic moments completely cancel, yielding a net magnetic moment of zero [64].

The presence of four unpaired electrons in the 3d orbital is the reason for the high magnetic moment possessed by Fe atoms. The main types of iron oxide crystal forms that exist in nature are magnetite (Fe₃O₄), maghemite (γ -Fe₂O₃), and hematite (α -Fe₂O₃). The magnetic state of iron-based crystals, e.g. iron oxide crystals, is determined by the relative orientation of the atomic magnetic moments of Fe atoms forming the lattice [61].

Depending on the effect of an external magnetic field on the atomic magnetic dipoles, materials can display three types of behaviors, classified as diamagnetic, paramagnetic or ferromagnetic behavior. [64]

Diamagnetic materials are those composed by atoms having completely filled electron shells or subshells, i.e. inert gases (He, Ne, Ar, etc.) and certain ionic materials. In these atoms, all the electrons' magnetic moments are mutually annulled, and, consequently, they cannot be permanently magnetized. Diamagnetism is a very weak form of magnetism that arises from transitory changes in the orbital motion of electrons induced by the application of an external magnetic field. The resulting magnetic moment is extremely small and oriented in the opposite direction to that of the external field [64].

In paramagnetic materials, atoms possess a net permanent dipolar moment, as a result of the incomplete annulment of the magnetic moment of their electrons. Normally, these atomic moments are randomly oriented, and the crystal does not display any macroscopic magnetization. When an external field is applied, these dipoles align preferentially along the field lines, causing a slight increase of the net magnetic moment, that decay to zero once the field is removed [64].

In ferromagnetic materials, all the atomic moments are aligned between each other, and the material possesses a permanent net magnetic moment even in the absence of an external field. This kind of behavior is typical of transition metals, such us Fe, Co, Ni and Gd. In ferromagnetic materials, coupling interactions between neighboring atoms cause their spin magnetic moments to align with one another without the need of an applied field, whose origin, not yet fully understood, arises from the electronic structure of atoms. This mutual alignment of spins occurs over relatively large portions of the crystal, known as "domains" [64].

Ferromagnetic bulk materials are, indeed, composed of multiple domains, each with a different magnetization orientation. Within each domain, the magnetic moments are parallel, but between adjacent domains they can have different orientations [61].

It is possible to define a magnetization vector (M) for the bulk material, resulting from the sum of all the magnetic moments in the crystal per unit volume. When an external magnetic field (H) is applied, the constituent domains tend to align parallel to the field lines. As a result, M increases with H until a saturation magnetization (M_s) is reached, when all the domains are oriented parallelly to H. When H is removed not all the domains are free to rotate back to their initial orientation, due to energy barriers and inner tensions within the multi-domain material, leading to the persistence of a remnant magnetization (M_s). Only by applying an opposite field having an equal intensity, so-called coercive field (Hc), it is possible to remove M_s . By plotting M vs H for a ferromagnetic material, a hysteresis loop is evident, as represented in *Figure 2.1 A* (blue curve) [61].

The multi-domain organization of bulk ferromagnetic materials arises from the balance between two competing energies, that together determine the size of magnetic domains: the exchange interaction energy, responsible for the atomic moment alignment within each domain, and the magnetostatic interaction energy, which promotes the division into smaller domains with opposite moment orientation. When the dimension of the ferromagnetic material is reduced below a specific critical radius (r_c), the latter contribution becomes insufficient to cause the subdivision into multiple domains, so that the multidomain structure is no longer energetically favorable. As a result, the material transitions to a single-domain system, as shown in *Figure 2.1 B*. This phenomenon is called superparamagnetism [65]. Superparamagnetic nanoparticles are characterized by a sufficiently small size (commonly 1-300nm) that comprises a single crystalline domain, characterized by a preferred axis of magnetization, that depends on particle's crystal structure and shape. [63], [66]. When H is applied, the material reaches high values of magnetization (being intrinsically ferromagnetic) but, at sufficiently high temperatures, the magnetization quickly decays after the remotion of the field like in paramagnetic materials, since the moment is free to rotate. Indeed, M_S is close to zero and any hysteresis loop is observed (see *Figure 2.1 A*, red curve) [61], [65].

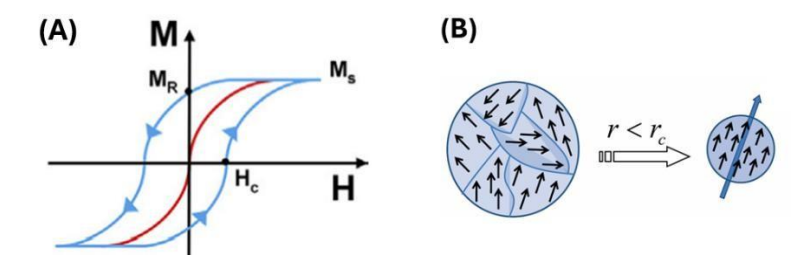


Figure 2.1 (A) Magnetization vs magnetic field intensity graph, showing hysteresis loop for bulk ferromagnetic materials [63]. (B) passaging from a multi-domain ferromagnetic particle to a single-domain superparamagnetic particle when reducing the dimension below the critical size (r_c) [65].

Due to the existence of intrinsic magnetic anisotropy, the magnetic moment of superparamagnetic particles tends to orientate along some preferential direction, called (called "preferred axis" or "easy axis of magnetization"), which depends on the nature and shape of the material [63], [65]. The magnetic energy of magnetic nanoparticles (E) varies with the angle of deviation of the magnetization direction from the easy axis (θ) , according to *Equation 2.1*.

$$E(\theta) = KV(\sin\theta)^2$$
 [Equation 2.1]

where V is particle volume and K is the anisotropy constant, comprising all the different anisotropy contributions. This means that the magnetic energy possessed by a magnetic particle is minimal when θ =0 or θ = π , i.e. when the magnetization direction is parallel with the easy axis of magnetization [63]. These two orientations, referred to as "up" (θ =0) and "down" (θ = π) respectively, are the more thermodynamically stable, since they minimize the magnetic energy, and are equally probable. These two states are separated by an energy barrier (E_b) that has to be overcome to induce the flipping from "up" to "down" or vice versa. In the absence of an external magnetic field E_b=KV [65].

Thermal fluctuations cause fast flipping of the particles' moment between these two states, with a characteristic time (τ), also called "relaxation time" or "super-spin flipping time", expressed by the Arrhenius law, and reported in *Equation 2.2*.

$$\tau = \tau_0 e^{\frac{Eb}{kbT}}$$
 [Equation 2.2]

where k_b is the Boltzman constant, τ_0 is a material-specific relaxation time, dependent on parameters like K and Ms, of the order of $10^{-11} - 10^{-9}$ s, and E_b is the energy barrier that separates the two equilibrium states.[63], [65]

According to Equation 2.2, the characteristic super-spin flipping time strongly depends on the temperature of the system: an increase of T causes an exponential decrease of the characteristic time of super-spin flipping (τ) , while lower T greatly reduces the relaxation time. When T is so high to cause the thermal energy to be greater than the anisotropy barrier $(k_BT >> E_B)$, the super-spin flipping

frequency drastically increases and the particles are in the superparamagnetic state. On the contrary, at very low T (k_BT << E_B), the thermal energy is insufficient to promote the switching of particle's moment to an orientation different from the easy axis of magnetization, and particles are in the so-called blocked state. A threshold temperature, termed blocking temperature (T_b), can be defined to distinguish between the blocked state (T< T_b) and superparamagnetic state (T> T_b). The magnetic state of the system also depends on the order of magnitude of the experimental time scale (τ_{exp}) in which the measure is performed. If the measuring time is larger than the relaxation time (τ_{exp} >> τ) then the particle moment will quickly flip from one orientation to the other, showing a paramagnetic behavior (superparamagnetic state). On the other hand, if τ_{exp} << τ , during the measuring time the particle moment will remain blocked in one of the preferred orientation states (θ =0 or θ = π) dictated by anisotropy energy, and a ferromagnetic behavior is displayed [63] [65]. The threshold is defined at τ_{exp} = τ , so that the blocking temperature can be derived from Eq. 2 as

$$T_b = \frac{K \cdot V}{k_b \cdot \ln(\tau_m/\tau_0)}$$
 [Equation 2.3]

A collection of single-domain nanoparticles in the superparamagnetic state, due to these rapid fluctuations of their magnetic moments, possess a time-averaged magnetic moment equal to zero. Indeed, individual particle dipoles are randomly oriented at any given instant. They only exhibit a net magnetic moment when an external magnetic field (H) is applied, and the individual dipoles' moment spontaneously aligns parallel to it. Under an external field H, magnetic nanoparticles acquire an induced magnetic moment (m) proportional to the particle volume (V), material susceptibility (χ) and H, according to the *Equation 2.4* [63].

$$m = \chi \cdot \mu_0 \cdot H \cdot V$$
 [Equation 2.4]

2.2 Magnetic field-driven self-assembly

Self-assembly is a thermodynamically driven process of organization of structural units (building blocks) such as atoms, molecules or nanoparticles into bigger arrays stabilized against destructive thermal fluctuations via nanoscale forces of interaction inherent to the system. This concept is the core of the "bottom up" nanofabrication approach, which provides a scalable and simple way to fabricate hierarchical structures. For the fabrication of anisotropic magnetic hydrogel, superparamagnetic nanoparticles are used as structural building blocks, and their self-assembly is guided by the application of a uniform magnetic field. The main driving force of this process is the magnetostatic dipole—dipole interaction force [63].

To form structures with a specific directional orientation, i.e. chains or fibers, the interactions between particles must be spatially anisotropic. This type of asymmetric interaction can be efficiently generated through the application of external fields. Electric and magnetic fields are the

most common kinds of fields used to induce attractive interactions between particles, enabling their organization into ordered architectures [67]. Magnetized particles, i.e. particles exhibiting a net nonnull magnetic moment, behave as nanoscale magnets, generating a local magnetic field, as shown in Figure 2.2 A, whose intensity is proportional to the strength of their dipole moment (m). Under the application of an external magnetic field, the strength of the dipole moment is proportional to the intensity of the applied field, as given by Equation 2.4. This local magnetic field interacts with the surrounding magnetic dipoles. Magnetic dipole-dipole interactions between two magnetized particles are "directional", in the sense that they can be either attractive or repulsive, depending on the relative spatial orientation of the two interacting dipoles, defined by the angle δ . A scheme of the interaction between two superparmagnetic particles is presented in Figure 2.2 B. The magnetic field generated by a single magnetic particle produces attractive interactions towards nano-dipoles which are located near the poles along the main magnetization axis ("in line" positioning) while repulsive interaction toward dipoles nearer to the equator ("anti-parallel" arrangement). A schematic representation of neighboring particles interaction types (attractive and repulsive) is provided in Figure 2.2 D. When H is applied, the directional nature of the induced magnetic dipole-dipole interactions give rise to a head-to-tail assembly of the nanomagnets into linear chain-like structures along the main magnetization axis, i.e. direction of the applied external magnetic field (see Figure 2.2C) [66].

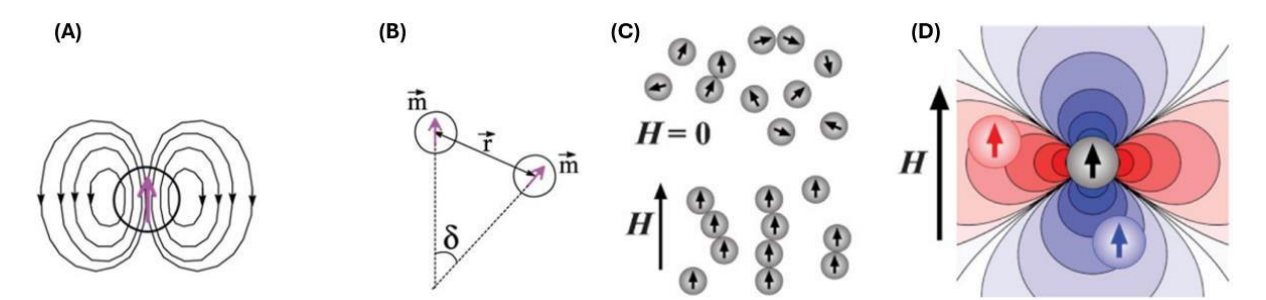


Figure 2.2 (A)Magnetic field lines produced by a single domain ferromagnetic particles; (B) Magnetic interaction between two superparamagnetic nanoparticls; (C) Schematic of the heat-to-tail assembly of magnetic particles under the effect of the application of a magnetic field H (D) Blue regions near the poles of the particle correspond to attraction interaction while red regions near the equator correspond to repulsive interaction [66].

The dipole–dipole energy of interaction between two magnetized particles is defined as the work required to bring these two particles from infinity to a finite separation (r) and is described by the Keesom potential, reported in *Equation 2.5* [63].

$$U_{dd} = \frac{m_1 \cdot m_2 - 3(m_1 \cdot \overrightarrow{r})(m_2 \cdot \overrightarrow{r})}{4\pi\mu_0 r^3}$$
 [Equation 2.5]

where

- m_1 , m_2 are the strength of magnetic dipole moments of the interacting particles
- r is the vector connecting the two particles
- \vec{r} is the unit vector parallel to r

Under the application of an external magnetic field, magnetic interaction energy exceeds thermal fluctuation energy and superparamagnetic nanoparticles spontaneously align their intrinsic magnetic moment along the field direction, so that they are all parallel or antiparallel to each other. The mathematical description of dipole-dipole interaction energy in Eq. 5 explains the directional nature of MNPs interactions in this condition [66]:

- In-line attractive interaction: between magnetic dipoles "in line" (Figure 2.2 D, blue regions), meaning aligned along the line connecting the two dipoles $(m_1//m_2//\vec{r})$, the scalar products became: $m_1 \cdot m_2 = m^2$, $m_1 \cdot \vec{r} = m_2 \cdot \vec{r} = m$, so the interaction energy U_{dd} is attractive and equal to $-m^2/2\pi\mu_0 r^3$
- Anti-parallel repulsive interaction: between magnetic dipoles "anti-parallelly" arranged (Figure 2.2 D, red region), i.e. orthogonally oriented with respect to \vec{r} (m₁//m₂ $\perp \vec{r}$), the scalar products became: $m_1 \cdot m_2 = -m^2$, $m_1 \cdot \vec{r} = m_2 \cdot \vec{r} = 0$, and the interaction energy U_{dd} is repulsive along the connecting direction and equal to $m^2/4\pi\mu_0 r^3$

The force of the dipole-dipole interaction is defined as $F=-\nabla U_{mag}$, thus it is scaled as r^{-4} . As it strongly decreases with increasing inter-particles distance, it only acts over a short range. The dipole moment of a superparamagnetic particle immersed in a magnetic field H, as given by Eq. 4, is proportional to particle's volume. Therefore, also the strength of the dipole-dipole interaction force scales with the volume. Increasing particles' dimension, the dipolar interaction force rises. On the contrary, for very small particles the same force could be insufficient to promote their ordered self-assembly [68]. As an example, for iron oxide particles smaller than 7 nm this energy became smaller than the thermal energy kT, and the randomizing effect of Brownian motion dominates over the attractive magnetic force [66].

Additionally, for one magnetic particle immersed in an external magnetic field H, its magnetic energy (U_m) is given by *Equation 2.6*.

$$U_{\rm m} = -\mu_0 mH$$
 [Equation 2.6]

The magnetic force acting on this nanoparticle is described as a gradient of the energy, $F_m = \nabla(mH)$, directly proportional to particles' volume and the gradient of the external field magnitude. Consequentially, magnetic particles are forced to move towards regions with greater field intensity. This phenomenon is referred to as positive magnetophoresis and it only occurs if there is gradient in the applied field [70].

To summarize, under the application of an external magnetic, the magnetic interaction energy exceeds the thermal fluctuation energy and magnetic nanoparticles tend to align their intrinsic magnetic moment along the field direction. After that, magnetic particles start interacting with each

other and arrange into chain-like aggregates to minimize the energy interaction between their magnetic moments. Once the field is removed, particles lose their arrangement because their dipoles are no longer constrained to align with the field direction and relax back to random orientations under thermal fluctuations. The only way to preserve the fibrous arrangement in the absence of a magnetic field is by means of the phase change of the surrounding environment, e.g. matrix sol-togel transition [69].

2.3 State-of-the-art of anisotropic magnetic hydrogel

Hu et al. leveraged the field-guided self-assembly to develop composite hydrogels with improved magnetothermal properties, thanks to the enhanced magnetic interaction between linearly aligned nanoparticles [70]. Commercially available superparamagnetic Fe₃O₄ particles, capped with carboxylated SiO₂, were dispersed inside a solution of acrylamide/bis-acrylamide monomers and exposed to a uniform magnetostatic field of 80 mT for 5-30 minutes before and during the gelation. The polymerization of the hydrogel matrix was activated by heating the monomer solution at 50°C, leading to the immobilization of the embedded chain-like assemblies, as schematically illustrated in *Figure 2.3*.

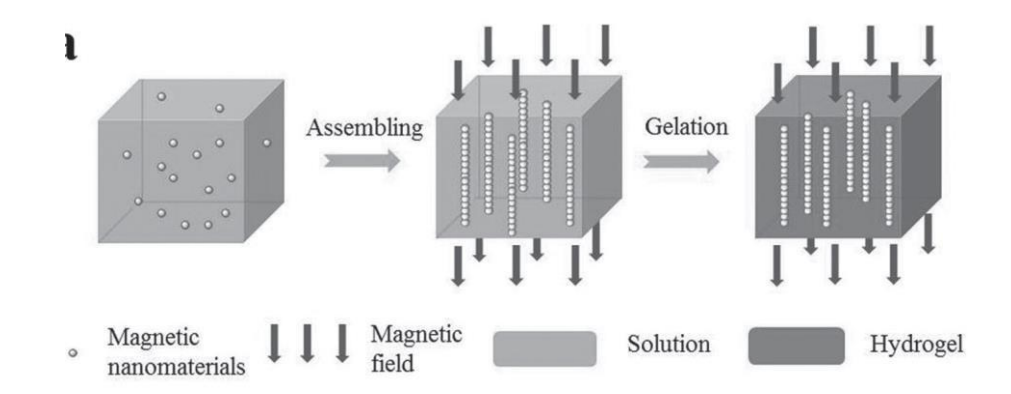


Figure 2.3 Schematic of the three-step process to fabricate magnetically-patterned anisotropic hydrogel, leveraging magnetic field self-assembly followed by matrix gelation [70]

The authors outline the suitability of heat-induced gelation method to preserve the morphology of IOPs arrangements, as it does not require processes that could interfere with the programmed magnetic microstructure, such as the addition of molecules or stirring. Also, they compared the use of two sized magnetic building blocks (15nm vs 200 nm), concluding that particles with larger volume result in better morphology of the assembled chains, as a consequence of their higher dipole-dipole interaction. The magnetic force on 15 nm nanoparticles, instead, failed to overcome the thermal perturbations and generate aligned structures. Finally, they reported that the nanoparticles concentration greatly affects the final morphology, with higher concentrations accelerating the self-assembly process [70]. However, their proposed approach is not suitable for the simultaneous

embedding of cells, due to the high temperature required for hydrogel gelation. Ensuring nontoxicity and biocompatibility of the manufacturing process is a major challenge toward the fabrication of multifunctional hydrogel aimed to incorporate living cells [61].

In another study, a magnetic anisotropic hydrogel based on the PEGDA–GelMA was developed to promote the differentiation of stem cells toward osteogenic phenotype. Similarly to skeletal muscle, bone tissue comprises highly ordered, hierarchically organized collagen fibers, whose precise anisotropic arrangement is at the base of tissue's mechanical properties and biological functions [49]. The hydrogel prepolymerization solution was realized by mixing 15 wt% PEGDA, 5 wt% GelMA, 0.6 wt% N,N-methylene-bis-acrylamide (MBA), and 1 wt% lithium phenyl-2,4,6-trimethylben-zoylphosphinate (LAP), together with 2 mg/mL γ-Fe₂O₃@ PSC/PLL colloidal solution. This solution was poured into a mold and placed in between two the poles of a pair of electromagnets before photo-polymerization. Composite hydrogels were then freeze-dried, sliced parallelly to the assembled magnetic chains and seeded with human bone mesenchymal stem cells (BMSCs), as shown in *Figure 2.4*. The presence of parallel assembled chains conferred anisotropy to the network structure, and BMSCs exhibited a preferential alignment along the magnetic chains' direction. Stem cells cultured on anisotropic scaffolds exhibited enhanced differentiation compared to those on isotropic substrates, with higher expression levels of some osteogenesis-related genes.

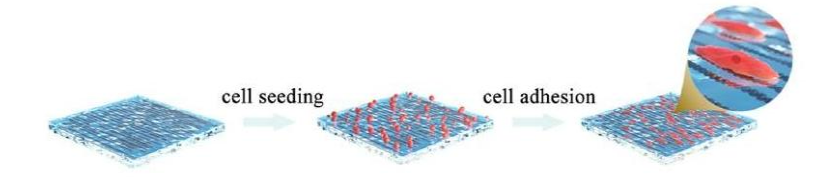


Figure 2.4 Schematic illustration of cell seeding and adhesion on anisotropic scaffolds [49]

A major limitation of this approach is that cells are seeded on the scaffolds only after its fabrication, and they are not embedded within the hydrogel matrix. This reduces the system to a less biologically relevant 2D culture on the scaffold surface and does not fully exploit the potential of hydrogels to encapsulate cells and bioactive fillers in an ECM-like 3D environment.

Kim et al. established a newel method to bio-fabricate cell-laden, nanocomposite hydrogels endowed with anisotropic, cell-guiding functionalities [69]. ECM-coated superparamagnetic particles (ECM-IOPs) of 300 nm were used to program topographies in 3D biomaterials, with the aim to dissect the role of anisotropic spatial guidance provided by fibrillar geometries on cells dendritic extension. NIH 3T3 fibroblasts and PC12 neural cells were used for the study. ECM-IOPs were mixed with cells in liquid Matrigel. The assembling process was performed on ice to maintain Matrigel in a liquid state and enable the field-induced alignment of the embedded particles. Then

the matrix was gelled by incubating at 37 °C for 25 min. A schematic of the bio-fabrication steps is reported in *Figure 2.5 A*.

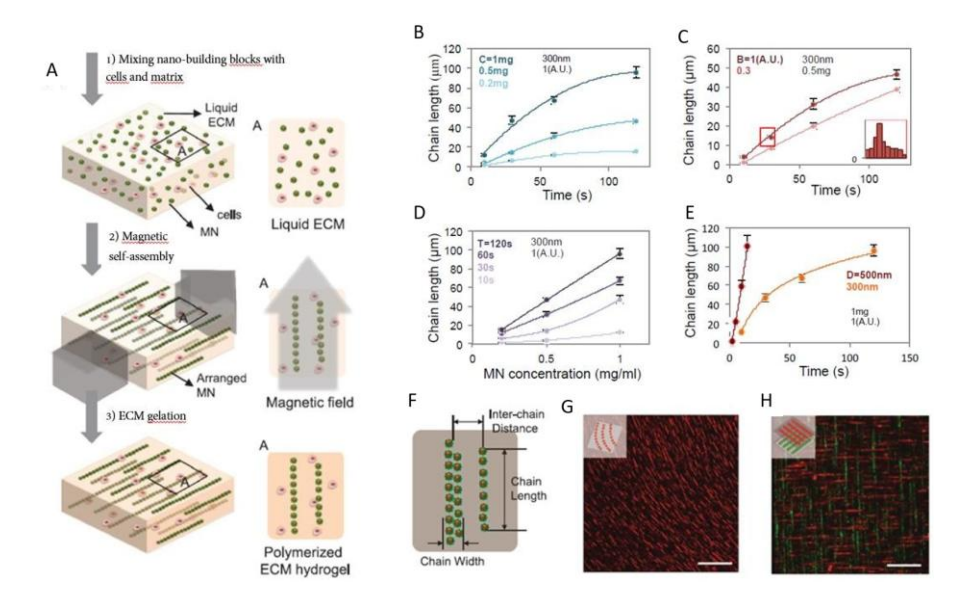


Figure 2.5 (A) Illustration of the bio-fabrication approach. (B)-(E) Results of the effect of magnetic nanoparticles concentration and diameter, magnetic field application time and matrix viscosity on the self-assembly profile; (F) dimensions that characterized the self-assembled microstructure: chain length, width and inter-chain distance (G) curvilinear NNs pattern and (H) NPs patterns varied from one polymerized layer to the other

The authors pointed out the extraordinary ease of engineering 3D hydrogels with various microscale topographic geometries, by playing with the spatial distribution of the applied magnetic field. Indeed, MNPs field-induced self-assembly follows the same direction of the field lines, not necessarily straight. As a proof of concept, they created a curvilinear NPs pattern by modulating the curvature of the applied magnetic field (see *Figure 2.5 G*), and also showed that the NPs-pattern can be varied from one layer to the other by altering the magnetic field in sequential matrix polymerization steps (*Figure 2.5 H*), demonstrating the great versatility of the self-assembly approach. Additionally, they provided an extensive investigation of the effect of magnetic nanoparticles concentration and diameter, magnetic field application time and matrix viscosity on the self-assembly profile. Results (summarized in *Figure 2.5 B-E*) show that particles chains' length and inter-fibers distance increases with the duration of the applied magnetic field, and that the self-assembling profile is critically affected by the rheological properties of the host matrix, speeding up at lower viscosities. In *Figure 2.5 F* the main geometrical descriptors of the self-assembled structures.

Both NIH 3T3 and PC12 cells grown in the anisotropic matrices aligned along the direction of the nanofibers and displayed longer protrusions, differently from cells cultured in isotropic hydrogels. This result suggests that topography may be a physical stimulus capable of guiding cellular exploration and growth [69].

In another example, Tognato et al. developed cellularized anisotropic hybrid hydrogels through a mild and biocompatible process that leverages magnetic field, temperature, and light [71]. PEG-capped iron oxide nanoparticles (IOPs) with a diameter in the range of 40-60 nm were dispersed within a liquid GelMA solution (at T > 37 °C) and aligned into size-tunable filaments by an ultra-low-intensity magnetic field (20mT) for 30 minutes, finally photo-polymerized through 10 minutes of UV irradiation, to permanently stabilize the anisotropic organization of the self-assembled IOPs filaments. Three matrices were compared: bare GelMA (G), GelMA incorporating randomly dispersed IOPs (GRIOPs) and aligned IOPs filaments (G/AIOPs). Human mesenchymal stem cells (hMSC) were seeded on the top of the hydrogels, while C2C12 (myoblasts cell line) were embedded.

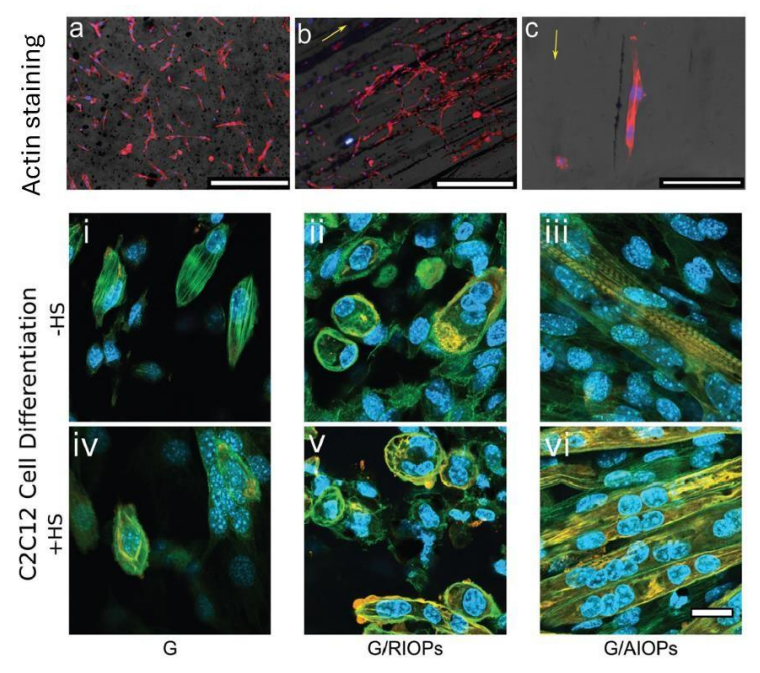


Figure 2.6 Fluorescent image of hMSCs labeled for actin seeded on top of a GelMA hydrogel loaded with a) randomly dispersed IOPs b) aligned IOPs after 24 h. Scale bar = 400 μm. c) Higher magnification fluorescent image of hMSC seeded on top of the anisotropic material, clearly showing the preferential alignment of the cells along the magnetic fibers. Scale bar = 100 μm. The yellow arrows indicate the IOPs filament direction [71].

Also in this case, the presence of spatially organized mechanical cues was effective in orchestrating an anisotropic cytoskeletal arrangement of cells, preferentially aligned along the magnetic fibers (see *Figure 2.6 a-c*), both in 2D (hMSC) and 3D (C2C12) culture conditions. This physical guidance drastically improved scaffold's functionality, as it promoted C2C12 early maturation toward multinucleated myotubes. Remarkably, even in the absence of differentiation medium (HS-), cells underwent differentiation into mature myotubes when cultured in G/AIOPs, as assessed by MyHC expression (marker of skeletal muscle differentiation), absent in G/RIOPs and G matrices (see *Figure 2.6 i-ii*) Instead, when differentiation medium (HS+) was used, C2C12 encapsulated inside G/AIOPs hydrogels showed improved myotube organization, with higher level of MyHC expression, compared to G/RIOPs and G groups.

An additional step forward of this work is to provide a proof-of-concept of the applicability of their nanocomposite hydrogel as a 3D printing ink, showcasing its potential for fabricating intricate 3D structures via light-based 3D printing technologies.

The integration of additive manufacturing technologies with the remote manipulation of magnetic fillers incorporated in the hydrogel bio-ink allows the automated fabrication of intrinsically anisotropic living constructs, with a high control over macroscopic geometry. This concept, known as "magnetically-assisted 3D (bio)printing", is based on the contemporaneous application of an external magnetic field on the (bio)ink during the printing process to guide the arrangement of magnetic materials within the printed structures, and holds the potential to improve the versatility and reproducibility of the magnetic pattern approach (bottom up), compared to the use of traditional fabrication methods [54], [61].

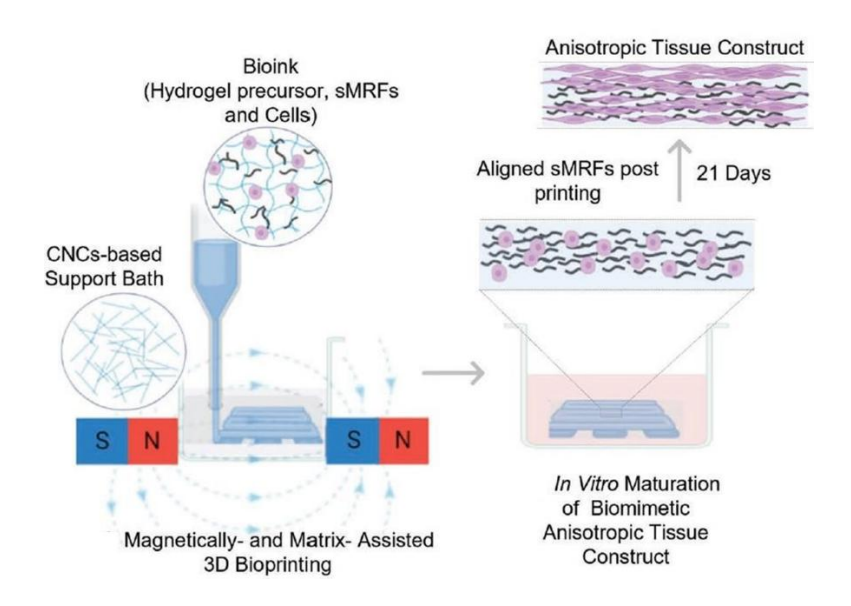


Figure 2.7 Schematic illustration of the proposed strategy to fabricate high-resolution anisotropic biomimetic constructs [72].

Pardo et al. proposed an innovative strategy to combine extrusion-based 3D printing technology with magnetic hydrogel bio-ink to engineer high resolution composite constructs endowed with programmed anisotropic topographical cues [72]. Magnetic bioinks were created by mixing GelMA, short magnetically responsive microfibers (sMRFs) and human adipose-derived stem cells (hASCs), and extruded into a shear-thinning, support baths, under the application of low-strength magnetic fields. This system allows the bio-ink fibers to remain viscous long enough after printing to enable the magnetically-induced arrangement of the fillers. A schematic of the magnetically-assisted printing process is proposed in *Figure 2.7*.

A noteworthy contribution in the field of magnetic nanocomposite 3D printing was reported by Lantean et al., who developed a Digital Light Processing (DLP) - based approach to fabricate

magneto-responsive polymeric materials [73]. A detailed description of the DLP method will be provided in the following chapter, focused on additive Manufacturing technologies. This work leverages the self-assembly of magnetic particles within a photocurable resin matrix, enabling microstructural programming layer-by-layer during the printing process. However, this example does not fall within the framework of tissue engineering strategies aimed at directing cell response. Instead, the study aimed to explore the 3D printing of geometrically intricate objects with enhanced magnetic responsivity, demonstrating complex and precise magnetically actuated movements under external magnetic fields.

3. Additive manufacturing (AM)

The term "additive manufacturing" (AM) is referred to a set of technologies allowing for the automatic creation of solid objects from a computer-aided design (CAD) file description. They all build the object layer-by-layer (thus called "additive"), leveraging a method-specific physical principle. AM technologies were originally intended to produce physical prototypes of products in short times, to evaluate manufacturability and design effectiveness. With time, they have started to be employed as methods for actual product manufacturing, offering great advantages compared to traditional approaches. One of the most important is the possibility to personalize the fabricated objects. That's extremely important, for example, in the field of biomedical engineering, where prosthetic devices can be designed based on the scanned measurements of the patient [74]. The general process begins with the creation of the 3D model, using a CAD software (e.g. SOLIDWORKS, AutoCAD, etc.), which is then converted into a *.stl (Standard Tessellation Language) format and sliced into layers by a dedicated software (slicing software), that generates the G-code as output [75]. G-code is a programming language that can be read by the machine and contains the set of actions that the AM machine must take to build the part [76]. This workflow, schematized in Figure 3.1, allows for a great level of automation and reproducibility.

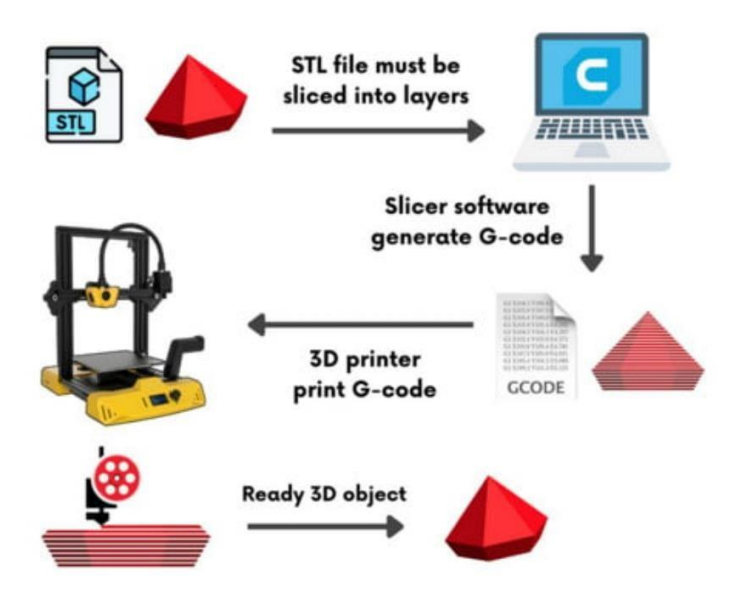


Figure 3.1 General workflow of an AM process [76]

In principle, all the materials can be used with some AM technology, ranging from rubber like polymers to metals and ceramics. Notably, polymeric materials are the most employed [74]. When referring to polymer additive manufacturing, the term "3D printing" (3DP) is used. [77].

An emerging application of 3DP technologies is that of "bio-printing", referred to the printing of living cells suspended in a liquid material (or "bioink") [74]. Differently from conventional fabrication methods, bio-printing strategies enable us to mimic the hierarchical and intricate architectures of native tissues, thanks to the spatiotemporally controlled deposition of cells and biomaterials (i.e. hydrogels) into precise 3D geometries, thus greatly improving the physiological relevance of TE models. [78].

3.1 3D-Printing overview

The American Society for Testing and Materials (ASTM) recognized the existence of more than 50 AM technologies and categorized them into seven different groups: material extrusion, material and binder jetting, vat photopolymerization, powder bed fusion, sheet lamination, and direct energy deposition [79]. Among these, the 3D printing categories mainly employed for biofabrication purposes to date are inkjet-based (derived from material jetting), extrusion-based and Vat Polymerization [78]. For the scope of this thesis, only these three AM approaches will be briefly described in the following paragraphs. Then, an entire section (3.2) will be dedicated to Vat polymerization. A scheme of the mentioned bioprinting processes is reported in *Figure 3.2*, where inkjet- and extrusion- based methods are grouped into the more general category of deposition approaches [80].

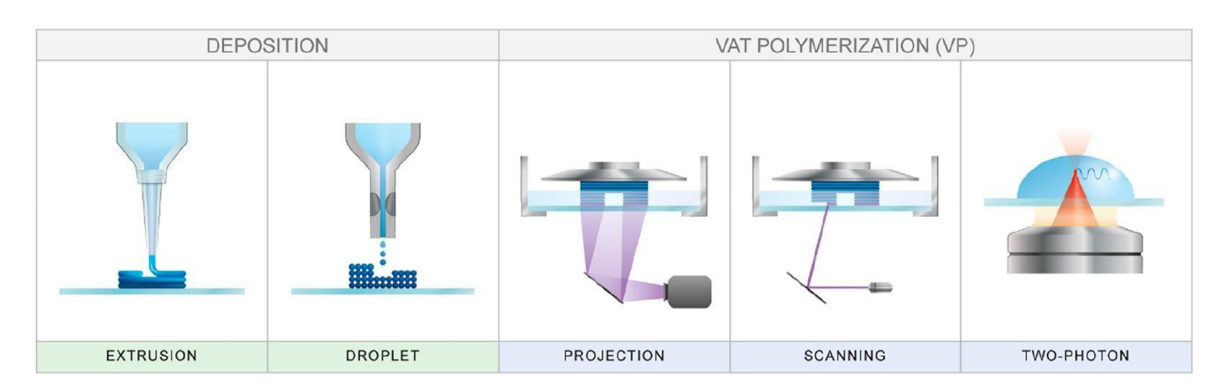


Figure 3.2 Scheme of the most common 3D (bio)printing technologies [80].

Extrusion-based 3D printing is a family of 3DP techniques in which the material is extruded through the small orifice of a printing head and deposited on a build platform in a layer-by-layer fashion. The filament deposition follows the pre-determined path of the printing heat along the x-y plane. After the completion of each layer, the build platform is lowered (or the print head is raised) of a defined z-step, and a new layer of filament is deposited on the top of the previous one. This general approach offers advantages such as cost effectiveness and ease of use [74]. The most diffused implementation is the Fused Filament Fabrication (FFF) process, based on the extrusion of a thermoplastic polymer filament through a heated nozzle. Once deposited, the filament cools down, solidifies and adheres to the underlying surface, i.e. the build platform (for

the first layer) or the previously deposited layer. FFF suffers from relatively low resolution, limited by the filament diameter (200-1000 m), and high surface roughness, due to the layers' superposition effect [81]. Also, the realization of overhanging parts requires the printing of additional support structures that have to be removed in a post-processing phase. The extrusion-based approach can be applied with viscous bioinks, to realize extrusion-based bio-printing, i.e. bioplotting. Different strategies are employed to drive the dispensing of the filament: pressure-based control, solenoid control and mechanical control. The volume of extruded ink is immediately polymerized by physical or chemical cross-linking. Both thermosensitive and light-sensitive polymer can be used as ink materials. When applied for bio-printing living tissues, two additional drawbacks are frequent clogging of the nozzle and the shear stress induced during the extrusion, that can damage encapsulated cells [78].

- Material Jetting works by depositing very small ink droplets with precise control. Typical printing speeds are of the order of mm s⁻¹ and the best reported resolution is $20 \,\mu\text{m}$. Inkjet printing technologies can be further classified on the base of the mechanism employed to produce the ink droplet: continuous-inkjet printing, drop-on-demand printing and electro-hydrodynamic jet printing, each with different characteristics in terms of control over droplet deposition. The main advantages of general inkjet-based bioprinting are the quite high printing speed, precise deposition, smooth surfaces and low cost. The limits are the easy clogging of the nozzle at high cell densities, the small nozzle aperture, the low-viscosity requirement for printing, thermal stress induced cell damage and low printing resolution, resulting from the point-by-point deposition approach [78]. A well-known implementation is the PolyJet technology, in which the print-head contains multiple nozzles, thus allowing for the simultaneous deposition of droplets of different materials, and for the deposition of support structures that do not solidify during the printing, and can be easily washed or blown away. PolyJet technology enables high surface quality but suffers from limited size and brittleness of the printed objects [81].
- 3) <u>Vat Polymerization (VP)</u>: is a family of AM technologies whose functioning is based on the spatiotemporally controlled exposure to light, and consequent solidification, of a photosensitive liquid resin contained in a vat. They utilize light beams to selectively hit and cure a liquid photopolymer resin in precise locations to create a solid part. They are also commonly referred to as light-assisted 3D printing methods [77]. Compared with extrusion- and ink- based techniques, VP can achieve high printing resolution and accuracy, faster printing times and are more suitable for cell-encapsulation applications [78].

Different photochemical reactions exist, indeed, that are relatively fast and can be performed in water under physiological conditions, eventually suitable for cell encapsulation with limitedcytotoxic effects. Photosensible hydrogel precursors are used as polymeric component of

bioink [80]. In *Table 3.1* the main features of deposition techniques and Vat Polymerization techniques are summarized.

Table 3.1 Comparative table between deposition (green) and vat polymerization (blue) techniques [80].

	DEPOSITION		VAT POLYMERIZATION	
	Extrusion printing	Droplet printing	Projection VP	Two-photon stereolithography
Max. structure size	cm	cm	cm	mm
Average time to print 1 cm³ block	20 min	N.A.	1 hr	Days
Typical feature size	100-600 μm	50-500 μm	25 - 150 μm	100 nm – 1 μm
Multimaterial	***	***	*	*
High throughput	**	***	**	*
Typical viscosity of ink/resin	10,000 Pa·s	<15 mPa·s ^a <200 mPa·s ^b	10 – 5000 mPa·s² <90,000 mPa·s²	Viscosity-independent
Cost of device (\$)	30-250k	5k	30k-50k	90k – 500k

3.2 Vat polymerization printing

Also known as light-based 3D printing, Vat polymerization (VP) builds its foundation on the synergistic combination of versatile polymer chemistry and precise light manipulation to achieve exquisite spatiotemporal control over the process of polymerization of a liquid photopolymer system (called "resin"), which locally triggers the liquid-to-solid transition. Thus, by accurately controlling the movement of the incident light, the liquid resin contained in a vat is selectively hit and cured, allowing the solidification of 3D objects with precise features. Among the traditional (layer-by-layer) VP technologies, the most common are Stereolithography (SLA) and Digital Light Projection (DLP). Since they both utilize the simplest form of single-photon photopolymerization, the liquid-to-solid transition only takes place at the surface (or bottom) of the vat, where the incident light dose is the highest. This implies that the only way to build a 3D object is through the gradual stacking of successive outermost layers, with a liquid resin replenishment step following each layer polymerization. The single-photon polymerization mechanism underlies a linear relationship between polymer conversion and incident light dose. A significant advancement in the VP field arose from the introduction of chemical and/or optical nonlinearity to the photopolymerization process, which are at the base of volumetric additive manufacturing (VAM) [82]. VAM has been defined by Thijssen et al. as "a process that enables freeform conversion of precursor material at an arbitrary position within a volume of material, without requiring

secondary operations that relocate precursor material (i.e., absence of relative motion within the material)" [82].

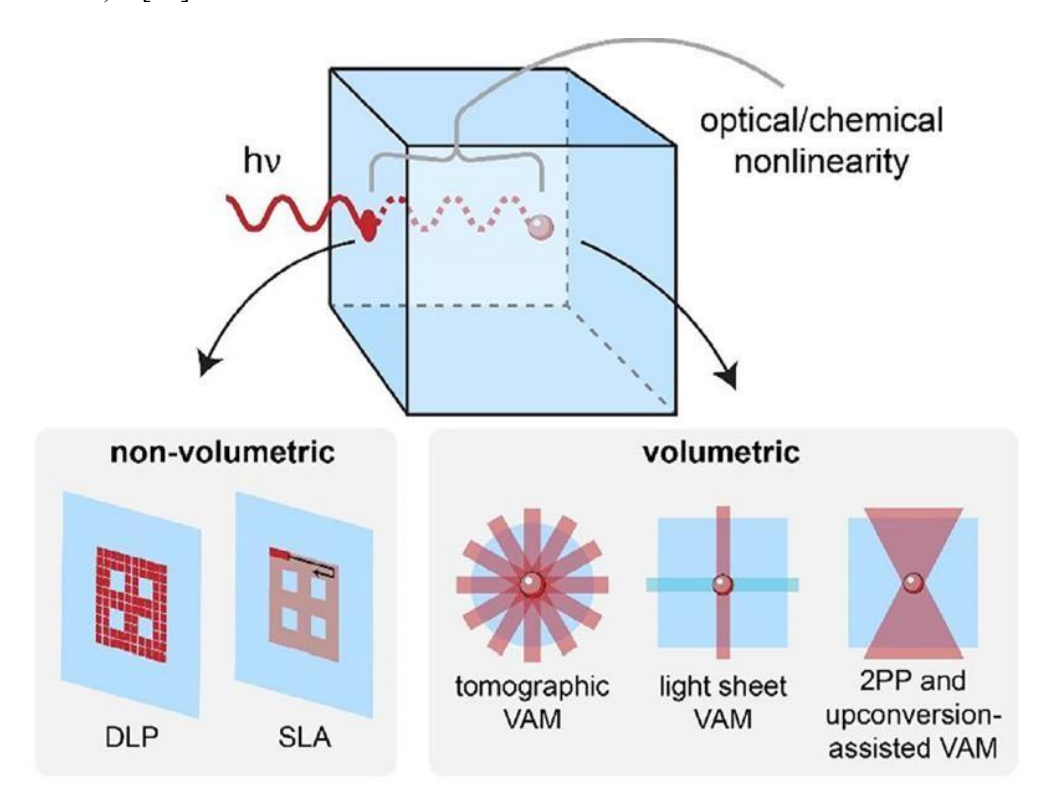


Figure 3.3 Schematic illustration showing the difference between non-volumetric VP, where the curing is confined to the resin's surface, and volumetric VP, in which optical/chemical nonlinearity shifts photopolymerization from the surface to any chosen point within the resin volume, thus enabling volumetric 3D printing [82].

This novel VP approach allows the creation of very complex shapes devoid of layering artefacts (intrinsic of layer-by-layer approaches), enabling outstanding improvement in printing speed and resolution. Additionally, VAM holds unmatched potential in the field of bioprinting, thanks to the combination of short residence time of the bioink, complete absence of shear stresses and minimal PI content required. Among the different technologies implemented in the field of VAM, the current state of the art is led by computed axial lithography (CAL), two-photon polymerization (2PP) and light-sheet VAM, of which Xolography represents first implementation to date. A schematic of the different modalities of light manipulation in traditional layer-bylayer and volumetric approaches is provided in *Figure 3.3*.

Before providing a more detailed description of each mentioned VP technologies (SLA, DLP, CAL, TPP and Xolography), the theoretical background of the photopolymerization mechanism will be here introduced.

3.2.1 Photopolymerization

The term "photopolymerization" refers to the process chain polymerization of pre-existing macromolecules (e.g. monomers, oligomers, and polymers), initiated by the absorption of light as the energy input. This process requires the presence of three main elements: photo-initiators, photo-crosslinkable macro-molecules and a source of light, shown in *Figure 3.4* [83]. Photoinitiators (PIs) are chemical compounds that, upon absorbing light at specific wavelengths, typically in the ultraviolet (UV) –visible range (250–450 nm), generate reactive intermediate species (free radicals or ions) that react with the functional units (monomers and/or oligomers), propagating the formation of covalent bonds (chemical cross-linking) and the growth of a polymer network [83], [84].

A photopolymerization reaction is typically divided into three steps: initiation, propagation and termination, as illustrated in *Figure 3.4* [77].

- 1. <u>Initiation</u>: upon light irradiation, PI generates reactive species.
- 2. <u>Propagation:</u> the generated reactive species react with monomers, leading to the formation of the polymeric chains, or networks, with increasing molecular weight.
- 3. <u>Termination:</u> the step in which the reaction of polymerization ends

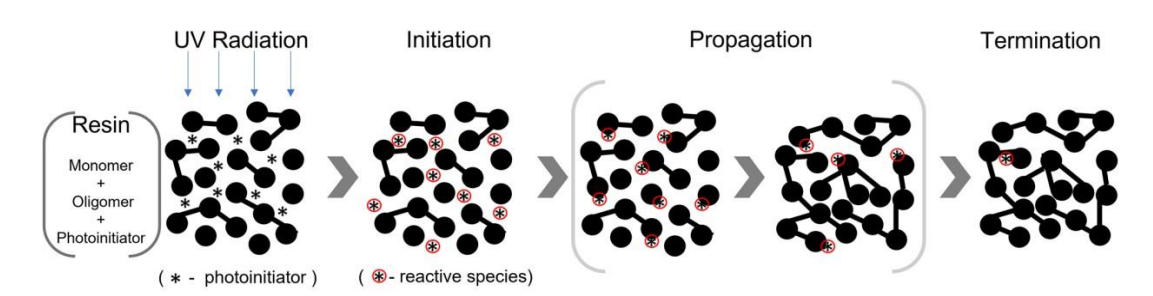


Figure 3.4 steps of photopolymerization of a typical resin for VP 3D printing, comprising monomers (single spheres), oligomers (connected spheres) and photoinitiator(stars) [85].

1) The initiation only occurs if the wavelength of the incident light falls into the absorption band of the PI. If that happens, light promotes one electron of the PI to a higher energy orbital, causing its transition to an electronically excited state (PI*). This highly unstable molecule can follow three main possible paths. (see *Figure 3.5*)

$$PI \stackrel{O_2}{\longleftarrow} PI + O_2^+$$

$$I \stackrel{\bullet}{\longleftarrow} (or \ I^+)$$

Figure 3.5 Scheme of the three possible routes an exited PI species (PI*) can follow [83].

1. PI* can decay back to its original state (PI), upon the emission of light and heat. This spontaneously happens after a PI-specific lifetime, usually around 10⁻⁶ s.

- 2. PI* can react with oxygen (O₂) and go back to its PI form
- 3. PI* can chemically react with another species (I) yielding the formation of a reactive intermediate: a free radical (I*) or a cationic species (I⁺).

This reactive intermediate, in turn, can react with another radical (R), with O₂, or react with existing monomers (M), thus initiating the polymerization (see *Figure 3.6*).

$$I - R$$

$$I \circ \bigcup_{0_2} I - R$$

$$I \circ \bigcup_{0_2} IO_2$$
Polymer

Figure 3.6 scheme of the possible paths that a reactive intermediate species can follow [83].

The presence of oxygen reduces photopolymerization's efficiency by reducing the available amount of both reactive PI* molecules and initiating species I*, due to its competing reaction with them. For this reason, photopolymerization is harder to achieve in air (effect known as oxygen inhibition) [83]. That inhibition mechanism can also be positively exploited in CAL, as it will be discussed [82].

Depending on the specific mechanism through which the excited photo-initiator molecule PI* generates the reactive radical (I*), photo-initiator systems can be classified into type I and type II, as shown in *Figure 3.7* [84].

- Type I photo-initiators are photo-cleavable chromophores (or dyes), in which a chemical bond is cleaved upon the absorption of light, yielding two free radicals, e.g. benzoin derivatives
- <u>Type II photo-initiators</u> are non-cleavable compounds (or dye) that need the help of a hydrogen-donor molecule, called co-initiator. Upon light absorption, a type II PI subtracts hydrogen (H) from the coinitiator (D-H), generating the initiating radicals D*. Amines are a classical example of co-initiator molecules, as they easily donate hydrogens in alpha position [84].

$$\frac{dye}{R_1 - R_2} \xrightarrow{h\nu} {}^{1,3}dye \xrightarrow{\qquad} R_1^{\bullet} + R_2^{\bullet} \xrightarrow{\qquad} Type I$$

$$\frac{dye}{dye} \xrightarrow{h\nu} {}^{1,3}dye \xrightarrow{\qquad} D^{\bullet} + dyeH^{\bullet} \xrightarrow{\qquad} Type II$$

Figure 3.7 schematic representation of the different mechanisms through which type I and type II photoinitiators generate the active radicals to initiate the polymerization [84].

2) The propagation begins when the initiating species react with monomers (or oligomers), generating new reactive macromolecules. These, in turn, react with additional unreacted monomers (or oligomers), leading to the formation of a growing polymer with an increasing

molecular weight. 3) The termination of the polymerization process is due to three possible causes: recombination, disproportion or occlusion [85]. The first two termination mechanisms involve the interaction of two propagating macro-molecular species (P*), both leading to radical deactivation. The third one results from the progressive decrease of mobility of the propagating species within the growing polymeric network [84].

The most common polymerization mechanism harvested for vat 3DP is polyaddition (chain-grow mechanism), in which unreacted monomers are progressively added to the growing propagating chain, as schematically reported in *Figure 3.8 A*. Typical monomers used in this process include (meth)acrylates, (meth)acrylamides, and vinyl esters, which are endowed with unsaturated bonds (-C=C-) (See *Figure 3.8 A1, A2*) [77]. Methacryloyl-based monomers (e.g. gelatin-methacryloyl or hyaluronic acid methacrylate) are the most commonly employed, possessing a polymerizable double bond at the a,ßunsaturatedcarbonyl position. Typically, they are synthesized through esterification or amidation reactions, in which methacryloyl chloride or methacrylic anhydride reacts with the hydroxyl or amino groups present in natural polymers. (e.g. gelatin, hyaluronic acid etc.) [80] In 3DP applications, monomers possessing at least two reactive functionalities are needed, as they allow for the rapid formation of densely crosslinked polymeric networks, insoluble in the surrounding unreacted monomers mixture. Monofunctional monomers are not suitable, because they only form linear polymeric chains, which are soluble in their monomer solution [77].

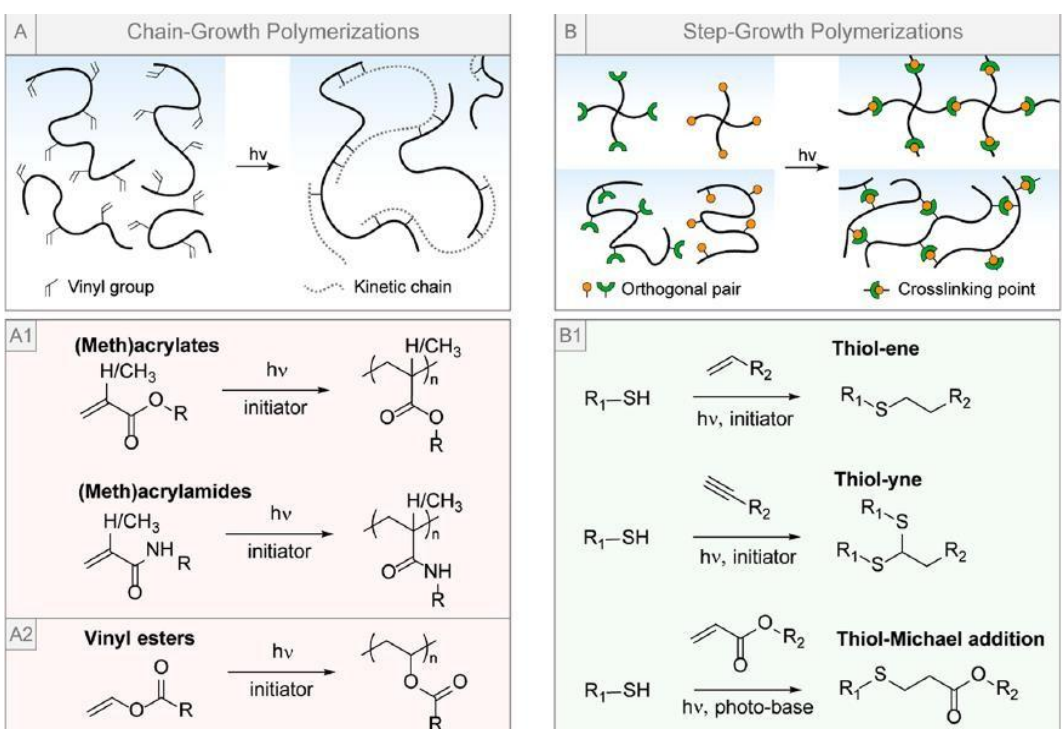


Figure 3.8 Schematic illustration of polymer network formation via (A) chain-growth and (B) step-growth mechanisms. Examples of photochemical "constructive" reactions used to form and functionalize hydrogels in 3D biofabrication include: (A1) (meth)acrylates and (meth)acrylamides; (A2) vinyl esters for chain-growth, and (B1) thiol—ene, thiol—yne, and thiol—Michael addition reactions for step-growth. from Lee et al. [80].

The main advantages of chain-growth radical polymerization are (i) its fast reaction kinetics, which is advantageous for hydrogel 3D printing, and (ii) the wide range of commercially available monomers, allowing for precise tuning of chemical and mechanical properties. On the other hand, this mechanism is highly sensible to oxygen inhibition: propagating radicals readily react with dissolved oxygen, forming inactive peroxides that slow or halt polymerization. Another drawback is its diffusion-controlled kinetics: as polymerization proceeds, the mobility of radical chain ends becomes limited, leading to reaction-diffusion-controlled growth, which often results in network heterogeneity. Also, the reduced mobility of the propagating species can cause the termination of the polymerization before the total conversion of functional groups, leading to significant amount of unreacted double bonds, which negatively affect the viability of encapsulated cells in bioprinting applications. Highly crosslinked hydrogels tend to undergo volume shrinking and internal stress formation during curing.

Alternatively, the step-growth mechanism can be also exploited (e.g. thiol-ene based polymers). The highly efficient reaction between thiol groups and reactive carbon—carbon double bonds has proven versatile for the formation of hydrogel networks from photo-cross-linkable precursors. In this case, each reaction step occurs between two distinct reactive species, and there is no continuously growing chain (see *Figure 3.5 B*). This propagation mechanism is less affected by oxygen inhibition and gives rise to more uniform networks. However, it is way slower than the chain-growth mechanism, it requires stoichiometric balance between reactive groups and suffers from very limited monomer availability. However, a detailed explanation of this mechanism is out of the aim of thesis and can be found in literature [86].

3.2.2 Stereolithography (SLA)

A UV beam is generated by a laser source and focused on the surface of the layer of liquid resin. A system of dynamic mirrors is used to move it in the x-y plane, to scan the liquid layer in a point-by-point fashion, i.e. one pixel at the time [87]. The pattern of liquid resin layer hit by the laser cures and solidifies, giving rise to a solid slice of the 3D object [74]. After the completion of the first layer, the build platform is moved along the z-axes of an increment-step equal to the intended layer thickness, so that a new film of liquid resin can be deposited on the previous one (replenishment). The process repeats until the part is complete. Two different machine configurations exist, depending on whether the platform movement at each replenishment step occurs upward (bottom-up) or downward (bottom-up). In the former case, the light source is positioned beneath the vat and irradiates the layer of resin comprised between the platform and the bottom of the vat. Whereas, in the latter case, the laser beam lights up the resin surface from above, and the solidified layer is comprised between the platform and the free surface [87]. Both

configurations are shown in *Figure 3.9 A*, *B*. The step size must be small enough to guarantee light penetration throughout the layers' height, but not too small to cause over-curing outside the layer's thickness. Layer thickness and time of irradiation must be optimized to reach a tradeoff between short printing times and high resolution. The vertical resolution is principally determined by the precision of the vertical motion of the build plate. First layers usually require longer irradiation times to ensure their stable adhesion to the plate, and prevent their detach during platform movement [77].

3.2.3 Digital light processing

Digital Light Processing is a layer-by-layer VP technology whose working principle is identical to that of SLA, with the only difference that the light source is not a single-point laser but a digital light projector emitting in the UV-vis range. The key element is a Digital Mirror Device (DMD), composed of millions of micrometric mirrors that can be independently oriented to direct light onto the resin. In this way, the entire section of each layer polymerizes in a single step, thus critically reducing printing times compared to SLA, being in the order of cm³ h⁻¹ [88]. Each micron-sized mirror creates a pixel of the 2D image projected onto the resin layer, that can be on or off, and whose size determines the resolution on the XY-plane (25 μm) [85]. In the same way of SLA, DLP printer can be configurated in bottom-up or top-down, as shown in *Figure 3.9 C,D*.

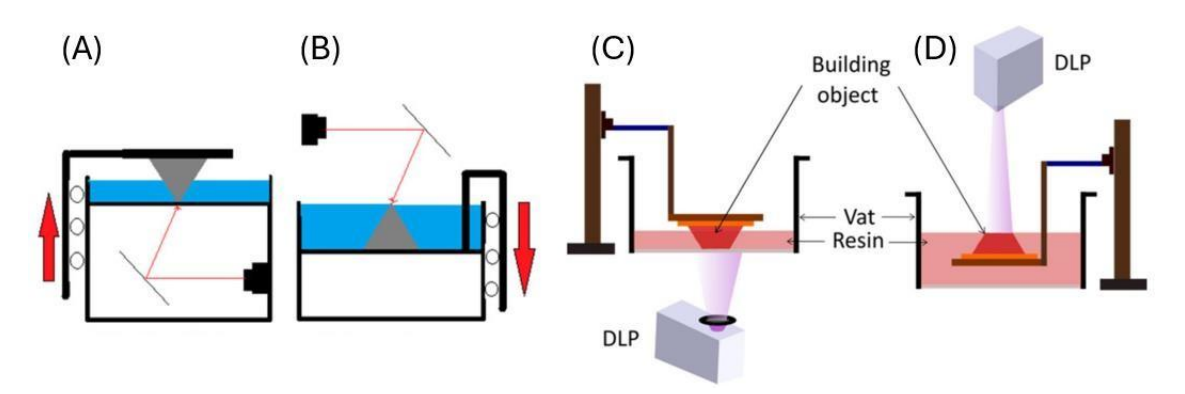


Figure 3.9 scheme of SLA bottom-up (A) and top-down [89]; scheme of DLP bottom-up (D), top-down (D) [90]

3.2.4 Computed axial lithography (CAL)

In Computed Axial Litography (CAL), commonly referred to as Tomographic VAM, the whole volume of the 3D object is generated in a single step, as a result of the superposition of multiple tomographic 2D projections, from different angles, onto a rotating resin vat. These 2D images (or "sinograms") are obtained by acquiring snapshots of the 3D model from different orientations. An algorithm, called Radom transform, is applied to the sinograms to generate the corresponding 2D light pattern. The superposition of the different 2D light projections produces an inhomogeneous

spatial distribution of light energy withing the volume of photocurable material, indicated as Energy Deposition Distribution Field (EDDF) [91]. An example is illustrated in *Figure 3.10*

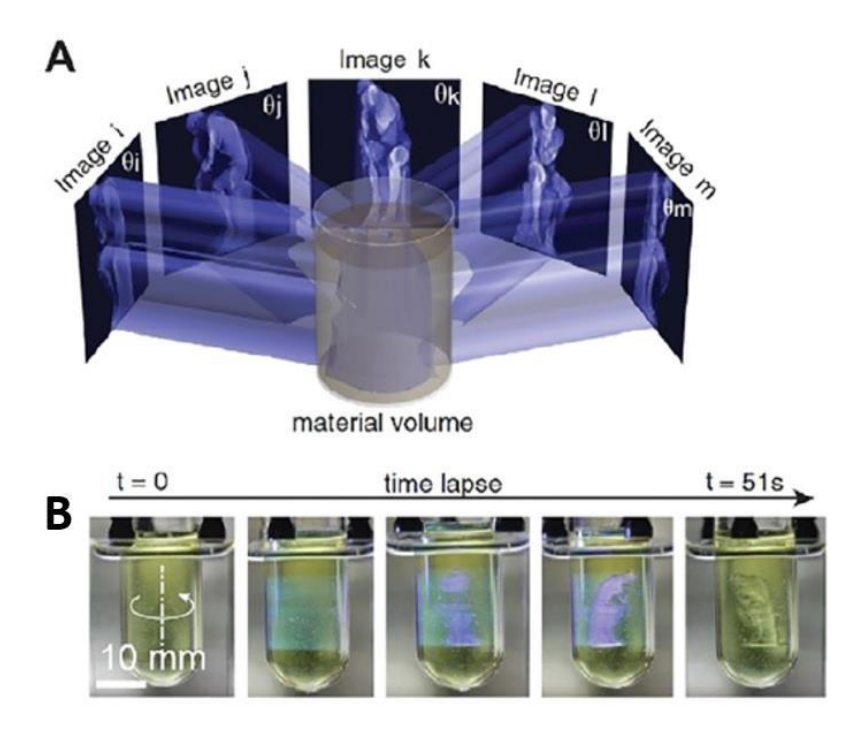


Figure 3.10 A) schematic illustration of the CAL printing process: the material volume is exposed with 2D light patterns from varying orientation B) real time laps of the resin during a printing process.

Vat rotation guarantees that the superposition of light patterns within the resin occurs from multiple angles, ensuring that the EDDF intensity overcomes the material's reaction threshold within the intended voxel, to generate a solid part reproducing CAD geometry [91]. The existence of a reaction threshold for the gelation to take place is crucial. Resins are designed in a way to make the polymer degree of conversion a nonlinear function of the adsorbed light-dose, so that sol-togel transition is induced selectively within resin's voxels where the energy input overcomes a threshold.

Usually, inhibition-mediated, chemical non-linearity is employed. It is achieved by introducing dissolved oxygen or other radicals (both inhibitors of polymerization) in the resin. Upon light absorption, newly formed radicals are immediately deactivated by reacting with inhibiting species, rather than monomers (radical quenching). With increasing adsorbed light dose, inhibitors' amount locally decreases, until it is sufficiently low that polymerization propagation, i.e. polymeric network growth, can proceed. "This type of chemical nonlinearity requires absorption of only a single photon per photoinitiator to operate (linear absorption). Thus, spatial selectivity is determined by the degree of nonlinearity of the polymer conversion vs. absorbed light dose relationship". [82].

3.2.5 Two-photon photopolymerization

A different approach to achieve spatial selectivity in the VAM process is *optical* nonlinearity, in which the generation or absorption of photoinitiator species depends nonlinearly on the local photoexcitation intensity. This requires the (almost) simultaneous absorption of multiple photons by the photo initiator, made possible by the development of ultrafast pulsed lasers. Optical nonlinearity provides greatly enhanced spatial selectivity over the photopolymerization process compared to chemical nonlinearity, used in CAL [82].

Two photon polymerization (2PP) is a direct laser writing (DLW) that relies on two-photon excitation [92]. A high-repetition-rate, sharply focused, pulsed laser beam, is used to write the solid structure into the volume of photosensitive resin. "When a near-infrared (NIR) femtosecond pulsed laser beam is used for the excitation of TPP, the photo initiator absorbs two photons of NIR light and generates radicals to trigger a free radical polymerization reaction" [93]. Founded in 2007, Nanoscribe was the first company to bring 2PP DLW systems to the market. In these systems, beam scanning is performed by translating the sample stage along XYZ, using piezo motors, as shown in Figure 3.11. Among the various VAM approaches, 2PP enables the highest resolution, with the smallest achievable feature below the diffraction limit of light (< 100 nm) [92]. Thanks to its ultra-high resolution, 2PP enables the fabrication of 3D scaffolds with subcellular-scale patterns capable of directing cell morphology. The main limitation of 2PP is its ultra-low volume generation rate (around 1–20 mm³ h⁻¹), and that severely hampers its use for generating constructs above the millimeter- scale [93].

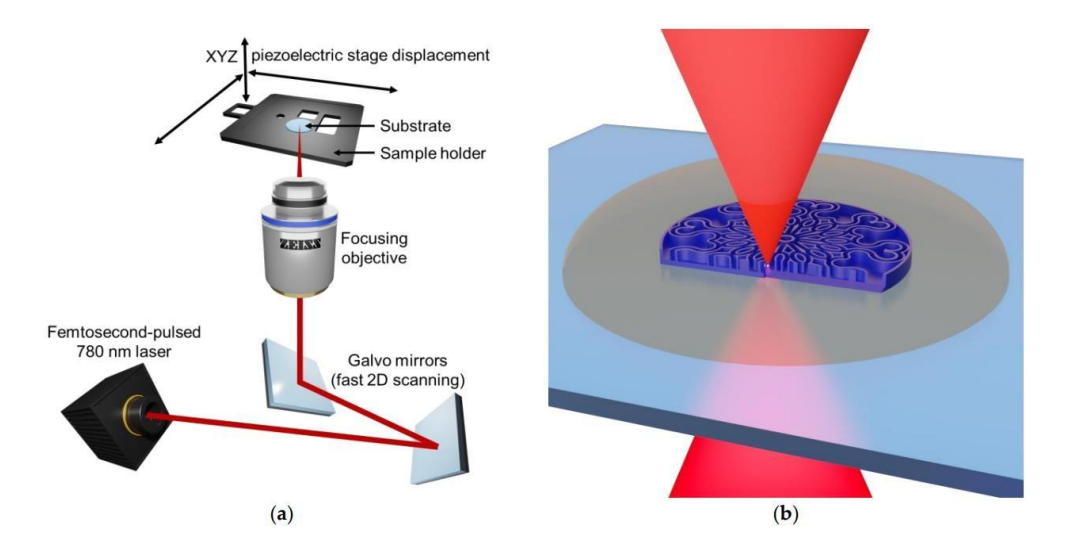


Figure 3.11 Illustration of two-photon polymerization (a) A femtosecond-pulsed laser beam is scanned in two dimensions using a high-speed galvo mirror system and then focused into the sample through a microscope objective. The sample stage can additionally be moved along the X, Y, and Z axes using a piezoelectric system. (b) By scanning the laser focal point, the desired structure is fabricated within the liquid resin voxel by voxel. [92]

3.3 Xolography

Xolography is the latest of volumetric 3D printing technologies, developed by XOLO (GmbH, Berlin, Germany). It enables the fabrication of entire objects within a photosensitive resin in a single step, making use of two intersecting light beams of different wavelengths to achieve spatiotemporally controlled solidification of localized regions (see *Figure 3.12*). A comprehensive description of the process is provided by Regehly et al. [94]. The core of the XOLO technology relies on the dual-color photopolymerization (DCP) process, proposed by Swainson [95]. It is mediated by a double-colour photoinitiator (DCPI), which combines efficient photoswitching and photoinitiating properties.

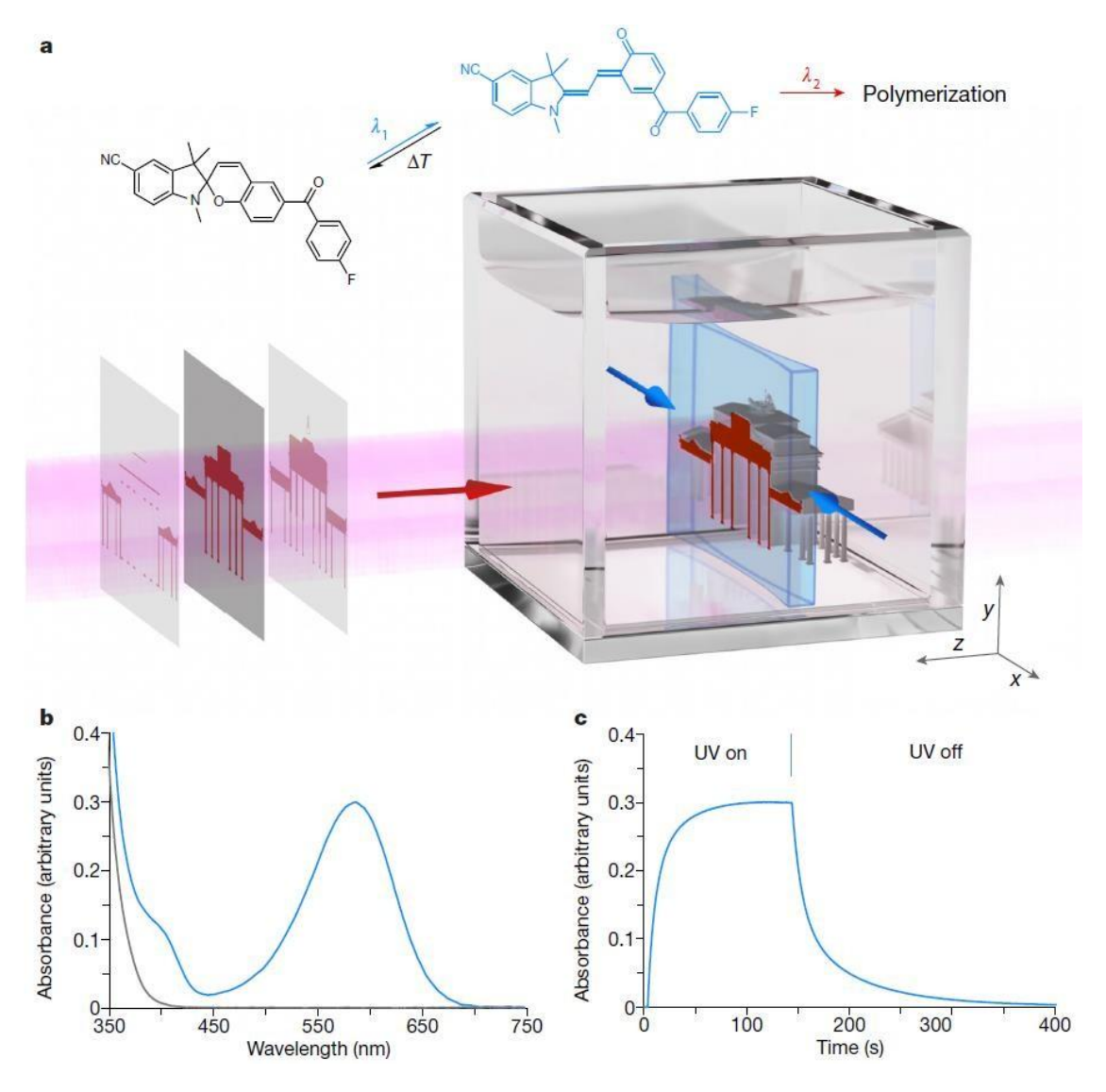


Figure 3.12 Xolography 3D printing (XOLO) technology. (A) Illustration of the printing setup, with a focus on the double-color activation mechanisms of the DCPI. (B) Absorbance spectrum of DCPI in the dark (grey curve) and upon 375 nm UV irradiation (blue curve). (C) Photoswitching kinetics recorded at 585 nm, showing the formation of the

The DCPI molecule is composed of two parts: a benzophenone type II photoinitiator motif linked with a spiropyran group. The spiropyran is a photochrome (t-type) photoswitch, that, when absorbs light at wavelength below 400 nm (λ_1), undergoes photoisomerization, i.e. light-induced conformational change, into merocyanine [95], [96]. As a consequence, the entire DPCI molecule changes its conformation, exposing the photoinitiator motif (DCPI "active" or "latent" form), which was masked in the initial configuration of the molecule ("dormant" form). In this active form, absorption of the second wavelength in the visible range (λ_2 , 450-700 nm) induces the electronic transition that activates the type II photoinitiator moiety, which initiates radical polymerization, in combination with the co-initiator. The two states of the DPCI are, indeed, characterized by different absorption spectra, as shown in *Figure 3.12 B*. DCPI in its spiropyran state only absorbs below 400 nm (UV range), while being completely transparent in the visible range (gray curve). Instead, DCPI latent form (merocyanine state) shows a broad absorption band, from 450 to 700 nm (blue curve). Photoisomerization is reversible, and the latent photo-isomer (merocyanine) thermally reverses back to the initial dormant spiropyran form, with a characteristic half-lifetime (see *Figure 3.12 C*).

XOLO technology merges DCP chemistry with a cartesian projection light setup. in *Figure 3.12* A a schematic of the printing process is provided. The photosensitive resin is contained within a transparent cuvette, where the object fabrication takes place. A linear stage continuously moves the cuvette in the z-direction, towards a thin UV light sheet (λ_1), lying in the x-y plane, while a perpendicularly arranged visible light projector focuses sectional images of the 3D objects onto the sheet. To do so, the 3D model is divided into slices along the zaxis, and each slice is converted into a visible-light pattern, which is projected onto the resin volume to selectively polymerize the target region of the UV-irradiated layer. Resin solidification (curing) only occurs at the intersection of the two light beams, since only the DCPI molecules within the resin layer irradiated by the light sheet (λ_1) can absorb in the visible range, and therefore visible light (λ_2) can initiate polymerization exciting the active DPCI molecule. By synchronizing the sequential display of these slice projections (i.e. slice video) with the light sheet scanning of the resin, the object is continuously fabricated.

To generate these slice videos, a digital light projector of ultrahigh definition is utilized, whose output spectrum is restricted to the absorption bands of the transient merocyanine form DCPI. Looking at *Figure 3.12 A*, the resin filled cuvette is translated away from the projector, ensuring that visible light only interacts with transparent, unpolymerized areas resin, and never passes through previously polymerized regions, which would cause light refraction and scattering.

The absorption spectrum of merocyanine also comprises the UV range, meaning that UV light can initiate the photopolymerization, creating an unwanted competing initiation channel. The light sheet approach has been designed in a way that each voxel of material is hit by UV only once. Also, the irradiance of the visible light projector (215 mW/cm²) is more than one order of magnitude higher than the UV light sheet irradiance, thus favoring the DCP pathway over the single-wavelength initiation route [94].

UV light is exponentially attenuated with increasing penetration depth, due to absorption of DCPI, according to the Beer–Lambert–Bouguer law. Inhomogeneous excitation along the x-direction would lead to uneven polymerization. To compensate for this effect, the light sheet is generated by merging two "half-sheets" that irradiate the resin volume from opposite sides. On each side, a 375-nm Gaussian beam, emitted by a diode laser, is directed onto a rotating mirror, converted into a diverging line, and subsequently collimated and focused to form the light sheet [94].

Free-standing geometries can be realized without the need for supporting structures since it is a self-supported printing technique. Indeed, the volume of the printed object is retained by the viscous surrounding un-cured photo-resin that prevents the solidified part from sinking.

Compared to state-of-the-art volumetric printing methods, Xolography has a resolution about ten times higher than computed axial lithography (300 μ m), a volume generation rate up to five orders of magnitude higher than two-photon photopolymerization (few mm³/h). In a very short time, typically a couple of minutes, complex-shaped macroscopic objects can be manufactured. The smallest size of both positive and negative features is reported to be 20 μ m and 100 μ m, respectively. Examples of printed objects with high resolution features are reported in *Figure 3.13*.

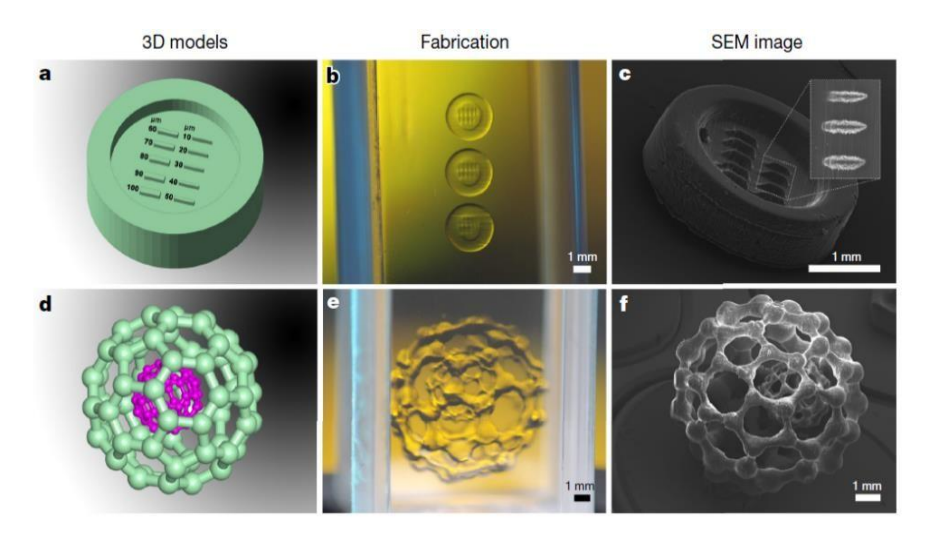


Figure 3.13 CAD models (a, d), printed objects inside the cuvette (b, e) and SEM characterization of post-processed objects (c, f)

On the other hand, this technology presents some drawbacks, mainly related to the strict requirements of high optical transparency and viscoelastic properties of the resins, together with the limited maximum dimension of the printable objects. Related to optical properties, below it is reported a detailed explanation. Mechanical properties (in particular viscosity) should be high enough to maintain the solid structure in position without floating in the uncured resin during printing but, on the other hand, it cannot be too high to prevent sample removal and cleaning. At last, finally, the size of the printable objects is limited, as homogeneous UV irradiation must be ensured throughout each layer, thereby restricting the allowable optical path length. At the present stage, the maximum printable dimension for objects is in the order of few cubic centimeters.

Resin photopolymerization within the intended volume is triggered only if the incident UV light energy density (E) overcomes the resin-specific activation threshold. It is possible to tune the energy input (E) by playing with two adjustable printing parameters: the UV light power density (I) and the printing speed (v) [96]. These three parameters are linked by Equation 3.1

$$E = \frac{3 \cdot I}{v}$$

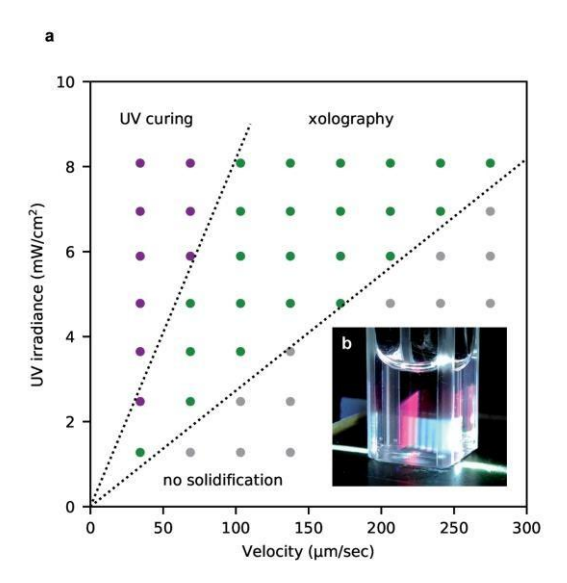
- <u>UV light power density (I)</u> determines the amount of DCPI activated within the irradiated layer. It is directly proportional to the energy input (E)
- <u>Printing speed</u> (rate at which the cuvette is moved) defines the residence time of each virtual resin layer within the intersection volume of the two orthogonal light beams. It needs to be tuned with the characteristic speed of thermal decay of the activated DCPI merocyanine form [94], [96].

The effect of these two printing parameters on the result of the printing process must be investigated and optimized for every new photo-resin composition, to identify the so-called "printing window". To this end, a calibration procedure has been established: The same geometry is printed several times using different combinations of printing parameters. An optical readout detected whether the (I,v) or (E,v) combination led to no curing, dissolving parts, correctly printed objects, overcured parts or UV-initiated polymerization. In this way, a matrix of results is generated, comprising five regions [94], [96].

- No curing: combinations of too low I and/or too high v, for which the energy input falls below the activation threshold, meaning that concentration of activated photoinitiator molecules is too low to provide sufficient crosslinking between monomers, i.e. any gelation occurs.

- <u>Dissolving</u>: (I, v) combinations that result in partial and insufficient crosslinking, i.e. "dissolved" parts.
- Overcuring: combinations of low print speed and/or high UV intensity which cause undesired crosslinking over the edges of the intended geometry, so that the CAD model is no longer resembled
- <u>UV hardening</u>: the UV energy dose is so high that the competing single-wavelength activation channels of the photo-initiator overcomes the two-colour mechanism, leading to unspecific UVlight-induced curing of the entire cross-section of the cuvette is polymerized due to the UV scanning producing sheet-like structures.
- <u>Printing</u>: it is the window of suitable parameter combinations to achieve geometries with well-defined features, close to the CAD model. In this case, solidification only occurs following the dual-colour photopolymerization on which xolography is based.

The last region is the desired parameter space for xolography (or printing window), limited by a minimum light dose to achieve the curing of the whole object and by a maximum value above which undesired solidification verify. In its simpler form, the calibration matrix can be limited to three main regions: UV curing, printing region ("xolography") and no solidification, as shown in *Figure 3.14*.



- Figure 3.14 a. Results of the calibration procedure: array of tested irradiance/velocity combinations, divided into three parameters regions: UV curing, xolography and no solidification. Each dot represents a classified result. b, Photograph of the printing process in a 1-cm cuvette [94]

While in layer-by-layer VP technologies (SLA, DLP), the light exposure of one thin slice at a time allows to compensate low curing depths and light-scattering-induced artifacts, in volumetric AM photo-resin's transparency becomes of paramount importance. Despite the challenge, Sanger et al. demonstrated the possibility to utilize XOLO technology to print composite photoresins filled with ultra-fine and highly dispersed 5 nm zirconia nanoparticles. Filler loadings up to 70% w/w could be printed with Xolography since monocrystals of pure zirconia are characterized by high transparency in the range of 260 - 700 nm [97].

Stoecker et al. have recently reported the first-ever application of Xolography for bioprinting purposes, demonstrating the cytocompatibility of the printing process [96]. Aggregates of human mesenchymal stromal cells (hMSCs) were incorporated into a sterile GelMA-based photoresin (10% w/v GelMA). Cellladen constructs, resembling the CAD geometry, were successfully 3D printed using XOLO technology, and a good percentage of viable cells was observed after one and five days of culture. Despite the high cytocompatibility, bare GelMA photoresins exhibited poor printing performance, with very narrow printing windows and low resolution of the printed structures. The study demonstrated that the addition of low molecular-weight (Mw) PEGDA significantly improved the printability of the hybrid resin, by extending the printing window and enhancing the resolution. This arises from the fact that the presence of PEGDA increases the concentration of double bonds, thereby accelerating the cross-linking process. On the other hand, the introduction of PEGDA decreases the cytocompatibility of the photoresins, drastically reducing cell viability [96].

4. Materials and methods

4.1 GelMA synthesis

Gelatin methacrylation was performed following the protocol described by Loessner et al., which has proved to be a reliable and user-friendly method to synthetize GelMA having reproducible biochemical properties. The introduced photoactive functionalities are a mixture of methacrylamide and methacrylate groups, with the latter accounting for the majority (>90%) [40]. Gelatin from porcine skin, gel strength 300, type A (Sigma-Aldrich) and methacrylic anhydride (Sigma-Aldrich) were used.

Based on the previously established protocol, with minor modifications, the steps for GelMA synthesis are the following:

- 1. Gelatin is dissolved in ultra-pure water (UPW) to a final concentration of 10% w/v in a glass beaker with a magnetic stir bar. The beaker is placed in a water bath at 50°C while gently stirring for 30-60 minutes until gelatin is fully dissolved, resulting in a clear solution.
- 2. Inside a chemical safety fume hood, methacrylic anhydride (MAA) is slowly added with the aid of a glass pipette at a ratio 6:10 with respect to gelatin while stirring vigorously. The solution is then kept stirring for 3-4 h at 50°C to allow the reaction gelatin methacrylation to occur, until a viscous and homogeneously opaque solution is achieved. Reaction time, temperature and mass ratio of MAA to gelatin determine the degree of GelMA functionalization (DoF). In these conditions the DoF has been reported to be around 79% [40].
- 3. To remove the unreacted MAA the solution is transferred into 50-mL tubes and centrifugated at 3500 rpm for 3 minutes at 40°C. The clear supernatant containing GelMA is poured into a glass beaker and diluted with two volumes of preheated (40 °C) UPW, while the opaque viscous pellet of MAA is discarded.
- 4. Using a 12-kDa Molecular Weight Cut Off (MWCO) dialysis membrane, the GelMA solution is dialyzed at 40 °C against a large volume of Ultra Pure Water (UPW) for 7 days. Methacrylic anhydride and acid byproducts are cytotoxic, so any trace of these contaminants must be removed if the material is intended to be used to encapsulate cells. The water is changed every day. Dialysis is completed when the GelMA solution appears clear and the odor of residuals is no longer noticeable.

- 5. Under magnetic stirring, the pH of the purified GelMA solution is adjusted to 7.4 by adding dropwise a solution of NaHCO₃ (1M) until the intended pH is reached.
- Finally, GelMA solution is partitioned into 50 mL tubes, stored at −20 °C overnight to allow complete freezing. It is then transferred into a freeze dryer and lyophilized for 7 days until fully dehydrated.

GelMA is stored at -20 °C until use.

4.2 Optimization of IOPs self-assembly

The first step of the work was the investigation of how the magnetic microstructure can be tuned and spatially controlled inside the liquid photo-resin before the printing step. To this end, the effect of three main regulating factors on the final self-assembled microstructure was studied:

- Magnetic nanoparticles concentration
- Viscosity of the host matrix
- Duration of the exposure to the magnetic field

Polyethilenglycole (PEG) - functionalized Iron oxide (II,III), magnetic nanoparticles dispersion (30 nm avg. part. size (TEM), 1 mg/mL Fe in H_2O) from Sigma-Aldrich was employed as magnetic building blocks. Three different concentrations of IOPs were tested: 0.005% w/v, 0.01% w/v and 0.02% w/v.

For a fixed working temperature, increasing concentration of GelMA leads to a marked enhancement of the solution's viscosity [98]. To study the effect of the viscosity of the host matrix on the self-assembly process, two different hydrogel precursor solutions were used, having different GelMA concentrations.

- A blend of GelMA 5% w/v and PEGDA (Mw=575 g/molto) 10% w/v in UPW
- A blend of GelMA 8% w/v and PEGDA (Mw=575 g/molto) 10% w/v in UPW

In both cases, 0.1% w/v Lithium phenyl-2,4,6-trimethylbenzoylphosphinate (LAP) (Sigma-Aldrich, USA) was used as photoinitiator.

Polydimethylsiloxane (PDMS) molds with three cavities (6 mm x 6 mm x 4 mm) were created to cast the MNPs-laden hydrogel solution. The negative master was designed using *Solidworks* 2024 (Dassault Systèmes) and 3D printed using LuxaPrint Ortho Plus TRA resin (DMG, Germania) with an Asiga MAX 3D printer (Asiga, Australia). Polydimetilsiloxane (PDMS, SylgardTM 184

Silicone Elastomer Kit, Dow Corning, USA). The mixture was poured inside the negative master, degassed for 20 min using a CRVpro vacuum pump (Trivac) then cured in oven (Carbolite PF Fan Convection Oven) at 65°C for 3 hours. The cured PDMS part was then extracted from the master and washed in acetone. In *Figure 4.1* the negative master and the PDMS molds are shown.



Figure 4.1 Master and PDMS mold

To create the magnetic field, a total of eight neodymium magnets (4 cm x 2 cm x 0.5 cm each), purchased by Supermagnete (Webcraft, GmbH, Germany, strength approx. 14 kg), were used. A customized holder was designed and manufactured using Tough 1500 Resin V2 (Formlabs, Somerville, MA, USA) with a Formlabs Form 4 printer (Formlabs, Somerville, MA, USA). The holder was conceived to keep the pair of magnetic blocks (four per side) 4 cm apart from each other and to locate the PDMS mold in the exact center between them, to achieve a spatial field distribution as uniform as possible inside the volume where the particles-laden solution will be poured. A drawing of the holder design is provided in *Figure 4.2*, while a picture of the assembled system (holder, magnets, PDMS mold) is presented in *Figure 4.3* (right side).

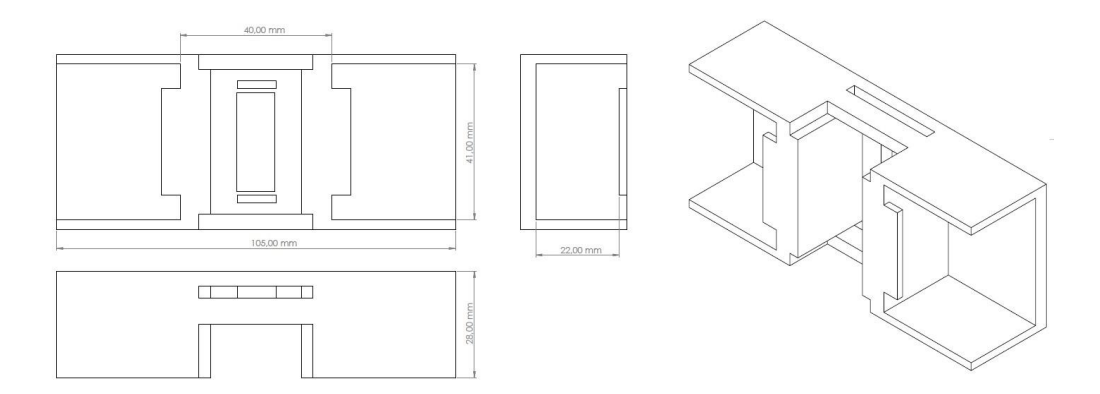


Figure 4.2 Design of the holder intended to locate the magnets and the hydrogel's mold in a way that the mold is positioned in the exact center of the magnetic field

By placing the magnets at a distance of 4 cm from each other, the magnetic field's intensity was 162 mT in the center and 170 mT at the two sides, closer to the magnets, 3mm apart from the center. The magnetic field intensity was measured with a PCE-MFM 3500 AC/DC magnetic field meter.

The viscosity of a GelMA solution is strongly influenced by the working temperature. For this reason, environmental changes of temperature would alter the viscosity of the hydrogel solution, affecting the kinetic of the self-assembly process in an uncontrolled manner. To make the experiments more reproducible, the temperature of the hydrogel solution was kept at $\sim 37^{\circ}$ C during the particles' alignment. To this end, the whole assembled system (comprising holder, magnets and PDMS mold) was partially immersed in a $\sim 38^{\circ}$ C water bath, created by placing a glass petri dish filled with water on a hotplate (DHP 15, Labo Tech, Germany) at

39°C, as shown in *Figure 4.3 (left side)*. A higher temperature was set on the hotplate to account for heat loss. The petri dish was then covered with aluminum to thermally isolate the system. Only once water's temperature reached 38°C, 80 □L of particles laden hydrogel solution was poured inside each wall of the hydrogel's mold.

N.B. A magnetic stirrer cannot be used as a heating source due to the magnetic nature of the plate that would interact with the magnets and interfere with the experiment.



Figure 4.3 Setup to produce anisotropic magnetic hydrogel samples. On the left side the magnets and hydrogel's mold assembled on the custom-made holder. On the right side the assembled system placed in the water bath during particles-self assembly (magnets are covered by parafilm to protect them from water and prevent rust formation)

After a given duration of magnetic exposure (5min, 10 min, 20 min or 30 min) the assembled system (holder, magnets and mold) was moved into a UV curing chamber (Nailstar NS-01-UK/EU, 220–240 V, 36 W) for 2 min to photopolymerize the hydrogel matrix and fix the particles arrangement. The external magnetic field was continuously applied during the entire gelation process, so that the magnetic particles could maintain the alignment. The procedure of casting, waiting and UV-curing was repeated varying the duration of the magnetic exposure before curing. In this way, it was possible to simulate the dynamics of the self-assembly process. Thanks to the three-well mold, it was possible to realize a triplicate of patterned samples for each time point. The magnetic microstructures inside the solid hydrogel samples were observed with a Leica DMi8

inverted microscope (Leica Microsystems GmbH, Germania) in brightfield mode, using LAS X (Leica Application Suite X) software. For each sample, eight images were acquired in different locations of the sample, moving on the XY plane and along the z axes.

Fiji (Fiji Is Just ImageJ, version 2.9.0) software was used to process the images to quantify the dimensions of particle aggregates. Contrast and brightness of the grayscale pictures were adjusted to enhance the separation between the intensity levels of the magnetic chains and the background. The first attempted approach was the binarization of the images into black and white, followed by the use of the built-in 'Analyze Particles' function to automatically detect and measure the dimension of the aggregates. However, the results were not satisfactory, since the magnetic chains were very thin and discontinuous in some regions, causing the software to incorrectly identify them as separate aggregates. To overcome this issue, the chains' length was measured manually by drawing line segments and recording their length. This manual approach allowed to discriminate between in-focus chains and out-of-focus structures located at different depths, which appeared blurred and with lower contrast against the background, thus being difficult to properly binarize. Due to the relatively limited image quality, automatic detection would misclassify these structures, whereas manual measurement ensured a more accurate evaluation of the actual chain length. An example is shown in Figure 4.4.

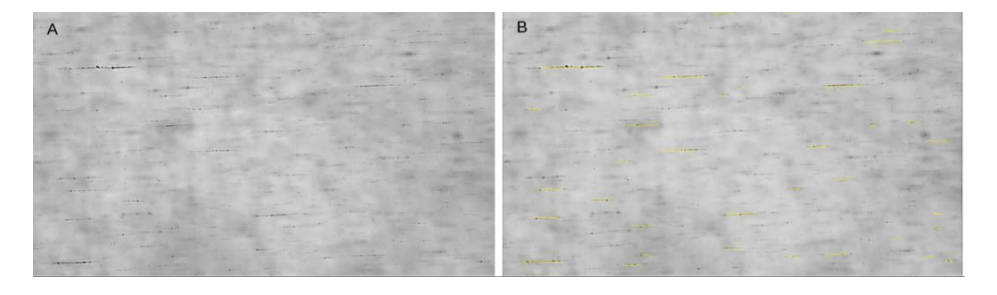


Figure 4.4 (A) Brightfield images of the inside structure of the magnetically patterned hydrogel sample, captured by a Leica DMi8 inverted microscope (B) yellow segments manually defined to identify magnetic aggregates and measure their length.

For each patterned hydrogel sample, the average chain length was calculated from eight acquired images. These values were then averaged across the triplicates realized for each time point, and the corresponding standard deviation was determined. The data was plotted in Excel to obtain a graph of chain length versus time. The analysis was repeated by varying the particle concentration (0.005%, 0.01%, 0.02% w/v) and the GelMA content in the hydrogel formulation (5% w/v, 8% w/v), i.e., the viscosity of the host matrix.

4.3 Adaptation of the self-assembly approach to Xolography

4.3.1 XOLO printers

Two different versions of Xolography-based 3d printer were used and compared: Xube and Xube². In *Figure 4.5* the Xube version is reported.

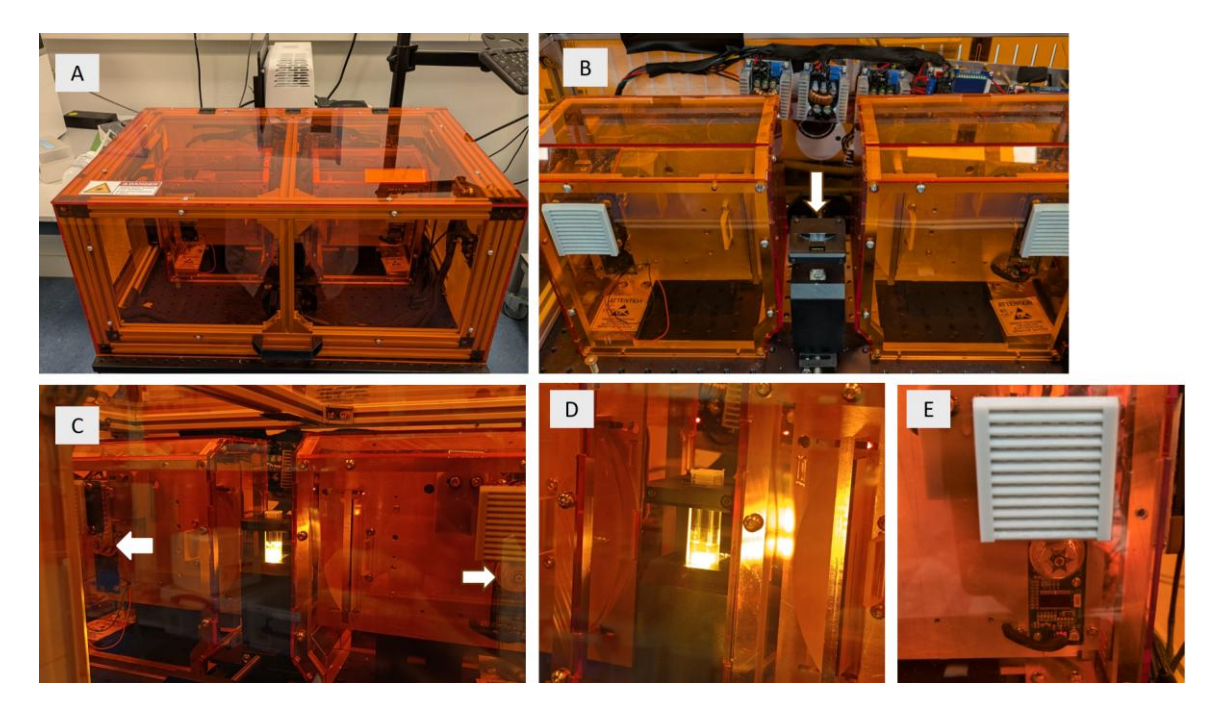


Figure 4.5 Pictures of the Xube printer (A) closed (B) open. The white arrow indicates the cuvette-holder (C) Picture of a printing process. The white arrows indicate the rotating mirrors used to generate the two UV semi-light sheets.

(D) zoom on the irradiated cuvette (D) zoom on the rotating mirror device

Xube² is the ultimate version of XOLO printers. Compared to Xube, Xube² reaches significantly higher resolution. Halogen lamp-based projector is replaced by a fully adjustable 3 channel LED projector, which enables a more controlled polymerization, with a resolution down to 5 mm. The light sheet module allows you to switch from 375 nm laser sheet to 405 nm.



*Figure 4.6 Pictures of the Xube*² *printer.*

A fundamental improvement of Xube² is the presence of a high-frequency shifting microlens array (MLA) system that allows to enhance the homogeneity of the activating light sheet. The MLA splits the incoming UV beam into multiple micro-beams and refocuses them. Due to the rapid vibration of the MLA system, the direction of the re-focused micro-beams is continuously varied, enabling a dynamic homogenization of the incident UV light sheet

4.3.2 Photoresin preparation

Pristine hydrogel photoresin composition:

- GelMA 5% w/v
- PEGDA (Mw=575) 10% v/v
- BisTris 0.8 M
- DCPI (5004 for Xube or 6001 for Xube²) 0.015% w/v

Increasing amount of commercially available magnetic nanoparticles were added to the bare hydrogel matrix to find the maximum concentration of magnetic nanoparticles that it is possible to introduce inside a photoresin without compromise the printability of the composite material: 0.005%, 0.01%, 0.02% and 0.03% w/v.

Stock solutions:

- <u>BisTris (2M)</u>: 20.92 g of BIS-TRIS (B4429, Sigma-Aldrich, USA) were added to ~ 30 mL UPW inside a beker and dissolved under magnetic stirring at room temperature for around 20 minutes, until a homogeneous solution is obtained. Then, the pH (basic) was adjusted by adding dropwise a solution of hydrochloric acid (HCl) 1M while stirring, until pH=7.4 was reached. UPW was added to reach a final volume of 50mL. Finally, the stock solution was transferred into a 50mL falcon tube and stored in the fridge.
- GelMA (25% w/v): lyophilized GelMA was soaked in pre-heted UPW. Heating cycles in a 50 °C water bath were alternated with vortex mixing until GelMA fully dissolved. It was stored in the fridge and melted in a 40°C water bath before use

Photoresin preparation steps (for a10 mL volume)

1. 1.5 mg of DCPI (DCPI5001 for Xube and DCPI6001 for Xube²) were dissolved in 1mL of UPW to obtain a DCPI stock solution 10x more concentrated than the desired final

concentration in the photoresin. The solution was prepared in a 2mL Eppendorf and sonicated for 5 min at 25°C. Aluminum foil was used to cover the Eppendorf to shield the photo-initiator solution from light.

- N.B. DCPI solutions should not be stored longer than 24h, as the DCPI reactivity may degrade. Therefore, they were prepared prior to each use.
- 2. 1 mL of melted GelMA stock solution (25% w/v) at 40°C was mixed with 4 mL of BisTris stock solution (2M) inside a glass beker and magnetically stirred at 50°C for 10 minutes (250 rpm)
- 3. 1 mL of PEGDA was added dropwise and everything was stirred for 10 minutes until a homogeneous solution was obtained
- 4. 1 mL of DCPI stock solution (10x) was added after covering the beker with aluminum foil. Everything was stirred for 10 minutes
- 5. UPW and IOPs stock solution (1 mg/mL) were added to fill the remaining 30% v/v of the total volume (10 mL) at the correct ratio to achieve the desired IOPs concentration. E.g. to obtain [IOPs] = 0.01% w/v, 1mL of IOPs stock and 2 mL of UPW were used.
 N.B. IOPs stock solution was always sonicated for 3 min at RT before use, to dissolve any aggregate that could be formed after long periods of storage.
- 6. The IOPs-laden hydrogel solution was vortexed until a homogeneous dispersion of particles was achieved. N.B. Magnetic stirring cannot be applied because magnetic nanoparticles would attach to the magnetic bar, thus reducing their amount in the liquid material.

Cuvette preparation:

- 7. 0.55 mL of resin was used to fill each XOLO cuvette, then centrifugated for 2 minutes at 800 rpm at RT to remove bubbles and deposit at the bottom the material stuck on the cuvette wall.
- 8. To promote quick GelMA gelation, the cuvettes were immersed in ice for 10 minutes.
- 9. The external surface of the cuvette was wiped with tissue paper before placing it inside the 3D printer, to remove traces of water and dust which could interfere with the printing process.

For each photoresin composition (0%, 0.005%, 0.01%, 0.02%, 0.03% w/v IOPs), a full factorial screening of printing parameters was performed. For Xube, the parameters varied were printing speed (v) and UV light power density (I), while for Xube² it is possible to set the printing speed and UV light energy density (E).

The aim was to find combinations of printing parameters allowing for the correct printing of the object in the minor time possible. For this reason, only the higher speeds enabling the printing were explored. In *Figure 4.7* the model of the test object is shown.

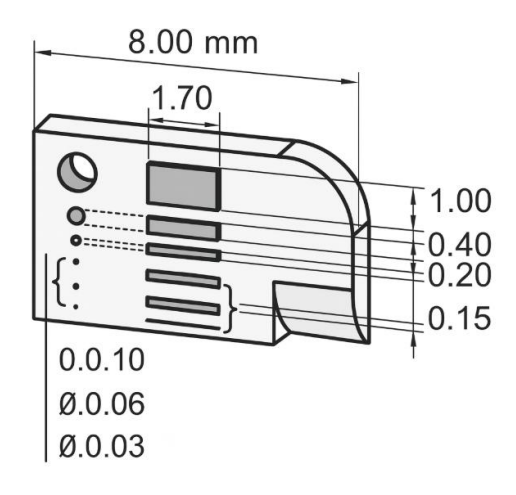


Figure 4.7 Design of the geometry of the printed object [96]

4.3.3 Stabilization of the anisotropic pattern in XOLO cuvette

To integrate the magnetic alignment of nanoparticles within photo-curable hydrogel matrices with XOLO technology, the reversible thermal gelation of GelMA-containing solutions was leveraged to stabilize the particles aligned microstructures within the photo-resin volume contained inside the XOLO cuvette.

To this end, a new holder was designed and manufactured. This holder differs from the one used for the kinetics analysis only in the design of the part to hold the cuvette, as the magnetic blocks and inter-magnets distance were the same. A drawing of the holder for the cuvette is reported in *Figure 4.8*, while a picture of the assembled system (holder, magnets, cuvette) is provided in *Figure 4.9*.

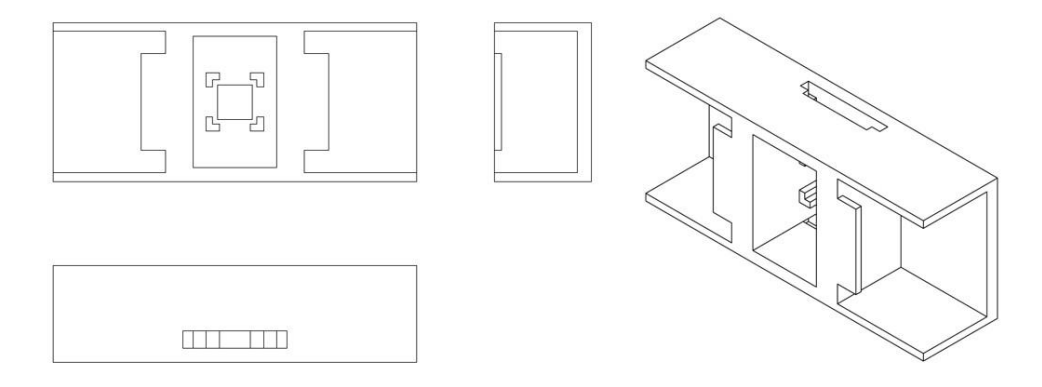


Figure 4.8 Drawing of the holder used to keep the cuvette in between the magnets to promote the self-assembly of magnetic nanoparticles inside the volume of photoresin

The concentration of IOPs used (0.01 % w/v) was the highest compatible with Xolographic 3D printing, as determined in previous experiments. The magnetic resin was poured inside the XOLO cuvette, that was then placed in the holder located inside the warm water bath at 39°C, as shown in *Figure 4.9*. After 20 minutes of exposure to the magnetic field, all the system (holder, cuvette and magnets) was entirely immersed in ice for 10 minutes to induce thermal gelation (see *Figure 4.9*).



Figure 4.9 Left: picture of the assembled system: holder, magnets and cuvette; Center: Assembled setup placed in the warm water bath during the IOPs self-assembly; Right: Assembled setup immersed in ice to promote thermal gelation of the composite photoresin

The printing process must be performed as soon as possible after GelMA gelation, to prevent resin softening, and losing the embedded aligned configuration of nanoparticles. The Xube² was employed, using a combination of 1.5 mm/min printing speed and 45 mJ/mm² energy density. Parallelepipeds of 3 mm x 3 mm x 2 mm were printed. The inner microstructure of the printed samples was then observed as for the cast samples.

4.4 Cell culture

C2C12 cells (passage 9) were thawed in a 37 °C water bath, then transferred to a 15 mL tube containing 4 mL of pre-warmed growth medium (20% FBS and 1% PenStrep in DMEM High Glucose) and centrifuged at 300G for 5 minutes. The cell pellet was resuspended in 1 mL of fresh growth medium and 1:40 of cells suspension was seeded onto 10 cm Petri dishes filled with 10 mL of growth medium. The medium was replaced every 2 days, and cells were passaged when they reached 70–80% confluency.

At each passage, cells were washed twice with 5mL of Phosphate-Buffered Saline (PBS) and then incubated with 1 mL of Trypsin-EDTA at 37 °C for 1 minute. Trypsin activity was then neutralized

by adding 2 mL of growth medium. An aliquot of this cell suspension was then seeded into new

10 cm Petri dishes in 10 mL of fresh medium. The value of the aliquot of cell suspension seeded

depends on the desired rate of growth. For instance, using a ratio of 1:40 of the total volume of cell

suspension the 70-80% of confluency in a 10cm petri dish is reached after around 4 days. With a

ratio of 1:10 cells reach confluency after around 2 days.

4.4.1 Cell casting – Cytocompatibility analysis

To assess the cytocompatibility of PEG-capped IOPs and PEGDA, two different hydrogels

formulation were prepared to decouple the effect of each component on cells viability and

metabolic activity: one consisting of 5% w/v GelMA (cytocompatible control) with 0.01% w/v

PEG-capped IOPs, the other composed of GelMA 5% combined with PEGDA 10% v/v. In all cases

0.1% LAP was used as photoinitiator to achieve quick photopolymerization with UV light

irradiation.

0.5 mg of GelMA and 1g of LAP were dissolved into 7mL of PBS. The solution was filter-sterilized

with a 0.2 μL syringe filter, while the IOPs stock solution (0.1% w/v) was transferred into a 2mL

Eppendorf and sterilized via 30 minutes of UV irradiation. PEGDA (Mw=575) was filter-sterilized

separately.

Three 2-mL Eppendorf were filled with 0.7 mL of the sterile GelMA/LAP solution. To obtain the

pristine GelMA hydrogel, 0.1 mL of sterile PBS was added to one of the Eppendorf. For the

GelMA/IOPs sample, 0.1 mL of sterile IOP stock solution was added instead of PBS, whereas for

the GelMA/PEGDA sample, 0.1 mL of PEGDA was used. The remaining 0.2 mL volume was

completed with the cell suspension.

C2C12 cells at passage 24 at 80% confluency were washed two times with PBS and incubated

with 1mL of Trypsin-EDTA for 1min at 37°C, then 4mL of fresh growth medium were added to

neutralize Trypsin activity. The cells suspension was transferred into a 15ml tube and centrifugated

for 5 minutes at 300 G. Cell pellet was resuspended in 1 mL of culture medium inside a 2mL

Eppendorf, and cell density was measured using a CountessTM 3 Automated Cell Counter

(Invitrogen, Thermo Fisher Scientific, USA). For the cell counting, a

10 μL aliquot of the cell suspension was mixed with 10 μL of Tripan blue (Sigma Aldrich, USA)

and 10 µL of the mixture was loaded into each of the two counting chambers. The cell suspension

was then centrifugated for 5 min at 300G. The cell pellet was resuspended in sterile PBS to obtain

a cell suspension of $5 \cdot 10^6$ cells/mL,

calculated according to the formula

Number of cells : PBS volume = $5 \cdot 10^6$ cells : 1 mL

59

The desired cell density inside the hydrogel matrices was 10⁶ cells/mL. By adding 0.2 mL of 5 · 10⁶ cells/mL cell suspension into each hydrogel formulation (total volume= 1mL), a dilution of 1:5 was achieved to obtain the desired cell density.

To summarize, the three hydrogel matrices were:

- 1. GelMA: 0.7 mL of GelMA/LAP solution; 0.1 mL PBS; 0.2 mL cell suspension (5x)
- GelMA/IOPs: 0.7 mL of GelMA/LAP solution; 0.1mL IOPs stock solution (0.1 mg/mL);
 0.2 mL cell suspension
- 3. <u>GelMA/PEGDA</u>: 0.7 mL of GelMA/LAP solution; 0.1mL PEGDA; 0.2 mL cell suspension

 $80~\mu L$ of cell-laden hydrogel precursor was poured inside each well of the PDMS molds and photocured through 10 minutes of UV irradiation using a UV chamber (Nailstar, NS-01-UK/EU, 220-240V, 36W). With the help of a sterile spatula, the constructs were moved into a 24-well and cultured in growth medium.

4.4.2 Live/Dead essay

Viability of cells within the hydrogels was assessed at day 1 and day 7 of culture using a Live/Dead assay kit (Invitrogen, Thermo Fisher Scientific, USA). Cells were stained with Calcein-AM (live cells) and propidium iodide (PI) (dead cells). The staining solution was prepared by diluting Calcein-AM 1:1000 (1 μ L/mL) and PI 1:100 (stock 1 mg/mL) in PBS. The cell-laden hydrogels were washed twice with 1 mL of PBS, then incubated with 1 mL of staining solution at 37 °C for 50 min. Samples were then transferred into a μ -Slide 4 Well (Ibidi) and imaged using a Leica TCS SP5 Laser Scanning Confocal Microscope (Leica Microsystems, Germany).

4.4.3 Cell casting – Anisotropic Magnetic Hydrogels

All the devices needed to produce magnetically patterned, cast hydrogels were sterilized before use: UV curing lamp, PDMS molds, holder, magnets, spatula, glass petri dish, heating plate. The sterilization of the molds, holders, spatula and petri dish was carried out by 30 minutes of ethanol washing followed by 2 x 30 minutes of UV light exposure (one per side) inside a biological ML-II cabinet. For the UV chamber, thermometer and hotplate the washing step was replaced with simple ethanol wiping. For the sterile water bath autoclaved UPW was used. A digital thermometer was used to monitor the temperature of the water bath during the whole process to ensure that water temperature remains in the range of 38-39°C.

The same protocol described in Section 4.4.1 was used to embed C2C12 (passage 25) inside the GelMA/IOPs hydrogels. Magnetic nanoparticles were aligned in the presence of cells for 20

minutes before UV-curing, following the same procedure described in Section 4.2, but working sterile in a MLII safety cabinet.

Phase contrast images of cells were acquired at day 1, 3 and 6 with an Invitrogen EVOS M3000 microscope (ThermoFisher, Scientific, USA). Phalloidin/DAPI staining was performed at day 6 to evaluate cells' cytoskeletal organization.

4.4.4 DAPI/Phallodin staining

Constructs were transferred into a μ -Slide 4 Well and washed twice with PBS. Then, they were fixed with 1 mL of 4 % PFA at room temperature (RT) for 30 minutes, under shaking. After being washed two times with PBS for 5 minutes, samples were permeabilized with 0.5 % Triton X-100 (SigmaAldrich, Germany) at RT for 30 minutes under shaking. Permeabilized constructs were washed 3 times for 5 minutes under shaking. Actin filaments were stained with Phalloidin 550 (1:200 dilution) for 1h under shaking. Samples were then washed with PBS and cells' DNA was stained with DAPI (1:1000) for 15 min. Constructs were imaged with Confocal Laser Microscopy (TCS SP5, Leica Microsystems, Germany) using LAS X Office software.

Quantitative analysis of myotube orientation was performed with Fiji (ImageJ). Fluorescent images of actin-stained samples were processed with the OrientationJ plugin [101]

5. Results and discussion

5.1 Kinetics of IOPs self-assembly

As mentioned in material and method section, the magnetic field-driven self-assembly of 30 nm sized iron oxide nanoparticles was performed in four different conditions, to evaluate the effect of both nanoparticles concentration and host matrix viscosity on the self-assembly behavior:

Brightfield images of the inner microstructure of patterned hydrogel samples at different time points (5 min, 10 min, 20 min, 30 min) are shown in *Figure 5.1*, providing a qualitative representation of the self-assembly progression. Any alignment was observed with 0.005% w/v IOPs and images are not shown.

5 min 10 min 20 min 30 min

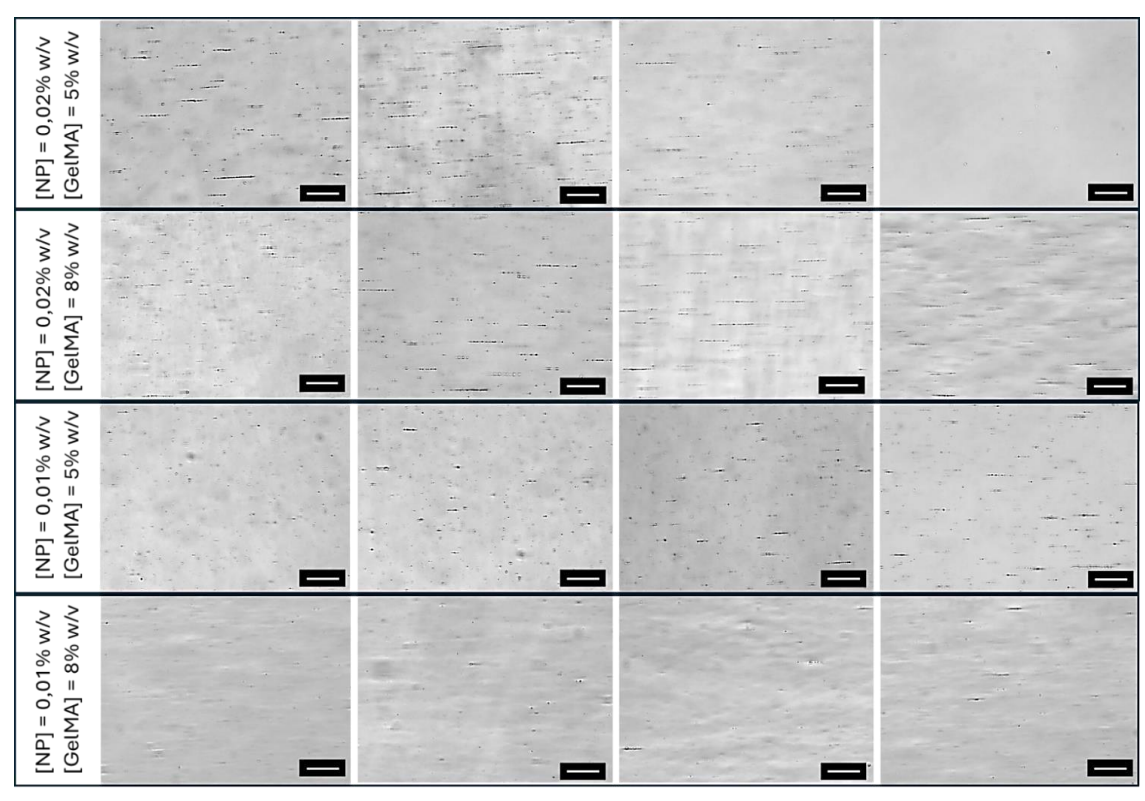


Figure 5.1 Self-assembly progression for four different combinations of NPs concentration and GelMA concentration within the hydrogel precursor. Each line corresponds to a ([NPs], [GelMA]) combination, specified on the left. Each column represents a different time-point. Scalebar 50 \(\text{ \text{Im}} \)

The profile of self-assembly for each condition was described by a graph where the average chains' length is plotted against time. For each time point, the average chain length was calculated from

triplicate samples, and the corresponding standard deviation is reported. In *Figure 5.2* the four profiles are reported

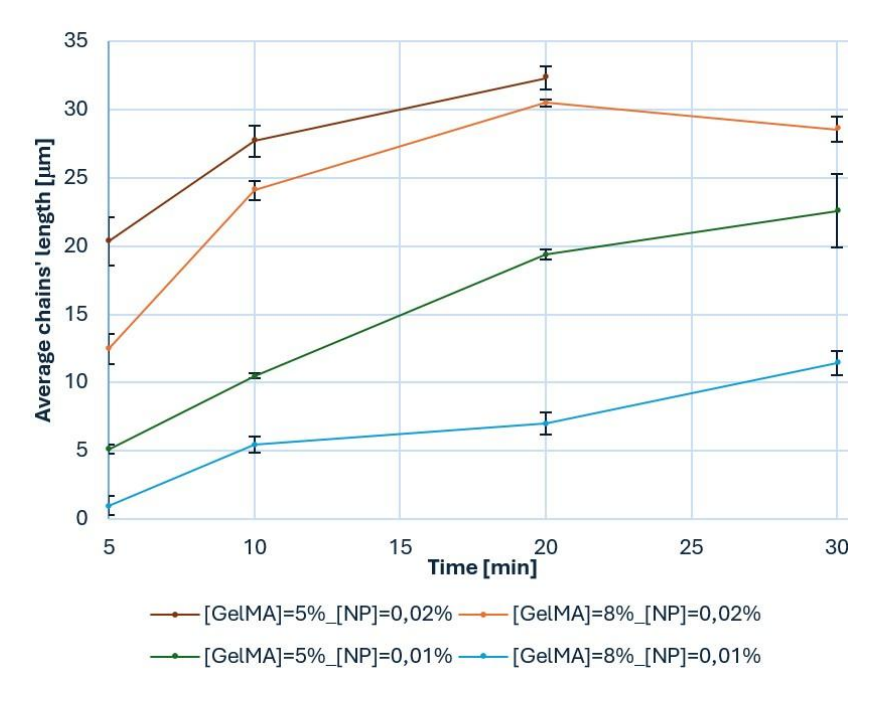


Figure 5.2 Chains' average length versus time for the four tested conditions: [NP]=0.02% w/v & [GelMA]=5% w/v (brown); [NP]=0.02% w/v & [GelMA]=8% w/v (orange); [NP]=0.01% w/v & [GelMA]=5% w/v (green); [NP]=0.02% w/v & [GelMA]=5% w/v (blue);

The variation of the amount of GelMA in the hydrogel precursor leads to a change of the solution's viscosity [98]. An increase in the viscosity of the medium in which the particles are dispersed represents an obstacle to their field-driven self-assembly. Greater increase in length within less viscous medium was already reported by Kim et al. [69]. Matrix viscosity affects particles arrangement into chain-like structures aligned along magnetic field lines in two ways:

- In a low-viscosity environment, particles can translate and rotate more freely, which facilitates the alignment of their magnetic moment along the magnetic field direction (first foremost step of the self-assembly) [63].
- The acting force between MNPs, driving their movement and assembly into chain-like structures along the magnetic field lines, is composed by two main contributions: the inter-dipoles magnetic interaction force and the friction force. The particles movement within a liquid medium is hampered by the resistance from the host matrix (friction force), which is proportional to the equivalent viscosity [99].

As a result, even if magnetic dipole-dipole attractive interactions are present, the restricted movement within the more viscous medium hinders the particles from reorganizing into chain-like structures.

When using 0,01% w/v IOPs (green and blue curves), a variation of GelMA concentration greatly affected particles' ability to self-assemble into aligned structures. With 8% w/v GelMA, it was not possible to achieve a proper organized microstructure: only few small aggregates were formed (see *Fig. 5.1*, fourth line), with an average length of 11 μ m (see *Fig. 5.2*). Instead, with 5% w/v GelMA, it was possible to appreciate a progressive evolution of particles arrangement in chain-like structures, which started to be appreciable after 20 min, and whose average length kept increasing until 30 min, reaching a final mean length of 23 μ m (see *Figure 5.2*).

At higher particle concentration (0.2% w/v), self-assembly occurred much faster and was less affected by the increase in matrix viscosity. Within the 5% GelMA formulation, after 5 minutes, an average chains' length of 20 µm was observed, and it kept increasing until 32 µm after 20 minutes. At 0.02% w/v IOPs, the alignment was slightly slowed inside the 8% GelMA matrix, especially in the first 10 min, but after 20 minutes it gave rise to homogeneously distributed microstructures with an average chains' length of 30 µm. Also, the impact of matrix viscosity on the self-assembly profile was less severe at higher particles concentration: increasing GelMA concentration from 5% w/v to 8% w/v severely hindered chains formation at 0.01% w/v IOPs, while it had just a minor influence at 0.02% w/v IOPs. In Figure 5.2, that is highlighted by the fact that the two curves related to 0.02% IOPs are very close to each other, while the curves related to 0.01% IOPs are more distant. These observations suggest that at higher particle concentration, the magnetic dipolar interactions become sufficiently strong to dominate over viscous resistance, such that variations in matrix viscosity result in only minor influence in the self-assembly outcome. Conversely, at lower concentration, the interaction forces are probably only slightly greater than the viscous drag force, making the assembly process highly sensitive to changes in viscosity.

On the other hand, a negative effect that arose at higher particles' loading (0.02%) was the undesired migration of magnetic aggregates toward the edges of the sample, i.e. towards the magnets. When assembled within the 5% GelMA matrix, after 30 min all the aggregates accumulated at the edge of the sample, depleting its center (see *Figure 5.1*). For this reason, the corresponding curve, reported in *Figure. 5.2* (brown), interrupts at 20 min. This net movement is driven by magnetic particle – field interaction forces, arising in the presence of non-perfectly uniform magnetic fields and leads to particles movement toward regions of stronger magnetic field [70]. A gradient of 8mT is present from the center to the edge of the sample. Within the 8% GelMA precursor, the increased viscosity reduced the speed of undesired migration: after 30 minutes, aligned microstructures are still present in the center, but are shorter than those achieved after 20 min, due to the local reduction of IOPs

concentration. The absence of this phenomenon at lower IOP concentrations can be explained by the existence of a critical aggregate size, above which the magnetic field-aggregate interaction force becomes predominant over viscous resistance. This critical size is not reached at lower particle concentrations, where the aggregates remain significantly smaller, allowing the self-assembly process to prevail over migration. The field-particle interaction force is indeed proportional to the magnetic field gradient and magnetic particle volume [70]. The term "particle" is used to indicate an aggregate of IOPs in this case.

The use of 0.005% w/v IOPs did not lead to any significant chains' formation, not even after 90 minutes of magnetic exposure. Theoretically, the assembly should occur when the two particles are so close that their magnetic dipolar interaction overcomes the thermal energy. Hu et al. report that, for a specific set of working conditions, a maximum inter-particle distance (i.e. a minimum MNPs concentration) exists, above which the dipolar interaction energy is insufficient to drive particles' self-assembly and stabilize it against thermal disruption [70].

Summarizing, this set of experiments showed that by tuning particles loading and matrix composition (i.e. viscosity) it is possible to control the formation and morphology of aligned aggregates of particles within the hydrogel. The minimum particles concentration that leads to significant alignment was 0. 01% w/v, but only when performed within the less viscous (GelMA 5% w/v) hydrogel precursor. Results also highlight the possibility to obtain better morphologies, meaning longer and denser anisotropic assemblies, by increasing MNPs concentration, even though that is not expected to be beneficial for xolographic printing. In the perspective of minimizing the amount of nanofiller to be introduced within the photo-resin for XOLO printing, one goal of this preliminary analysis was to identify the minimum concentration of 30 nm-sized IOPs that could be aligned under the application of a 162 mT magnetic field, in the hope that such concentration would also be compatible with xolographic 3D printing of the nanocomposite resin.

5.2 Integration of IOPs self-assembly with XOLO technology

5.2.1 Printability of magnetic photoresins

Unfortunately, the introduction of magnetic particles severely compromised the printability of the photo-resins in the Xube. Even using the pristine photo-resin (without particles) the result of the printing process was suboptimal, yielding poorly defined objects (see *Figure 5.3.A*). The addition of 0.005% w/v of 30 nm PEG-capped IOPs was sufficient to completely prevent the

formation of printed objects resembling CAD geometry. In fact, the presence of magnetic nanoparticles caused a strong attenuation of the two UV semi-sheets irradiating the cuvette from opposite sides. As a consequence, the only way to enable the UV light to penetrate through the resin volume was to increase its intensity to levels so high to induce undesired UV-induced photopolymerization. Attempts to adjust the energy input failed to localize the curing process: at lower intensities, partial polymerization occurred only at the lateral edges of the resin, leaving the central region uncured. Increasing the UV intensity simply expanded these overcured lateral areas until they merged at the center, ultimately leading to complete curing of the entire UV-irradiated sheet of resin, as shown in Figure 5.3 B. Any geometrical detail of the intended object can be distinguished. When the IOP concentration was doubled to 0.01% w/v, the decrease of the resin's printing performance became even more pronounced. In these conditions, achieving complete UV-induced photopolymerization along the x-axis was not even possible due to the stronger light attenuation. Increasing the energy input only minimally expanded the laterally cured regions along the x-axis, which remain separated from each other, as shown in Figure 5.3 C. Due to the unsatisfactory results obtained with Xube, the array of tested printing parameters combinations is not reported.

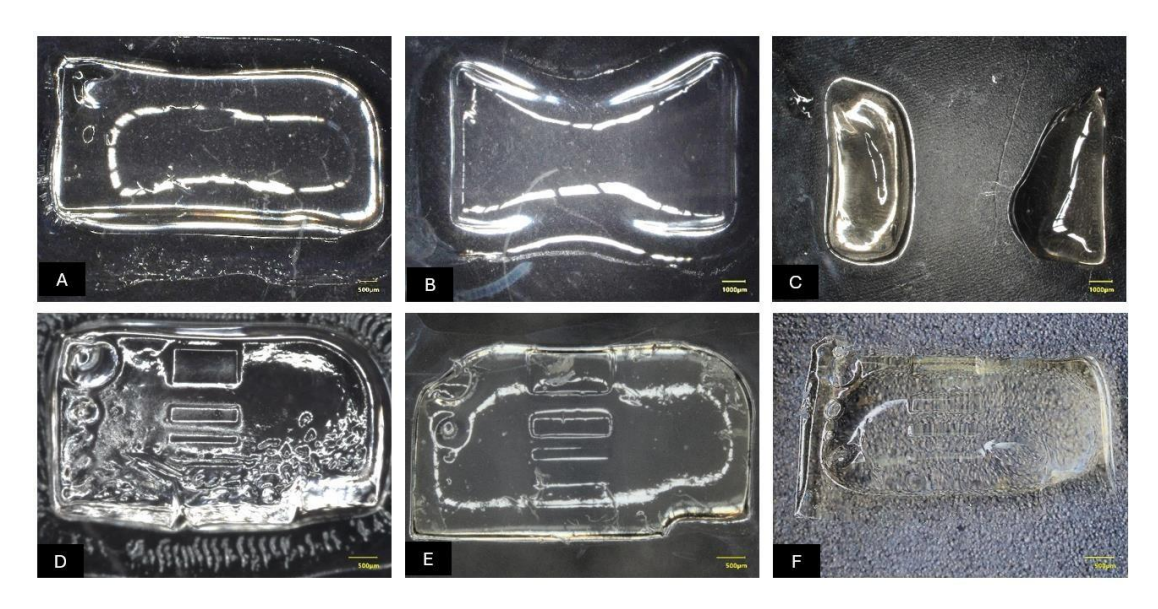


Figure 5.3. Best results using Xube with (A) 0%, (B) 0.005%, (C) 0.01% IOPs and Xube² with (D) 0%, (E) 0.005%, (F) 0.01% IOPs

Differently, when using the Xube² version of XOLO printer, the printing resolution was greatly improved. The printing process was achievable even in the presence of magnetic nanoparticles, even if in a reduced printability window, and just for low IOPs loadings (see *Figure 5.3*).

In the presence of embedded particles, UV light propagation is strongly affected by scattering and absorption. Each nanoparticle partially blocks or deviate the path of the electromagnetic wave, generating shadowed regions where fewer radicals are formed and polymerization is

hindered. An inhomogeneous activating UV light sheet ultimately lead to a disuniform curing process [94], [96], [97]. If the illumination remains static, the shadowed regions caused by light-particles interaction persist, leading to inhomogeneous DCPI activation

The improved printing performance of the Xube² system with nanocomposite photoresins probably arises from the dynamic uniformation of the activating UV-light sheet favoured by the use of a vibrating MLA system: thanks to the rapid variation of the orientation of the microbeams composing the light sheet shadows are constantly displaced and the resin experiences a more uniform UV irradiation.

The introduction of magnetic nanoparticles in the photo-resin lead to three main changes in terms of printability of the composite material.

In the first place, the energy needed to achieve the complete photopolymerization of the printed object was higher when increasing the IOPs concentration. It changed from 20 mJ/mm² for the pristine hydrogel matrix to 32.5 mJ/mm² with the introduction of 0.005% w/v IOPs, then to 42.5 mJ/mm² for 0,01% IOPs. Printability windows for each hydrogel formulation are reported in *Figure 5.4*.

Secondly, an increase in the concentration of nanofiller caused a reduction in resolution. In fact, the resolution of printed objects with 0.005% IOPs (see *Figure 5.3 E*) was basically the same of that of the pristine resin (see *Fig. 5.3 E*) but started to worsen at 0.01% IOPs, with printed parts showing less defined features (see *Fig. 5.3 F*).

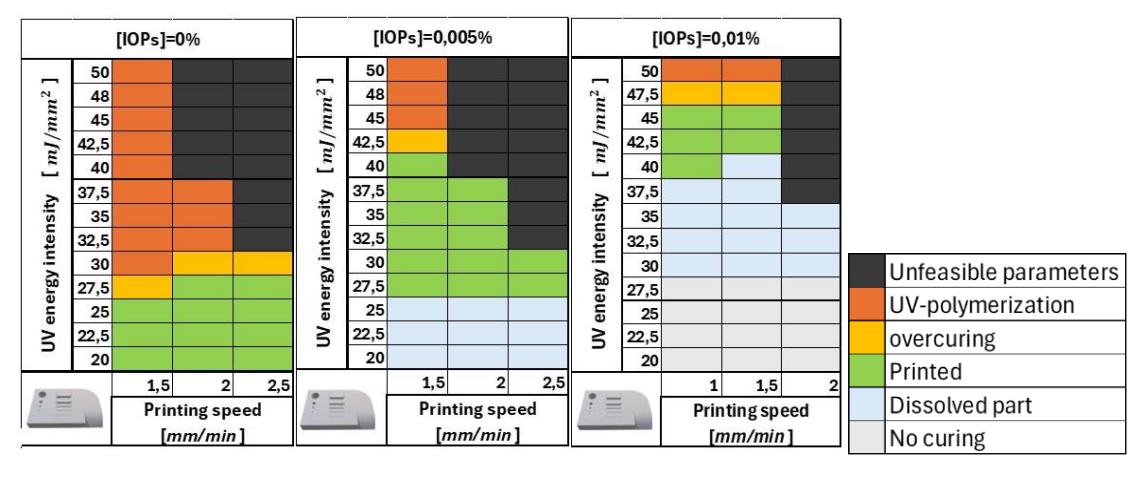


Figura 5.4 Parameters regions identified for each photo-resin composition. A definition of the different possible printing outcome is provided in Section 3.3

Finally, the composite printed constructs exhibited a crosslinking gradient along the x-axis. For the 0.01% IOPs resin, energy values comprised between 35 and 40 mJ/mm² resulted in printed

object that, upon washing with hot water to dissolve uncured material, consistently fractured in the center. This behavior could be explained considering different crosslinking densities towards the center, which caused a gradient of mechanical properties. Only for energy input equal or greater than 42.5 mJ/mm², nicely printed parts could be obtained (see Figure 5.3 F). The impact of uneven polymerization along the x-axes became significant when 0.02% w/v IOPs were introduced within the resin, making it impossible an optimization of the printing parameters. For energy input values of 50-52.5mJ/mm², the lateral edges were well polymerized and structurally stable, whereas the curing of central region was incomplete. As a result, the two edges were connected only by a thin and poorly defined portion of hydrogel, displaying a markedly reduced thickness along the z-axis in the central area. Solidified objects were extremely soft, with handling difficulties, making complex the possibility of taking pictures of their undeformed shape. One example is reported in Figure 5.5 A. Positive and negative features of the CAD geometry cannot be distinguished. When increasing the energy input up to 55 mJ/mm², the central part of the object was correctly polymerized, but the two edges resulted uncontrollably UV-cured (see Figure 5.5 B), so that a trade of could not be found. Results suggest that it is not possible to optimize printing parameters for the photo-resin containing 0.02% w/v IOPs (or higher), with the currently available technology.



Figure 5.5 Cured objects obtained with Xube² (A) 0.02% IOPs, 50-52.5mJ/mm ² (B) 0.02% IOPs, 55 mJ/mm ² (C) 0.03% IOPs, 60 mJ/mm ²

When further increasing IOPs loading up to 0.03% w/v laden photoresin, a net interruption of the photopolymerization occurs after the first mm of penetration along the x-direction, even when using energy input high enough to cause lateral UV-hardening (60mJ/mm^2), as shown in *Figure 5.5C*.

Due to the high degradation of printing performance observed when switching from 0.01% to 0.02% w/v IOPs loading, 0.01% w/v was considered as the highest printable concentration of 30-nm sized, PEG-capped IOPs. For this reason, this was the amount of IOPs employed to test cells response in magnetic hydrogel scaffolds obtained by casting.

5.2.2 Stabilization of anisotropic pattern in printed objects

Using a combination of 1.5 mm/min and 45 mJ/mm², parallelepipeds of 3 mm x 3 mm x 2 mm could be nicely printed. In Figure 5.6 the printed object (left) and the embedded magnetic structures (right) are shown.

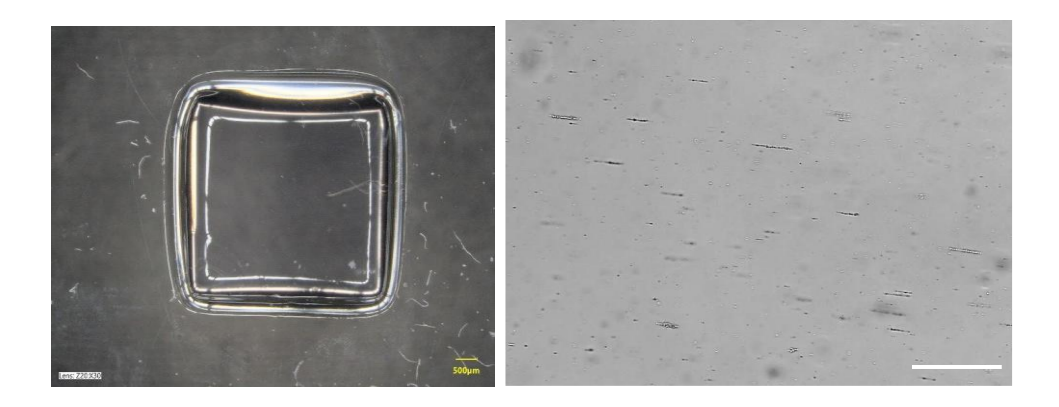


Figure 5.6 Printed parallelepipeds (A); embedded microstructures (B).

Although less uniform, an anisotropic microstructure composed of oriented aggregates was successfully obtained within the printed objects. This result confirmed the hypothesis that the thermal gelation of the GelMA-containing hydrogel matrix is an effective strategy to stabilize the assembled particle arrangements, enabling pre-alignment prior to the printing process. This achievement represents a key advancement that allows the integration of the selfassembly approach into volumetric 3D printing technology. The use of a thermo-responsive hydrogel formulation is crucial, as it provides a means to decouple the magnetic alignment step from the printing process.

5.3 cell culture

5.3.1 Live/dead essay

Fluorescent images of Calcein-AM/PI stained cells are reported in Figure 5.7.

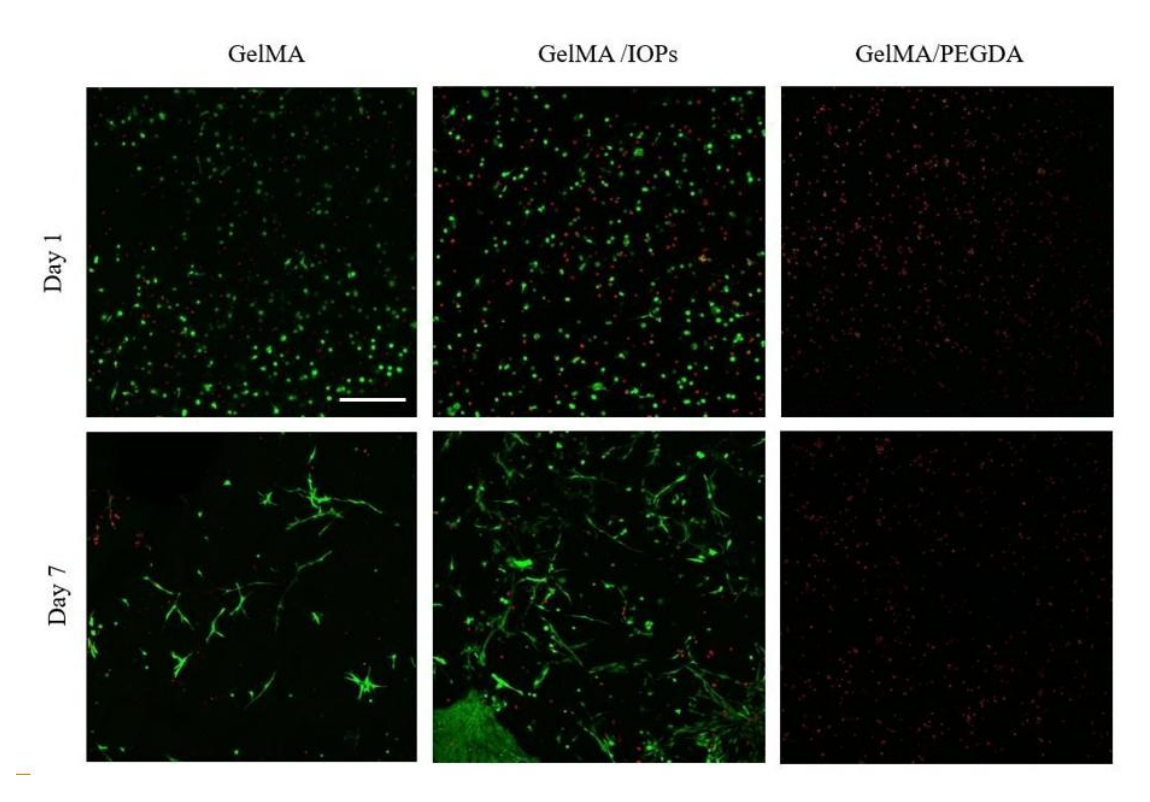


Figura 5.7 Fluorescent images of labeled cells. Green cells are alive (Calcein), red cells are dead (PI). Scalebar 200 µm

Results show that cell viability is very high inside GelMA and GelMA/IOPs hydrogel, demonstrating the cytocompatibility of the PEG-capped iron oxide particles at 0,01% w/v concentration. On the contrary, the introduction of 10% v/v PEGDA (Mw=575) is detrimental for cell viability. After 24h post embedding, almost all cells died, and cell viability is almost nul. This result is in line with previous reports of cytotoxic effect of PEGDA at low molecular weigths (<1000) even at 1.5 % w/v. However, the introduction of PEGDA within the composite photoresin is fundamental to guarantee printability. The presence of low Mn PEGDA significantly enhances hydrogel printability, as it allows for higher crosslinking speed [96]. Especially in the case of composite formulations, involving all the mentioned challenges for XOLO printing introduced by the presence of magnetic particles, ensure fast kinetics is crucial. In their work, Stoecker et al. succeeded in bio-print cell-laden, pristine GelMA constructs encapsulating viable cells. However, they used a concentration of GelMA of 10% w/v. In our case, due to the weaker magnetic responsiveness of the nanoparticles system at such ultra-low

concentrations (0.01% w/v), 8% w/v GelMA was already too high concentration to enable the field-driven self-assembly, working with the previously described experimental conditions (H=160mT; water bath at 38°C). A 10% w/v GelMA matrix is too viscous to avoid their field-driven alignment. For this reason, 5% w/v GelMA was selected as maximum amount of GelMA that can be introduced in the photoresin. Preliminary attempts to print bare 5% GelMA hydrogels were performed, but without success. However, the reduction of PEGDA amount and/or the increase of its Mw could improve the cytocompatibility of the matrix, at the cost of printing resolution. The biggest challenge in the field of bioprinting is to find a trade-off between cytocompatibility and printing requirements. PEGDA chains could also be modified with cell adhesive motives to enhance its ability to support cells' life.

5.3.2 Phase-contrast imaging

Phase contrast images of C2C12 cells cultured inside three different matrices (GelMA, GelMA/rIOPs and GelMA/aIOPs) on day 1, 3 and 6 are reported in *Figure 5.8*. The name "GelMA/rIOPs" indicates GelMA hydrogels (5% w/v) loaded with randomly dispersed IOPs, cured right after casting. "GelMA/aIOPs" refers to the constructs with aligned IOPs structures.

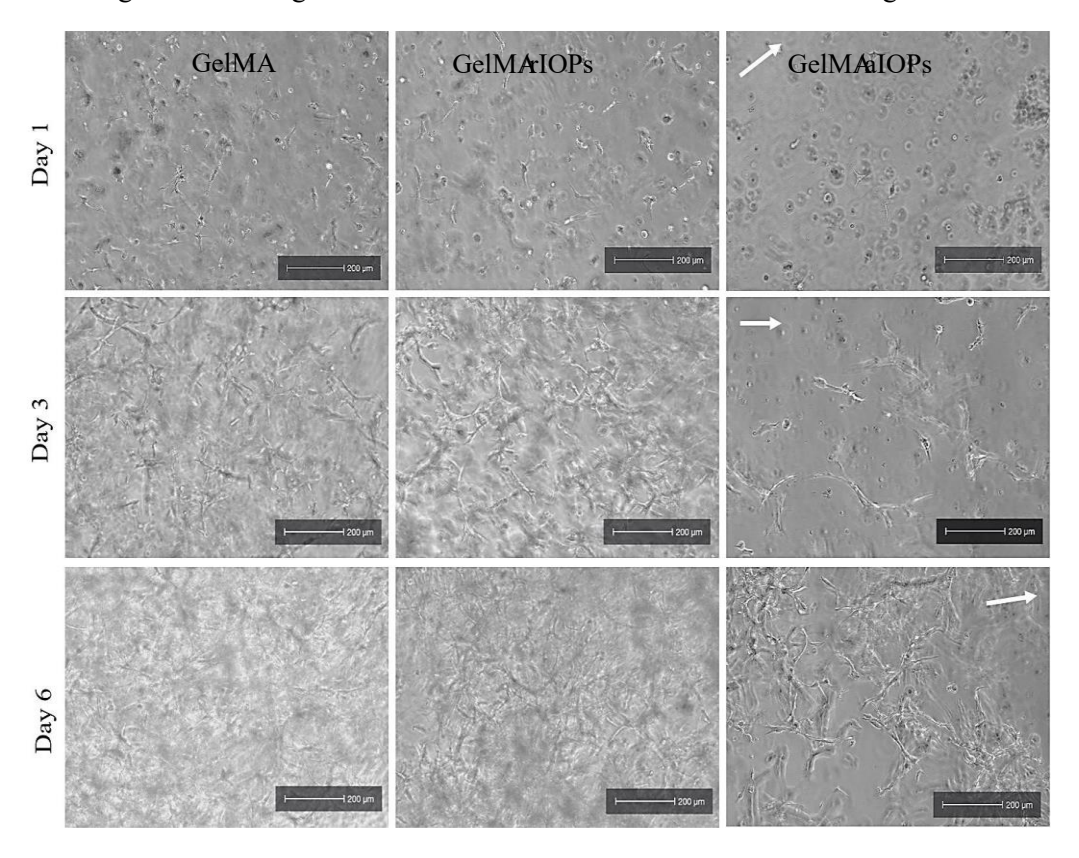


Figure 5.8 Phase contrast images of C2C12 cells cultured .inside three different GelMA-based matrices GelMA, GelMA/rIOPs and GelMA/aIOPs) on day 1, 3 and 6. The white arrow indicates the direction of the magnetic chains.

Cells embedded inside pristine GelMA and GelMA/rIOPs hydrogels started spreading after 24h post embedding, while a large number of cells appeared still rounded inside GelMA/aIOPs groups, where spreading occurred slower and in a heterogeneous manner across the construct. Short myotubes start forming at day 3, whereas inside GelMA and GelMA/rIOPs cells had already organized into interconnected networks. Overall, a clear impairment in myogenic morphological organization is observed in Gelma/aIOPs groups, with only sparse myotube formation, typically confined to aggregates.

The undesirable behavior observed in GelMA/aIOPs, compared with GelMA/rIOPs, whose chemical composition is identical, could be explained considering the higher stress at which cells were subjected during the fabrication of the anisotropic hydrogel. In fact, cells stay in contact with the hydrogel precursor solution for a longer period before gelation. For the whole duration of the self-assembly step, cells stay in contact with unreacted methacrylic groups and photoinitiator molecules (LAP) and are deprived from nutrients provided by the culture medium. However, this drawback was never reported in the reviewed literature, not even for bio-fabrication methods involving longer durations of magnetic exposure [71]. Furthermore, it is unlikely that the magnetic field intensity employed (~160mT) represented a cytotoxic element. Studies on the effect of magnetic stimulation of cells cultured inside magnetic 3D matrices report promising results under the application of magnetic cycles with magnetic field amplitude up to 450mT [100]. In addition, not even the temperature could have been the reason for the hypothesized cell damage, responsible for the minor cell spreading and proliferation, since the heating set up was arranged to keep the cell-laden hydrogel at 37-38 °C. The biocompatibility of the self-assembly step is an aspect that should be taken into consideration in future studies, moving toward the minimization of the duration of the magnetic exposure. Live/dead and/or metabolic activity essay should be performed to better investigate the origin of this undesirable cell behavior.

Not only cells cultured in GelMA/aIOPs hydrogel did not grow as well as in the control groups devoid of anisotropic cues, but, from a qualitative evaluation of the contrast images, they did not even display the intended preferential alignment along the direction of the magnetic fibers at day 6 (see *Figure 5.8*). Cells morphology in GelMA and GelMA/rIOPs evolved basically in the same way, being extremely similar between the two matrices at each time point. A dense and homogeneous network of interconnected myocytes is achieved at day 6, consistent with previous reports in which C2C12 cells were embedded in GelMA matrices [102]. The poor spreading and rounded morphology exhibited by C2C12 myoblasts in GelMA/aIOPs was similar to that observed by Costantini et al. inside more densely crosslinked and stiffer GelMA matrices.

Higher magnification images of GelMA/aIOPs samples (day 2 and 3) are reported in *Figure* 5.9, to show the relative dimension of C2C12 cells and IOPs chains. Within the first three days, it was possible to qualitatively observe an apparent preferential alignment of the first spreading cells along the magnetic chains direction. At day 6, when a denser network of cells was formed in GelMA/aIOPs hydrogels, it was no longer noticeable.

Chains' length is higher than cells' diameter in the initial round state. After 2-3 days, chains' dimension is still comparable with cells size. However, once myoblasts mature into bigger myotubes, magnetic fibrillar cues become too small to act as physical confinement for cells' directional growth.

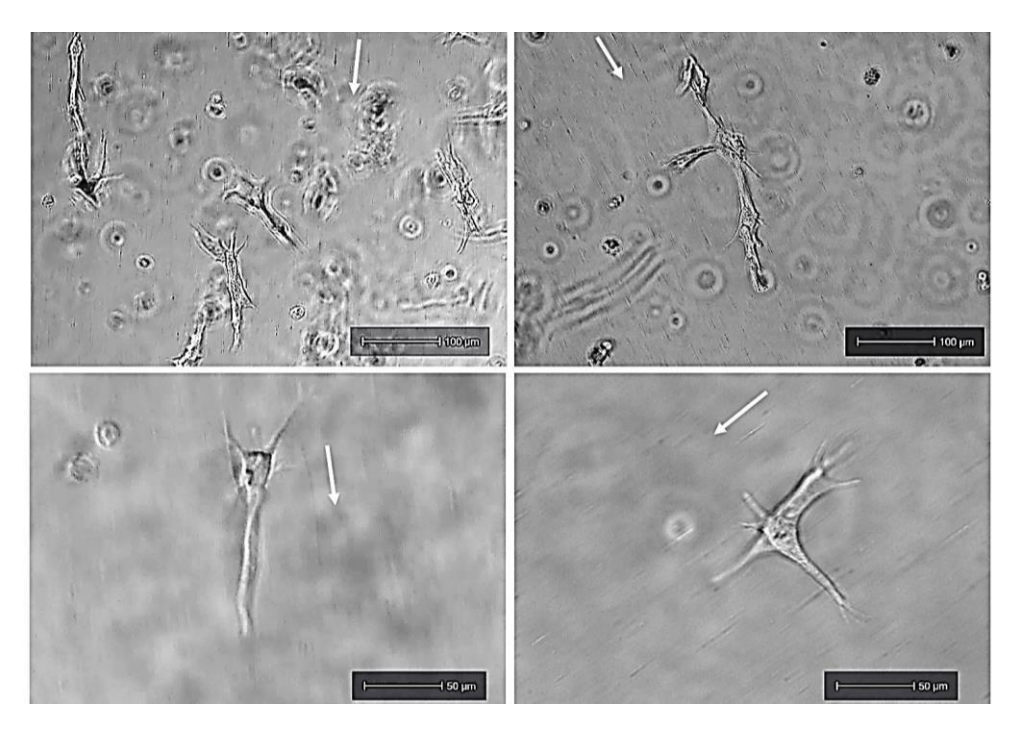


Figure 5.9 Higher magnification phase contrast images of C2C12 inside GelMA/aIOPs (day 2 and 3), surrounded by self-assembled IOPs chains

5.3.3 Myotubes orientation

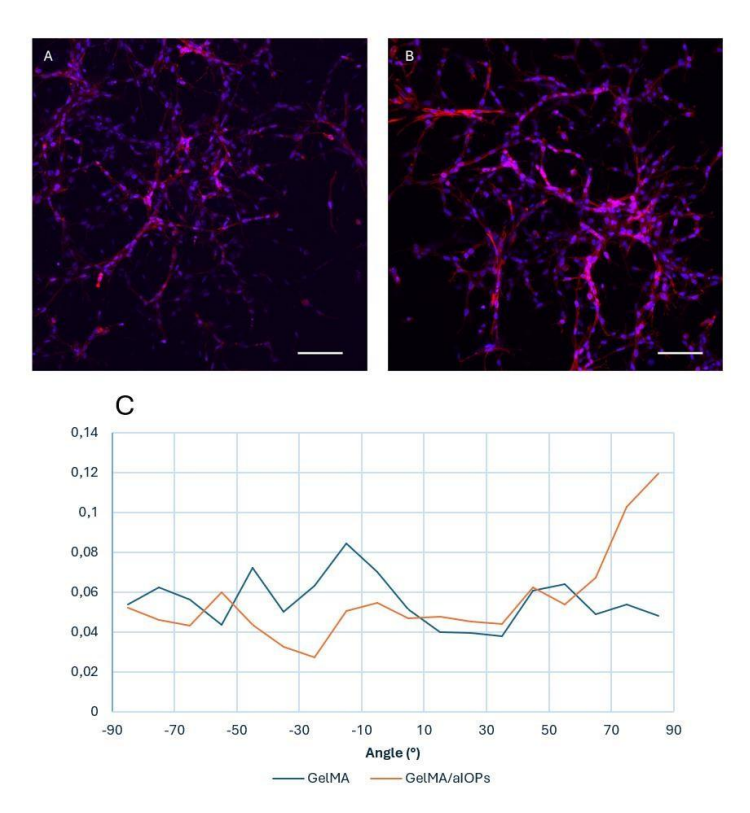


Figura 5.10 Fluorescent images of C2C12 stained for actine (red) and nuclei (blue). Scale bar 100 mm. (A) cells embedded in GelMA (B) cells embedded in GelMA/aIOPS (C) Distribution of cytoskeletal orientation (from ImageJ, OrientationJ plugin)

Images of DAPI/Phalloidin-stained cells on day 6 are reported in *Figure 5.10 A,B*. Quantification of the degree of local orientation confirmed the absence of a preferential alignment of cells along the direction of the IOPs chains (see *Figure 5.10 C*).

For bare GelMA hydrogels the distribution is flatter, indicating a high level of structural isotropy, with no orientation being more probable for the structures. For GelMA/aIOPs, instead, a peak at around 90° is observed. However, this cannot be justified by the presence of the anisotropic cues, as the orientation of the embedded chains is 0°. Fluorescent images taken at different locations within the GelMA/aIOPs hydrogel give very different orientation distribution (not reported), which can likely be ascribed to random effects. Particles aggregates achievable with 0.01% w/v 30nm-sized IOPs are too sparsely packed, and that severely compromises their effectiveness as contact guidance to direct cells alignment.

This finding is coherent with the results reported by Pardo et al., that analyzed the effect of the concentration of magnetic building blocks on the degree of anisotropic organization imparted to the cells [71]. They concluded that at very low concentration of magnetic filler (0.25% w/v), the wide inter-chain spacing minimizes direct interactions with cells, thereby enabling the almost unrestricted cell spreading and the establishment of randomly oriented intercellular

connections. They found that a minimum magnetic loading of 0.1 mg/mL was required to achieve the alignment of a significant fraction of cells along the anisotropic axis of the hydrogel. This value is 10 times higher than the IOPs concentration employed in the present work, which was limited by the printing requirements imposed by Xolography 3D printing.

6. Conclusions

The spatially aligned organization of cells is a key feature associated with the function of many biological tissues, such as skeletal muscle. Structurally anisotropic hydrogels emerged as scaffold platforms capable of directing cell alignment. An emergent versatile method to impart hydrogel scaffolds with anisotropic, cell instructive, physical cues is the magnetic pattern approach. It consists in the remote manipulation of magnetic nano- or micro- fillers (building blocks) within the liquid, cell-laden hydrogel precursor before gelation. The application of external magnetic field directs their spontaneous assembly (self-assembly) into head-to-tail arrangements aligned with the field lines.

The integration of bioprinting technologies with the magnetic-field driven self-assembly approach may pave the way for the fabrication of complex-shaped, intrinsically anisotropic constructs, with unprecedented control over structural features from the micro- to the macroscale. To date, the magnetically driven alignment of magnetic building blocks (e.g. nanoparticles, microfibers) has been implemented with extrusion-based and Digital Light Processing (DLP)-based printing technologies, the latter not for cell-culture application

Light-assisted techniques, beyond their superior performances compared to the other AM methods, are particularly suitable for integrating the self-assembly, since the arrangement of magnetic nanomaterials can be programmed within the liquid photocurable resin contained in the vat and rapidly stabilized upon light-induced polymerization.

Within this framework, the present thesis investigated a further step ahead in the development of advanced hydrogel scaffold for SkM TE. It aimed to integrate the magnetic alignment of nanoparticles into a cell-laden photoresin, processable via Xolography-based 3D printing, to fabricate intrinsically anisotropic hydrogel scaffolds capable of guiding the alignment of encapsulated myoblasts.

The hydrogel formulation combined GelMA, for cell adhesion and thermo-responsiveness, with PEGDA, for mechanical stability. PEG-capped iron oxide nanoparticles of 30 nm were incorporated as magnetic building blocks, while C2C12 myoblasts served as the cellular model. A thermo-responsive component (GelMA) enabled pre-alignment of nanoparticles outside the printer and preserved the anisotropic structures during Xolographic printing. This approach allowed for iterative optimization of self-assembly without material loss, as GelMA reversibly gels at low temperatures.

The first phase of the study focused on the characterization of the self-assembly process in the absence of cells at 37°C. It was analyzed the effect of IOPs concentration and matrix viscosity on

the kinetics of formation and morphology of magnetic assemblies. Photo-cured solid samples were realized to "freeze" and observe the selfassembled microstructures at different time points. A magnetic field of 162mT was produced by pair of neodymium magnets to guide the alignment. It was found that 0.01% w/v IOPs was the minimum concentration to form aligned microstructures, but effective assembly only occurred in the less viscous 5% w/v GelMA hydrogels, whereas the 8% w/v GelMA formulation prevented the formation of anisotropic patterns. Higher nanoparticle concentrations (0.02% w/v) accelerated self-assembly and allowed alignment even in more viscous matrices, although concentrations above 0.01% compromise optical transparency, which is crucial for Xolographic volumetric printing.

The second part of the work aimed at integrating the self-assembly within the printing process. To achieve this, the printability of the nanocomposite resin was first evaluated to determine suitable particle concentrations and printing parameters. Two versions of the XOLO printer were compared: the older Xube with the newer Xube². The Xube² printer exhibited superior printing performance, thanks to its enhanced optical system, allowing for the generation of a more uniform activating light sheet, compared to Xube. Only the Xube² enabled the successful printing of composite resins with IOPs loading up to 0.01% w/v, whereas higher particles loadings gave rise to uneven polymerization profiles, attributable to excessive light scattering and absorption. 0.01% w/v was established as the maximum concentration of 30 nm PEG-capped IOPs suitable for Xolographic printing, and it was the value selected for the subsequent phase, where it was demonstrated the possibility to leverage temperature-induced, physical gelation of the GelMA-containing photo-resin to stabilize the selfassembled microstructure within the volume of photo-resin inside the cuvette, to preserve them during printing. The customized holder designed to keep in place magnets and mold was adapted to hold the XOLO cuvette, rather than the PDMS mold, in the center of the magnetic field, to ensure a uniform magnetic field distribution throughout the resin volume. After 20 min of magnetic exposure, the whole assembled system was immersed in an ice-bath for 10 min to induce thermal gelation of the hydrogel matrix, then small cubes were printed, using previously optimized printing parameters, and imaged. Results confirm the successful formation and preservation of aligned microstructure within the printed object.

In the end, cell behavior inside the magnetic hydrogels was investigated. At first, C2C12 cells were incapsulated within bare GelMA 5% w/v, GelMA 5% w/v /PEGDA 10% w/v and GelMA 5% w/v /IOPs 0.01% live/dead essay was performed to evaluate the cytocompatibility of the hydrogel components. Results confirmed that iron oxide nanoparticles were highly cytocompatible, whereas PEGDA inclusion reduced cell viability, highlighting a trade-off between printability and biocompatibility. Finally, a second cell casting was performed to assess the effect of the presence of magnetically aligned microstructures on cell morphology. C2C12 cells were encapsulated within

GelMA/aIOPs (randomly distributed IOPs) and GelMA/aIOPs (aligned IOPs). GelMA/aIOPs sample were realized by inducing Despite the successful pre-alignment of nanoparticles also in the presence of cells, the oriented microstructures did not effectively promote myoblast alignment. This can likely be attributed to the insufficient density of magnetic aggregates, due to the ultra-low concentration of IOPs, constrained by the optical requirements of volumetric printing. In practice, closely spaced, fibrous microstructures are necessary to physically guide cells along a preferential axis, but this conflicts with the need for transparent hydrogel formulations for Xolography. Consequently, both isotropic and anisotropic samples exhibited random cellular spreading. Additionally, GelMA/aIOPs samples showed reduced network density, suggesting subtle cytotoxic effects from the alignment process, which could not be explained, thus highlighting the need for further optimizations (e.g. reduced alignment duration).

This work introduces a conceptual and technical advancement that expands the applicability of magnetic fieldinduced self-assembly to volumetric 3D printing. Central to this achievement is the use of a thermos-responsive hydrogel component (GelMA). This strategy decouples the self-assembly from the printing step, eliminating the need for real-time magnetic control within the printer, as required in previous studies. In addition, the reversibility of thermal gelation emerges as a key functional advantage, as it allows the resin to be reheated and remixed to repeat the assembly before printing, enabling iterative optimization without material loss and precise control over the final microstructure.

While the ultimate goal of producing anisotropic, cell-laden scaffolds capable of guiding myoblast alignment was not achieved, this thesis identified key constraints imposed by material composition and printing technology, providing essential insights for future attempts to 3D print functionally anisotropic skeletal muscle constructs. To effectively confine cellular spreading along preferential axes, closely spaced fibers are required to act as topographical cues. An intrinsic limitation of the integrated approach lies in the conflicting requirements of producing densely packed oriented fibers to effectively confine cell spreading along preferential axes while, at the same time, preserving the requisite of optical transparency for xolography inks.

Further optimization will be required in future work to balance the effects of nanoparticles concentration, hydrogel rheology, cytocompatibility, and optical transparency. In this thesis, the optimization could not be refined in detail, as it was primarily aimed at establishing a foundational framework. Given the exploratory nature of the study, with several parameters being investigated for the first time, the range of variables tested was necessarily limited. For example, the self-assembly and printability should be investigated for IOPs concentrations comprised between 0.01 and 0.02% w/v. Also, due to the limited timeframe of the work, it was not possible to perform a

thorough optimization of the photoresin composition. Newly synthetized DCPI or co-initiator, or different ratios between the resin components, could greatly enhance the printability of the composite material, thus increasing the maximum printable amount of magnetic particles.

To address PEGDA's cytotoxic effect, the hybrid hydrogel formulation could be redesigned using alternative, biocompatible crosslinkable monomers or oligomers that provide similar photoreactivity and mechanical stability. Promising candidates include methacrylated bio-macromolecules like Silk Fibroin Methacrylate (SilMA) or Hyaluronic Acid Methacrylate (HAMA) [103], or even PEGDA derivatives, covalently functionalized with cell-adhesive RGD peptides [104].

In addition, the use of MNPs with larger volume or cubic shapes could be explored. Larger superparamagnetic particles may provide stronger magnetic moments, which proved to improve the alignment efficiency, even in more viscous photo-resins [70]. Cubic morphology improves magnetic anisotropy, thereby enhancing magnetic responsiveness even at reduced particle sizes [105]. This could facilitate stronger magnetic dipolar interactions and more efficient field-induced self-assembly, compared to their spherical counterparts

Finally, with the evolving of the VAM technology, improvements in the optical setup for the generation of the light beams could allow to increase the amount of magnetic filler which can be introduced within the photo-resin, in the same way the Xube² allowed the successful printing of well defined hydrogel constructs using composite formulations that could not be printed with the precedent Xube version, way more sensible to light scattering.

In conclusion, the work highlights both the potential and the intrinsic challenges emerging from combining bottom-up microstructural control with state-of-the-art volumetric printing, offering a roadmap for the development of next-generation magnetically patterned, cell-laden hydrogels that can merge architectural complexity with biological functionality.

References

- [1] K. H. Nakayama, M. Shayan, and N. F. Huang, "Engineering biomimetic materials for skeletal muscle repair and regeneration" *Advanced Healthcare Materials*, vol. 8, no. 5, p. 1801168, 2019.
- [2] B. T. Corona, J. C. Rivera, J. G. Owens, J. C. Wenke, and C. R. Rathbone, "Volumetric muscle loss leads to permanent disability following extremity trauma " *Journal of Rehabilitation Research & Development*, vol. 52, no. 7, 2015.
- [3] E. Mercuri, C. G. Bönnemann, and F. Muntoni, "Muscular dystrophies" *The Lancet Neurology*, vol. 18, no. 4, pp. 402–414, 2019.
- [4] A. Khodabukus, "Tissue-engineered skeletal muscle models to study muscle function, plasticity, and disease "*Frontiers in Physiology*, vol. 12, p. 619710, 2021.
- [5] C. A. Vacanti, "The history of tissue engineering" *Journal of Cellular and Molecular Medicine*, vol. 10, no. 3, pp. 569–576, 2006.
- [6] R. Langer and J. P. Vacanti, "Tissue engineering" Science, vol. 260, no. 5110, pp. 920–926, 1993.
- [7] F. Berthiaume, T. J. Maguire, and M. L. Yarmush, "Tissue engineering and regenerative medicine: History, progress, and challenges" *Annual Review of Chemical and Biomolecular Engineering*, vol. 2, pp. 403–430, 2011.
- [8] F. J. O'Brien, "Biomaterials & scaffolds for tissue engineering" *Materials Today*, vol. 14, no. 3, pp. 88–95, 2011.
- [9] S. Stratton, N. B. Shelke, K. Hoshino, S. Rudraiah, and S. G. Kumbar, "Bioactive polymeric scaffolds for tissue engineering" *Bioactive Materials*, vol. 1, no. 2, pp. 93–108, 2016.
- [10] Y. Ikada, Tissue Engineering: Fundamentals and Applications. Elsevier, 2006.
- [11] M. W. Tibbitt and K. S. Anseth, "Hydrogels as extracellular matrix mimics for 3D cell culture" *Biotechnology and Bioengineering*, vol. 103, no. 4, pp. 655–663, 2009.
- [12] A. Sivashanmugam, R. Arun Kumar, M. Vishnu Priya, S. V. Nair, and R. Jayakumar, "An overview of injectable polymeric hydrogels for tissue engineering "*European Polymer Journal*, vol. 72, pp. 543–565, 2015.
- [13] Y. S. Zhang and A. Khademhosseini, "Advances in engineering hydrogels" *Science*, vol. 356, no. 6337, 2017.

- [14] E. M. Ahmed, "Hydrogel: Preparation, characterization, and applications A review "Journal of Advanced Research, vol. 6, no. 2, pp. 105–121, 2015.
- [15] S. Besarab, "Artificial extracellular hydrogel matrix for treatment of myocardial infarction" *Ukrainian Journal of Cardiology*, vol. 1, pp. 102–108, 2018.
- [16] S. Thakur, V. K. Thakur, and O. A. Arotiba, "History, classification, properties and application of hydrogels: An overview "in *Hydrogels. Gels Horizons: From Science to Smart Materials*, V. Thakur and M. Thakur, Eds. Singapore: Springer, 2018, pp. 23–70.
- [17] S. Besarab, "Schematic diagram of the hydrogels formation mechanism [Figure] " in Artificial Extracellular Hydrogel Matrix for Treatment of Myocardial Infarction (preprint). ResearchGate, 2021.
- [18] J. M. Dodda, K. Deshmukh, D. Bezuidenhout, and Y.-C. Yeh, "Hydrogels: Definition, history, classifications, formation, constitutive characteristics, and applications " in *Multicomponent Hydrogels: Smart Materials for Biomedical Applications*. Royal Society of Chemistry, 2023, pp. 1–25.
- [19] O. Wichterle and D. Lim, "Hydrophilic gels for biological use" *Nature*, vol. 185, pp. 117–118, 1960.
- [20] J. Elisseeff, K. Anseth, D. Sims, W. McIntosh, M. Randolph, and R. Langer, "Transdermal photopolymerization for minimally invasive implantation."
- [21] H. Taneja, S. M. Salodkar, A. S. Parmar, and S. Chaudhary, "Hydrogel based 3D printing: Bioink for tissue engineering."
- [22] Q. Zheng, A. Jiao, M. Shang, H. Ji, X. Li, Z. Jin, L. Jiang, and C. Qiu, "Advances in intelligent response and nano-enhanced polysaccharide-based hydrogels: Material properties, response types, action mechanisms, applications."
- [23] S. K. H. Gulrez, S. Al-Assaf, and G. O. Phillips, "Hydrogels: Methods of preparation, characterization and applications."
- [24] W. Hu, Z. Wang, Y. Xiao, S. Zhang, and J. Wang, "Advances in crosslinking strategies of biomedical hydrogels" *Biomaterials Science*, vol. 7, no. 3, pp. 843–855, 2019.
- [25] W. Hu, Z. Wang, Y. Xiao, S. Zhang, and J. Wang, "Advances in crosslinking strategies of biomedical hydrogels" *Biomaterials Science*, vol. 7, no. 3, pp. 843–855, 2019.
- [26] P. Gacesa, "Alginates" Carbohydrate Polymers, vol. 8, no. 3, pp. 161–182, 1988.

- [27] S. Chaterji, I. K. Kwon, and K. Park, "Smart polymeric gels: Redefining the limits of biomedical devices" *Progress in Polymer Science*, vol. 32, nos. 8–9, pp. 1083–1122, Aug.—Sep. 2007.
- [28] C. M. Hassan and N. A. Peppas, "Structure and morphology of freeze/thawed PVA hydrogels" *Macromolecules*, vol. 33, no. 7, Mar. 11, 2000.
- [29] R. Parhi, "Cross-linked hydrogel for pharmaceutical applications: A review " *Advanced Pharmaceutical Bulletin*, vol. 7, no. 4, pp. 515–530, 2017.
- [30] D. Braun, "Origins and development of initiation of free radical polymerization processes" *International Journal of Polymer Science*, pp. 1–10, 2009.
- [31] M. K. McHale, L. A. Setton, and A. Chilkoti, "Synthesis and in vitro evaluation of enzymatically cross-linked elastin-like polypeptide hydrogels" *Tissue Engineering*, vol. 11, nos. 11–12, pp. 1768–1779, 2005. doi: 10.1089/ten.2005.11.1768.
- [32] H. Li, R. Aneja, and I. Chaiken, "Click chemistry in peptide-based drug design" *Current Opinion in Chemical Biology*, vol. 17, no. 3, pp. 284–290, 2013. doi: 10.1016/j.cbpa.2013.01.016.
- [33] N. V. Arguchinskaya *et al.*, "Properties and printability of the synthesized hydrogel based on GelMA" *International Journal of Molecular Sciences*, vol. 24, no. 3, p. 2121, 2023. doi: 10.3390/ijms24032121.
- [34] N. Davidenko *et al.*, "Evaluation of cell binding to collagen and gelatin: A study of the effect of 2D and 3D architecture and surface chemistry "*Journal of Materials Science: Materials in Medicine*, vol. 27, p. 148, 2016. doi: 10.1007/s10856-016-5763-9.
- [35] D. W. Hutmacher and E. Cukierman, "Engineering of tumor microenvironments" *Advanced Drug Delivery Reviews*, vols. 79–80, pp. 1–2, 2014. doi: 10.1016/j.addr.2014.11.001.
- [36] S. J. Bryant and K. S. Anseth, "Hydrogel properties influence ECM production by chondrocytes photoencapsulated in poly (ethylene glycol) hydrogels " *Journal of Biomedical Materials Research Part A*, vol. 59, no. 1, pp. 63–72, 2002. doi: 10.1002/jbm.10068.
- [37] M. H. Khalili, R. Zhang, S. Wilson, S. Goel, S. A. Impey, and A. I. Aria, "Additive manufacturing and physicomechanical characteristics of PEGDA hydrogels: Recent advances and perspective for tissue engineering "*Polymers*, vol. 12, no. 11, p. 2674, 2020. doi: 10.3390/polym12112674.

- [38] L. M. Weber, K. N. Hayda, and K. S. Anseth, "Cell–matrix interactions improve β-cell survival and insulin secretion in three-dimensional culture" *Tissue Engineering Part A*, vol. 14, no. 12, pp. 1959–1968, 2008. doi: 10.1089/ten.tea.2007.0271.
- [39] M. Ehrbar *et al.*, "Biomolecular hydrogels formed and degraded via site-specific enzymatic reactions" *Biomacromolecules*, vol. 8, no. 9, pp. 3000–3007, 2007. doi: 10.1021/bm700642u.
- [40] D. Loessner *et al.*, "Functionalization, preparation and use of cell-laden gelatin methacryloyl—based hydrogels as modular tissue culture platforms."
- [41] S. Bupphathong, C. Quiroz, W. Huang, P.-F. Chung, H.-Y. Tao, and C.-H. Lin, "Gelatin methacrylate hydrogel for tissue engineering applications—A review on material modifications" *Pharmaceuticals*, vol. 15, no. 2, p. 171, 2022. doi: 10.3390/ph15020171.
- [42] S. Jana, S. K. L. Levengood, and M. Zhang, "Anisotropic materials for skeletal-muscle-tissue engineering" *Advanced Materials*, vol. 28, no. 48, pp. 10588–10612, 2016.
- [43] C. F. Bentzinger, Y. X. Wang, and M. A. Rudnicki, "Building muscle: Molecular regulation of myogenesis" *Cold Spring Harbor Perspectives in Biology*, vol. 4, p. a008342, 2012.
- [44] J. A. Trotter and P. P. Purslow, "Functional morphology of the endomysium in series-fibered muscles" *Journal of Morphology*, vol. 212, no. 2, pp. 109–122, 1992.
- [45] P. P. Purslow and J. A. Trotter, "The morphology and mechanical properties of endomysium in series-fibred muscles: Variations with muscle length "Journal of Muscle Research and Cell Motility, vol. 15, no. 3, pp. 299–308, 1994.
- [46] "Diagramma del muscolo scheletrico" Quizlet. Available: https://quizlet.com/it
- [47] P. Zhuang, J. An, C. K. Chua, and L. P. Tan, "Bioprinting of 3D in vitro skeletal muscle models: A review "*Micromachines*, vol. 11, no. 7, p. 687, 2020.
- [48] M. Théry *et al.*, "The extracellular matrix guides the orientation of the cell division axis" *Nature Cell Biology*, vol. 7, pp. 947–953, 2005.
- [49] C. Gao, L. Tang, J. Hong, C. Liang, L. P. Tan, and H. Li, "Effect of laser induced topography with moderate stiffness on human mesenchymal stem cell behavior " *Journal of Physics: Materials*, vol. 2, no. 3, 034006, 2019.
- [50] J. L. Charest, A. J. García, and W. P. King, "Myoblast alignment and differentiation on cell culture substrates with microscale topography and model chemistries" *Biomaterials*, vol. 28, no. 13, pp. 2202–2210, 2007.

- [51] P.-Y. Wang, T.-Y. Hung, and W.-B. Tsai, "Modulation of alignment and differentiation of skeletal myoblasts by submicron ridges/grooves surface structure " *Biotechnology and Bioengineering*, vol. 106, no. 2, pp. 285–294, 2010.
- [52] F. Iberite, E. Gruppioni, and L. Ricotti, "Skeletal muscle differentiation of human iPSCs meets bioengineering strategies: Perspectives and challenges."
- [53] M. Castilho *et al.*, "Hydrogel-based bioinks for tissue engineering applications" *Advanced Functional Materials*, vol. 28, 1803151, 2018.
- [54] A. Pardo *et al.*, "Magnetic nanocomposite hydrogels for tissue engineering: Design concepts and remote actuation strategies to control cell fate "*Advanced Functional Materials*, vol. 31, 2006229, 2021.
- [55] N. Khuu, S. Kheiri, and E. Kumacheva, "Structurally anisotropic hydrogels for tissue engineering" *Advanced Materials*, vol. 34, 2107760, 2022.
- [56] N. F. Huang *et al.*, "Myotube assembly on nanofibrous and micropatterned polymers" *Nano Letters*, vol. 6, no. 3, pp. 537–542, 2006.
- [57] T. L. Jenkins and D. Little, "Synthetic scaffolds for musculoskeletal tissue engineering: Cellular responses to fiber parameters" *NPJ Regenerative Medicine*, vol. 1, p. 15, 2019.
- [58] S. H. Ku, S. H. Lee, and C. B. Park, "Synergic effects of nanofiber alignment and electroactivity on myoblast differentiation" *Biomaterials*, vol. 33, no. 26, pp. 6098–6104, 2012.
- [59] B. L. Samolyk *et al.*, "Developing porous fibrin scaffolds with tunable anisotropic features to direct myoblast orientation " *Tissue Engineering Part C: Methods*, vol. 30, no. 5, pp. 217–228, 2024. doi: 10.1089/ten.tec.2023.0363.
- [60] G. Agrawal, A. Aung, and S. Varghese, "Skeletal muscle-on-a-chip: An in vitro model to evaluate tissue formation and injury."
- [61] T. Serra, R. Tognato, and A. Augurio, "Patterned nanocomposites generated via electric/magnetic fields for hierarchical tissue regeneration."
- [62] A. Pardo *et al.*, "Magnetic nanocomposite hydrogels for tissue engineering: Design concepts and remote actuation strategies to control cell fate."
- [63] S. Singamaneni, V. N. Bliznyuk, C. Binek, and E. Y. Tsymbal, "Magnetic nanoparticles: Recent advances in synthesis, self-assembly and applications."
- [64] W. D. Callister Jr. and D. G. Rethwisch, Scienza ed Ingegneria dei Materiali.

- [65] D. Serantes and D. Baldomir, "Superparamagnetism and Monte Carlo simulations" Nov. 9, 2018.
- [66] K. J. M. Bishop, C. E. Wilmer, S. Soh, and B. A. Grzybowski, "Nanoscale forces and their uses in self-assembly."
- [67] B. Bharti and O. D. Velev, "Assembly of reconfigurable colloidal structures by multidirectional field-induced interactions."
- [68] M. Natta, G. Cocchi, R. Tognato, A. Cianciosi, and T. Serra, "Advanced contactless bioassembly approaches: Leveraging sound, optical, and magnetic fields."
- [69] J. Kim, J. R. Staunton, and K. Tanner, "Independent control of topography for 3D patterning of the ECM microenvironment."
- [70] K. Hu, J. Sun, Z. Guo, P. Wang, Q. Chen, M. Ma, and N. Gu, "A novel magnetic hydrogel with aligned magnetic colloidal assemblies showing controllable enhancement of magnetothermal effect in the presence of alternating magnetic field."
- [71] R. Tognato *et al.*, "A stimuli-responsive nanocomposite for 3D anisotropic cell-guidance and magnetic soft robotics."
- [72] A. Pardo *et al.*, "Magnetically-assisted 3D bioprinting of anisotropic tissue-mimetic constructs."
- [73] S. Lantean, I. Roppolo, M. Sangermano, M. Hayoun, H. Dammak, and G. Rizza, "Programming the microstructure of magnetic nanocomposites in DLP 3D printing."
- [74] S. Kalpakjian and S. R. Schmid, *Manufacturing Engineering and Technology*, 8th ed., SI Units.
- [75] A. Gebhardt and J.-S. Hotter, *Additive Manufacturing*. Munich: Carl Hanser Verlag GmbH & Co. KG, 2016, pp. I–XX.
- [76] A. Alhamed, "Difference Between STL and G-code Explained" Cytron Tutorials, Aug. 23, 2022.
- [77] A. Salas, M. Zanatta, V. Sans, and I. Roppolo, "Chemistry in light-induced 3D printing"
- [78] N. Bhardwaj, S. K. Yadav, A. Saneja, "Recent advances in 3D bioprinting for cancer research: From precision models to personalized therapies " *Drug Discovery Today*, 2024. doi:10.1016/j.drudis.2024.103924

- [79] T. Vaneker, A. Bernard, G. Moroni, I. Gibson, Y. Zhang, "Design for additive manufacturing: Framework and methodology " *CIRP Annals*, vol. 69, no. 2, pp. 578–599, 2020. doi:10.1016/j.cirp.2020.05.006
- [80] M. Lee, R. Rizzo, F. Surman, and M. Zenobi-Wong, "Guiding Lights: Tissue bioprinting using photoactivated materials"
- [81] Z. Mehdiyev and C. Felhő, "Polymer 3D printing: A review of techniques with their advantages, limitations, and industrial applications"
- [82] Q. Thijssen, J. Toombs, C. C. Li, H. Taylor, and S. Van Vlierberghe, "From pixels to voxels: A mechanistic perspective on volumetric 3D-printing"
- [83] M. Kaur and A. K. Srivastava, "Photopolymerization: A review"
- [84] P. Garra, J.-P. Fouassier, S. Lakhdar, Y. Yagci, and J. Lalevée, "Visible light photoinitiating systems by charge transfer complexes: Photochemistry without dyes"
- [85] R. Chaudhary, P. Fabbri, E. Leoni, F. Mazzanti, R. Akbari, and C. Antonini, "Additive manufacturing by digital light processing: A review "
- [86] C. E. Hoyle and C. N. Bowman, "Thiol—ene click chemistry" *Angewandte Chemie International Edition*, doi: 10.1002/anie.200903924.
- [87] M. Mukhtarkhanov, A. Perveen, and D. Talamona, "Application of stereolithography based 3D printing technology in investment casting"
- [88] R. Bongiovanni and A. Vitale, "Vat photopolymerization" in *High Resolution Manufacturing from 2D to 3D/4D Printing*, S. L. Marasso and M. Cocuzza, Eds. Cham: Springer, 2022, pp. 17–46. doi: 10.1007/978-3-031-13779-2_2.
- [89] N. H. Ononiwu, P. A. Ako, C. O. Anyaoha, C. V. Ikwuagwu, and I. O. Jacobs, "Sustainable considerations in additive manufacturing processes: A review"
- [90] D. Chekkaramkodi, L. Jacob, M. Shebeeb, R. Umer, and H. Butt, "Review of vat photopolymerization 3D printing of photonic devices"
- [91] D. J. Whyte, E. H. Doeven, A. Sutti, A. Z. Kouzani, and S. D. Adams, "Volumetric additive manufacturing: A new frontier in layer-less 3D printing"
- [92] A.-I. Bunea, N. del Castillo Iniesta, A. Droumpali, A. E. Wetzel, E. Engay, and R. Taboryski, "Micro 3D printing by two-photon polymerization: Configurations and parameters for the Nanoscribe system"

- [93] A. Nakayama, Y. Kumamoto, M. Minoshima, K. Kikuchi, A. Taguchi, and K. Fujita, "Photoinitiator-free two-photon polymerization of biocompatible materials for 3D micro/nanofabrication"
- [94] M. Regehly et al., "Xolography for linear volumetric 3D printing"
- [95] W. K. Swainson, "Method, medium and apparatus for producing three-dimensional figure product" U.S. Patent US4041476A, 1977.
- [96] L. Stoecker *et al.*, "Xolography for biomedical applications: Dual-color light-sheet printing of hydrogels with local control over shape and stiffness "
- [97] J. C. Sanger *et al.*, "Linear volumetric additive manufacturing of zirconia from a transparent photopolymerizable ceramic slurry via xolography"
- [98] N. V. Arguchinskaya *et al.*, "Properties and printability of the synthesized hydrogel based on GelMA"
- [99] T. Yan, D. Rao, Y. Chen, Y. Wang, Q. Zhang, and S. Wu, "Magnetic nanocomposite hydrogel with tunable stiffness for probing cellular responses to matrix stiffening"
- [100] W. Chen, Y. Zhang, J. Kumari, H. Engelkamp, and P. H. J. Kouwer, "Magnetic stiffening in 3D cell culture matrices"
- [101] Z. Püspöki, M. Storath, D. Sage, and M. Unser, "Transforms and operators for directional bioimage analysis"
- [102] M. Costantini *et al.*, "Engineering muscle networks in 3D gelatin methacryloyl hydrogels: Influence of mechanical stiffness and geometrical confinement"
- [103] Y. Ma et al., "Biomacromolecule-based agent for high-precision light-based 3D hydrogel bioprinting" 2023.
- [104] G. C. Ingavle, S. H. Gehrke, and M. S. Detamore, "The bioactivity of agarose–PEGDA interpenetrating network hydrogels with covalently immobilized RGD peptides and physically entrapped aggrecan" *Acta Biomaterialia*, vol. 10, no. 4, pp. 1543–1551, 2014. doi: 10.1016/j.actbio.2013.11.017.
- [105] G. Zhen *et al.*, "Comparative study of the magnetic behavior of spherical and cubic superparamagnetic iron oxide nanoparticles"